

Progress and Perspectives in Photo- and Electrochemical-Oxidation of Biomass for Sustainable Chemicals and Hydrogen Production

Hui Luo, Jesús Barrio, Nixon Sunny, Alain Li, Ludmilla Steier, Nilay Shah, Ifan E. L. Stephens, and Maria-Magdalena Titirici*

Biomass is recognized as an ideal CO₂ neutral, abundant, and renewable resource substitute to fossil fuels. The rich proton content in most biomass derived materials, such as ethanol, 5-hydroxymethylfurfural (HMF) and glycerol allows it to be an effective hydrogen carrier. The oxidation derivatives, such as 2,5-difurandicarboxylic acid from HMF, glyceric acid from glycerol are valuable products to be used in biodegradable polymers and pharmaceuticals. Therefore, combining biomass-derived compound oxidation at the anode and hydrogen evolution reaction at the cathode in a biomass electrolysis or photo-reforming reactor would present a promising strategy for coproducing high value chemicals and hydrogen with low energy consumption and CO₂ emissions. This review aims to combine fundamental knowledge on photo and electro-assisted catalysis to provide a comprehensive understanding of the general reaction mechanisms of different biomass-derived molecule oxidation. At the same time, catalyst requirements and recent advances for various feedstock compounds are also reviewed in detail. Technoeconomic assessment and life cycle analysis are performed on various feedstocks to assess the relative benefits of various processes, and finally critical prospects are given on the challenges and opportunities for technology development to meet the sustainability requirement of the future global energy economy.

1. Introduction

Elevated concentrations of atmospheric greenhouse gases (GHGs), particularly carbon dioxide (CO₂), have affected the global environment, causing climate deviations and threatening the biodiversity.^[1,2] Deep-cutting solutions and new technologies are thus imperative to repay the carbon debt.^[3] Hydrogen (H₂) is an ideal fuel to enable a successful transition to a global zero emission economy: With a gravimetric energy density more than double that of conventional fuels like diesel, gasoline, and natural gas it is a lightweight energy carrier which can be converted to electricity and water via fuel cells and thus holds great promise to cut emissions of the transport and energy sectors to zero. Furthermore, it is an energy dense chemical which is already used in the chemical industry (i.e., ammonia via the Haber–Bosch process) and steel manufacturing. However, these industries currently use brown (made from coal via gasification and subsequent water gas


shift reaction) and gray (made by steam methane reforming) hydrogen which both have significant CO₂ footprints. Thus, synthesizing green (meaning renewable) hydrogen cost-effectively is a solution which could green such industries and the transport sector and simultaneously meet our growing demands for viable energy storage solutions. However, switching from fossil-fuels to a hydrogen economy requires efficient technologies that permit clean, sustainable and cost-effective production, storage, and utilization of H₂.^[4–6]

Water electrolysis is a clean technology for green H₂ production, where water is split into H₂ at the cathode while O₂ is generated at the anode. Thermodynamically, the energy input required for this reaction equals an applied voltage of 1.23 V but in practice >1.8 V is commonly applied due to the sluggish kinetics of the oxygen evolution reaction (OER). The kinetics of the OER are complex. In addition to the thermodynamic potential of 1.23 V, even the best OER catalysts to date show significant overpotentials (0.35–0.4 V) which is due to suboptimal scaling relation between OOH and OH adsorption energies.^[7,8] As a consequence, a significant amount of energy is spent on

Dr. H. Luo, Dr. N. Sunny, Dr. A. Li, Prof. N. Shah, Prof. M.-M. Titirici
Department of Chemical Engineering
Imperial College London
South Kensington Campus, London SW7 2AZ, UK
E-mail: m.titirici@imperial.ac.uk

Dr. J. Barrio, Dr. L. Steier, Dr. I. E. L. Stephens
Department of Materials
Imperial College London
South Kensington Campus, London SW7 2AZ, UK

Dr. N. Sunny
Centre for Environmental Policy
Imperial College London
South Kensington Campus, London SW7 2AZ, UK

 The ORCID identification number(s) for the author(s) of this article can be found under <https://doi.org/10.1002/aenm.202101180>.

© 2021 The Authors. Advanced Energy Materials published by Wiley-VCH GmbH. This is an open access article under the terms of the Creative Commons Attribution License, which permits use, distribution and reproduction in any medium, provided the original work is properly cited.

DOI: 10.1002/aenm.202101180

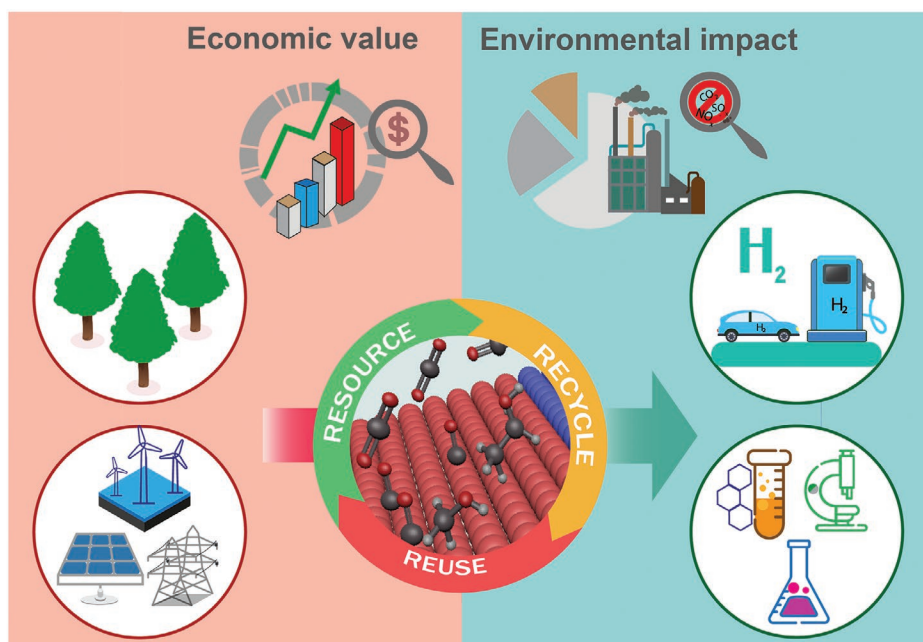


Figure 1. The basic conceptual illustration of biomass electrolysis.

a product (oxygen) with very low market value (and which is often vented), hindering the deployment of the green H_2 production market (until 2019 only 2% of dedicated H_2 is produced by water electrolysis),^[9] with the cost being a major drawback that limits the production of hydrogen at industrial scale.

Additionally, photon-driven water splitting has emerged as a feasible alternative for producing green hydrogen in a cost-effective manner. In this case, a semiconducting material is employed for harvesting incident solar light. The semiconductor shall have an electronic bandgap wider than 1.23 eV versus normal hydrogen electrode, implying that its conduction band potential should be more negative than the reduction potential of protons to molecular hydrogen. In addition, the valence band potential should be more negative than the oxidation potential of water to molecular oxygen. Nevertheless, up to now most of the reported semiconductors proven to produce H_2 upon water splitting do not display a positive enough valence band for carrying out the sluggish water oxidation.^[10–14]

Value-added oxidation reactions are a particularly attractive pathway forward to further reduce costs through a reduced energy consumption and added market value. As illustrated in **Figure 1**, biomass electrolysis as a viable alternative, substitutes the sluggish water oxidation with the thermodynamically more favorable organic molecule oxidation. Biomass is recognized as a CO_2 -neutral, abundant, and renewable resource substitute to fossil fuels.^[15] The rich proton content in most biomass building blocks also endows it to be an effective H_2 carrier. In the broader sense, biomass includes crop residues, forest residue, and even municipal solid waste. The estimated biomass production in the world is ≈ 100 billion metric tons of carbon per year.^[16] So far, thermal conversion of lignocellulosic biomass dominates the biomass energy market.^[17] Without carbon capture and storage (CCS) this generates CO_2 emissions. Some biomass sources (agricultural residues) are still burned on

fields not being properly managed. Hence, smarter ways of fully utilizing biomass toward high value products need to be designed. Antonini et al. published a life cycle assessment of methane and biomethane reforming to produce blue H_2 with CCS, concluding that the overall global warming potential is comparable to water electrolysis using renewable electricity.^[18]

In comparison to water electrolysis, the electrolysis of biomass feedstock to generate H_2 requires much lower theoretical electricity consumption.^[19–22] As an example, Shen and co-workers compared the energy input needed for electrolysis of renewable alcohols, such as ethanol, glycerol and ethylene glycol, to that needed for water electrolysis and found that the former requires $\approx 3\times$ less energy to produce the same amount of hydrogen under the same conditions.^[23]

Besides a lower electricity consumption, biomass electrolysis offers the opportunity to coproduce value added chemicals, representing a highly efficient power-to-X (X = fuel and chemicals) conversion. The current manufacturing of chemicals is energy and CO_2 -intensive, with most of the chemicals produced worldwide originating from fossil-fuel-derived feedstocks.^[24] Given this unsustainable production, urgent systemic changes are needed to transition to a greener chemical industry. The “2030 Agenda for Sustainable Development” adopted by the UN in 2015, urges the chemical industry to be low-carbon and resource efficient to create a circular economy and to have a minimal impact on health, safety, security, and the environment. The definition of performance must now be expanded beyond the technical function to also include sustainability considerations.^[25] Thus, although biomass electrolysis is still currently a lab-based technology, its potential large scale implementation to produce high-value commodity chemicals derived from renewable feedstocks via this power-to-X process is projected to accelerate manufacturing methods, efficiency, and sustainability.^[24]

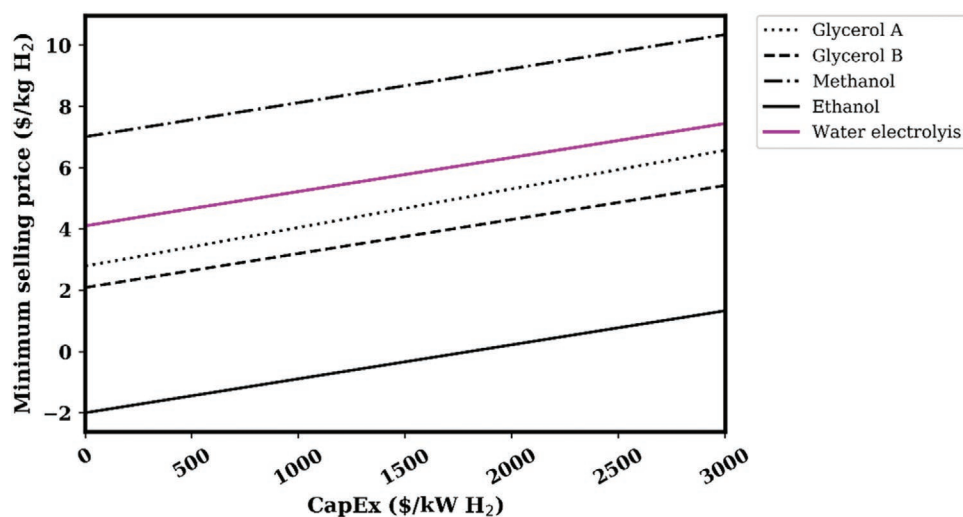


Figure 2. The profitability of the various electro-oxidation processes is described as a function of the total investment capital associated with its installation. The economic analysis incorporates raw material and electricity costs, fixed operating costs, depreciation, etc.

This review provides, for the first time, a holistic description of the photo- and electrochemical oxidation of biomass-derived organic compounds such as glycerol (biodiesel waste byproduct), glucose and 5-hydroxymethylfurfural (HMF) (biomass-derived chemicals), methanol and ethanol (biomass fermentation), and urea (wastewater). We summarize the fundamental understanding of photo- and electrochemical catalytic mechanism of biomass molecule transformation and provide critical overview of the catalyst design and benchmarking for different biomass substrates. These research advances are combined with technoeconomic assessment and life cycle analysis to assess the relative benefits of various processes and industrial feasibility, based on which finally critical prospects are given on the challenges and opportunities for technology development to meet the sustainability requirement of future global energy economy.

2. Economic and Environmental Perspectives

A high production cost is the main barrier which hinders the deployment of low-carbon technologies. Conventional H₂ production technologies such as steam methane reforming use natural gas as the primary feedstock, often at very low to zero marginal costs in some regions of the world. The electro-oxidation of bio-derived feedstocks could yield chemicals of major economic importance, which can generate additional income, providing a more cost-competitive alternative. Thus, to give some indicative information on the economic value and environmental impact of this process on a larger scale, we have conducted some basic technoeconomic assessment and life cycle analysis.

Researchers have shown that most electrocatalysts for organic compound electro-oxidation deliver higher activity and stability in alkaline conditions.^[23,26,27] Therefore, here we have analyzed the economic viability of five alkaline oxidation process schemes, which involve the electro-oxidation of bio-derived glycerol, ethanol, and methanol in diluted potassium hydroxide

(KOH) supporting electrolyte. The results are depicted in **Figure 2**. The raw material and electricity input-output data for all the processes are summarized in Tables S1 and S2 of the Supporting Information. Lab-scale experimental data from literature was used to define the process input-outputs. Importantly, the aim of this section is not to present comprehensive technoeconomic modeling of electro-oxidation processes, but rather to screen their potential viability for future deployment based on indicative values. This enables researchers to identify and develop the most relevant set of processes which offer value in a decarbonized future. In this instance, glycerol is assumed to be sourced as a product from the esterification of soybean oil, ethanol from the fermentation of sugarcane, methanol from biogas. The power requirements for all the various processes are supplied using renewable electricity from offshore wind farms, using Great Britain as a location reference. KOH is sourced directly from the global market of suppliers. In processes A and B, glycerol is electro-oxidized under alkaline conditions, which leads to the formation of products such as potassium glycerate, tartronate, glycolate, oxalate, formate, and carbonate in addition to H₂ with different product selectivity. Most of the coproducts from process A and B are currently sold as fine chemicals in the global marketplace. However, the demand for these products is expected to increase due to growth in cosmetics, pharmaceuticals, and biopolymer applications.^[28,29] Methanol and ethanol electro-oxidation leads to the formation of potassium formate and acetate, respectively.^[20,30] The main disadvantage of the alkaline electro-oxidation processes is their lower H₂ selectivity. H₂ constitutes at most 6% of the overall product share on a mass basis in the processes investigated in this study. However, the future demand for H₂ is expected to increase greatly beyond that of the coproducts.^[31] This might constrain the overall deployment potential of this technology toward small scale applications in the absence of a sufficiently large market for the coproducts.

The net present value of investment is used to compare the economic viability of the various process designs whilst accounting for the raw material costs, cost of electricity, fixed

and variable operating expenditure, revenue for the product streams, etc. The minimum selling price illustrated in Figure 2 was calculated by identifying the price of H₂ required to reach net present value of 0. More information on the assumptions related to the economic parameters can be found in Tables S3–S5 of the Supporting Information.

Notably, only ethanol electro-oxidation has a negative medium selling price at low CapEx values, indicating the profitability of the process without requiring additional revenue from the sale of H₂. For all the other process schemes, including water electrolysis, the net present value of investment is negative in the present market, and therefore requires financial support to initiate their deployment. Relative to water electrolysis, both glycerol oxidation schemes (processes A and B) require a lower minimum selling price to be economically viable, reducing the level of financial support at comparable CapEx values. However, their overall deployment potential is also dependent on their environmental footprint. The electro-oxidation of methanol appears to be the least profitable process, requiring a higher minimum selling price compared to water electrolysis, mainly due to the lower revenue from the sale of potassium formate. Overall, more detailed process design needs to be developed to estimate the economic viability at commercial scale.

The global warming potential of the aforementioned processes is estimated to benchmark their performance against steam methane reforming. For this purpose, life cycle assessment software SimaPro was used with the following functional basis: production of 1 kg of hydrogen at low temperature (<60 °C) and atmospheric pressure. The inventory data used for the characterization of life cycle impacts are provided as part of process input–output data in Table S6 of the Supporting Information and translated into impact assessments using the ReCiPe 2016 midpoint method.^[35]

In this review, different processes are compared based on the overall environmental impacts associated with the procurement of both raw materials and electricity to produce H₂. The electro-oxidation-based processes produce several value-added chemicals as coproducts, which are responsible for a certain share of the environmental impacts. An attributional modeling approach, incorporating economic revenue share principles, was used for the allocation of environmental impacts to the different product streams. These figures are reported in Tables S7–S11 of the Supporting Information. In practice, the revenue shares may differ due to market price volatilities and geographical variations over time. Nevertheless, **Figure 3** presents an indicative breakdown of the global warming potential owing to the various process elements.

The key distinction between the electro-oxidation processes and steam methane reforming is the absence of operating emissions. Therefore, the overall global warming potential of these processes is primarily a function of the upstream emissions associated with the sourcing of raw materials and electricity. Overall, the consumption of glycerol appears to have a greater CO₂ footprint (4.1 kg CO_{2,eq}/kg H₂) relative to that of KOH (1.7 kg CO_{2,eq}/kg H₂) due to the land use change associated with crop production. However, it is worth noting that the allocation of environmental impacts between the fatty acid methyl esters.^[1] Fatty acid methyl esters are the primary products of the esterification of vegetable oils from which glycerol can be sourced as

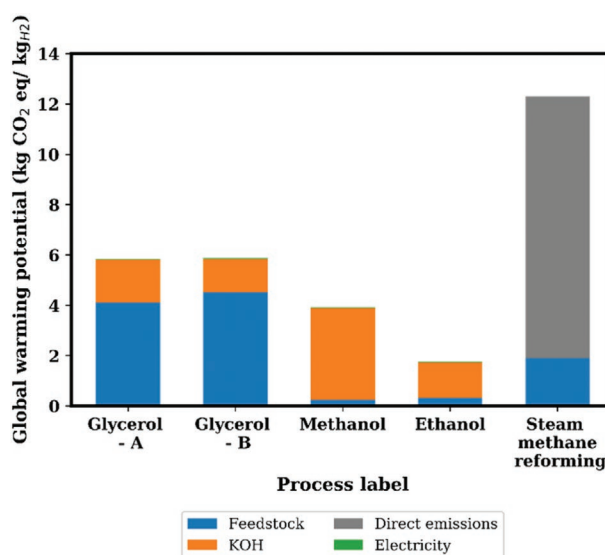


Figure 3. Global warming potential of alkaline electro-oxidation processes in comparison with steam methane reforming. The feedstock is the organic compound which undergoes electrolysis except in the case of steam methane reforming where it is natural gas. The data for electricity consumption, product selectivity, and mass balance of the four electrolysis processes are sourced from literature: methanol: 12 kWh kg_{H₂}⁻¹, assuming a 100% Faradaic efficiency to potassium formate and H₂;^[32] ethanol: 22.8 kWh kg_{H₂}⁻¹, assuming a 100% Faradaic efficiency to potassium acetate;^[33] glycerol-A: 23.3 kWh kg_{H₂}⁻¹, assuming a 100% Faradaic efficiency to H₂, and product selectivity to chemicals are: potassium glycerate (35%), potassium tartronate (36%), potassium glycolate (3%), potassium oxalate (14%), potassium formate (2.5), potassium carbonate (12.5%);^[33] glycerol-B: 23.3 kWh/kg_{H₂}⁻¹, assuming a 100% Faradaic efficiency to H₂, and product selectivity to chemicals are: potassium glycerate (48%), potassium tartronate (26%), potassium glycolate (7%), potassium oxalate (4%), potassium formate (6), and potassium carbonate (9%).^[34] The global warming potential for different components are allocated on a mass basis, and the high CO₂ footprint of glycerol (4.1 kgCO_{2,eq} kg⁻¹ H₂) is associated with land use for crop production.

a waste byproduct and glycerol vary depending on the primary feedstock (e.g., soybean, rapeseed, palm) and glycerol could have a lower CO₂ footprint depending on the yield of the esterification process. Importantly, the use of KOH adds notable contributions to the global warming potential of all four processes, thereby limiting the capacity for alkaline electrolysis to be very low carbon. This is principally a result of the usage of both electricity and heat in the production of KOH. Existing supply chains that are used to supply heat and electricity during the production of KOH are CO₂-intensive due to the combustion of hard coal and lignite. There is considerable potential to reduce the CO₂ footprint owing to electricity and heat in a carbon-neutral world. Nonetheless, future research efforts in this area must aim to reduce the consumption of KOH, whilst increasing the selectivity toward H₂ production. The electricity consumption has a minimal impact on the overall CO₂ footprint of the processes, namely, due to the lower specific electricity requirement (23.3 kWh/kg H₂) in processes A and B compared to water electrolysis (50.5 kWh/kg H₂), in addition to the renewable electricity supply. Methanol and ethanol electro-oxidation appear to have a lower global warming potential compared to both steam methane reforming and the glycerol oxidation processes. In

this instance, the CO₂ footprint attributable to KOH is higher than that of methanol and ethanol due to the greater upstream emissions associated with the KOH supply chain, in addition to the greater quantities needed. Relative to steam methane reforming, alkaline electro-oxidation of glycerol via process A, B, in addition to methanol and ethanol yield reductions in the global warming potential by 53%, 52%, 68%, and 86%, respectively. However, all processes have a greater impact than renewable wind-based water electrolysis, which has an approximate global warming potential of 0.97 kg CO_{2,eq}/kg H₂.^[36] Electrolysis of biomass in acidic conditions may improve process sustainability despite the lower activity,^[23,26,27] as acids such as sulfuric acid (0.17 kg CO_{2,eq}/kg H₂SO₄), have a considerably lower global warming potential than KOH (2.57 kg CO_{2,eq}/kg KOH). Alternatively, alkaline electrolysis can be coupled with the electro-dialysis process to recycle KOH while converting the potassium salts back to organic acids, although at a higher electricity consumption.^[37,38] The potential of different processes will be justified in Section 7.

In summary, alkaline electro-oxidation of biomass may offer a more economical alternative to water electrolysis, albeit with a greater global warming potential. However, it has a lower global warming potential compared to steam methane reforming and could play a key role in the transition toward net-zero. Importantly, reducing the CO₂ footprint of the feedstocks and the alkaline reagent can ensure that the process has a near-zero global warming potential. However, such low-carbon feedstocks and reagents may be costlier as they reflect the cost of CO₂ abatement. Hence, there is a trade-off between the economic viability of the process and its environmental performance. In the long run, the regulatory environment may facilitate a transition toward cleaner feedstocks, which can improve both the economics and environmental performance of these processes. Nevertheless, in the near term, acidic electro-oxidation of biomass must be investigated as an interim technology due to its potential to produce more mature coproducts with a lower global warming potential. In all cases, detailed designs need to be developed for the operation of these process at commercial scale to better understand the overall energy requirements from separation of the product streams, its costs and the resulting global warming potential. Future research must also address the overall impact of plant construction, operating patterns, and decommissioning on the global warming potential.

3. Water and Biomass Electrolysis Comparison

Water electrolysis has long been established as a clean technology for H₂ production. Its working principles and some of the most recent scientific developments are reviewed in detail in other dedicated reviews.^[41,46–49] In all cases OER involves multi-proton-coupled electron-transfer steps, suffering from the limitation of suboptimal scaling relation between OOH and OH adsorption energies, which is the major bottleneck and requires a cell potential above 1.23 V.^[7]

In biomass electrolysis, a complete oxidation process, also known as electrochemical reforming, such as methanol electrolysis, produces CO₂ under acidic condition (CO₃²⁻ under alkaline

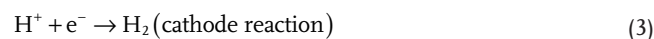
in the anode and H₂ at the cathode, resulting in a maximum proton utilization. The partial oxidation of certain feedstocks could concomitantly generate H₂ and value-added chemicals. For example, the electro-oxidation of glycerol lead to the formation of glyceric acid and hydroxypyruvic acid,^[43] while glucaric acid is produced by electrochemically converting glucose on a NiFeO_x electrode.^[50] A diagram summarizing the working principles of water and biomass derivatives is included in **Figure 4A**.

For both water and biomass electrolysis, the chemical transformations induced by the simultaneous transfer of an equal number of electrons and protons, require a high rate of charge transfer for the chemical reaction to proceed efficiently. To maximize the efficiency of such transformations, the utilization of electrocatalysts is necessary. Electrocatalysts are chosen primarily based on their ability to drive redox reactions with low energy loss, represented by the electrochemical cell voltage, *V*, generally given by

$$V = \Delta E_{\text{eq}} + \eta_a + \eta_c + IR \quad (1)$$

where ΔE_{eq} is the difference between the equilibrium electrode potentials, η_a and η_c are the overpotentials at the anode and cathode, respectively,^[51] and *IR* is the ohmic drop induced by the intrinsic resistance of the electrolyte and bubble effect.^[52] For water electrolysis, the ΔE_{eq} is 1.23 V regardless of the electrocatalyst used. Great scientific efforts have been devoted to developing efficient catalysts that can reduce the η_a and η_c , those being classified as hydrogen evolution reaction (HER) and OER electrocatalysts. Recent advances and challenges in water splitting electrocatalysis could be found in several recent reviews.^[53–59]

In the case of biomass electrolysis, *q* including organic molecules C_xH_yO_z, the ΔE_{eq} differs due to the thermodynamics of organic molecule oxidation reactions. Its efficient transformation is governed by kinetics, which can be achieved with a suitable electrocatalyst to compensate for the involved overpotentials. The working principle of biomass (organic compounds) electrolysis involves reactions at both the anodic and cathodic sides



As HER at the cathode typically possesses a high Faradaic efficiency (>95%), the electrical balance between the two reactions enables the estimation of H₂ produced based on the electrochemical profile of the anode. Hence, this measuring tool has been used in most of the organic molecule electrolysis studies to calculate the H₂ production energy efficiency.

The thermodynamics of oxidation for different molecules determine the ΔE_{eq} in Equation (1), which is the first parameter to consider when assessing the potential of a certain feedstock for electrolysis. As can be seen from Figure 4B (exact values listed in **Table 1**), which summarizes the energetics of different molecules in electrolysis, all reactions need an external energy input ($\Delta G > 0$), sourced from the electricity. In the case of organic molecules, the energy needed to produce one mole of hydrogen is smaller compared with water.^[44] Nevertheless, a complete oxidation is often difficult to achieve, the

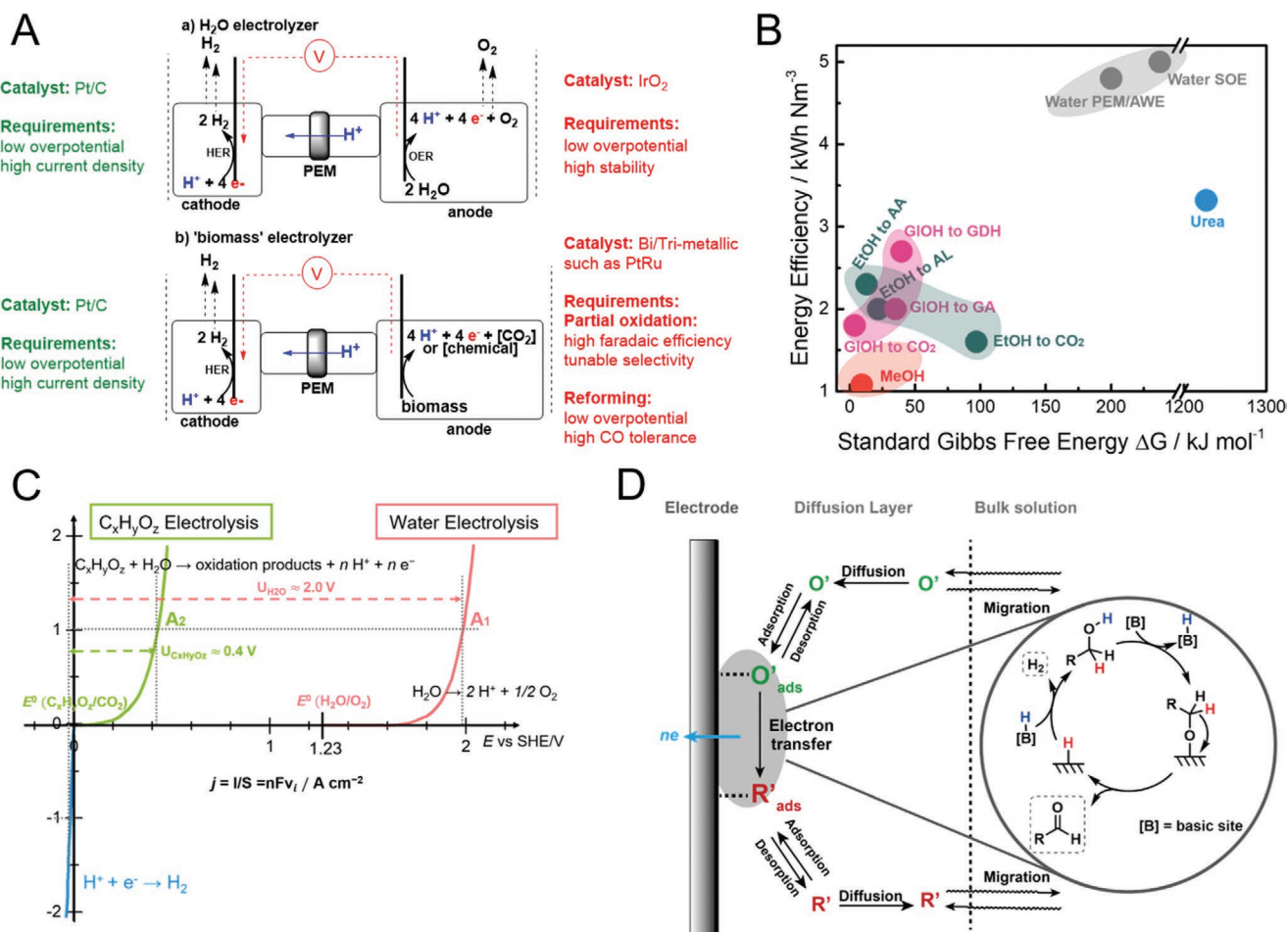


Figure 4. A) Schematic diagram of water electrolyzer and biomass electrolyzer operating in a proton exchange membrane (PEM) configuration. The state-of-art catalysts for each reaction and the catalyst requirements are also summarized. B) A comparison of different feedstocks in terms of the theoretical thermodynamics and the experimental results on H₂ production energy efficiency. (The ΔG is calculated assuming a 100% Faradaic efficiency to the indicated products, and the shadow for each feedstock represents the range where experimental values are reported for energy efficiency, depending on catalyst type, loading, operation condition, etc. SOE: solid oxide electrolyzer; PEM/AE: proton-exchange membrane/alkaline electrolyzer;^[39–41] MeOH: methanol; EtOH: ethanol; GIOH: glycerol; AA: acetic acid; AL: acetaldehyde; GDH: glyceraldehyde; GA: glyceric acid.) Data sourced from MeOH to CO₂,^[30] EtOH to CO₂,^[22] EtOH to AA,^[20,23,33] EtOH to AL,^[22] urea oxidation,^[42] GIOH to GDH,^[43] GIOH to GA,^[23] GIOH to CO₂.^[44] C) Theoretical reaction kinetics controlled by the Butler–Volmer law, $U_{\text{C}_x\text{H}_y\text{O}_z}$, and $U_{\text{H}_2\text{O}}$ are the cell voltage for $\text{C}_x\text{H}_y\text{O}_z$ and water electrolysis at 1 A cm^{-2} current density. Reproduced with permission.^[45] Copyright 2020, Elsevier. D) Schematic diagram of the pathway of a general electrode reaction.

thermodynamics of organic molecule oxidation reactions normally need to be recalculated based on the products detected. For example, a complete ethanol oxidation in acidic media generates CO₂ and H₂ with electron transfer $n = 14$ and $\Delta H = 348 \text{ kJ mol}^{-1}$, while in a real ethanol oxidation experiment the reaction product is mainly acetic acid, which is a four electron transfer process and requires only $\Delta H = 79.1 \text{ kJ mol}^{-1}$.^[22]

The kinetics diagram for water and biomass oxidations is displayed in Figure 4C,^[45] with the specific values for different substrates summarized in Table 1. It can be seen that, despite the low ΔE_{eq} , for both water and biomass electrolysis, the kinetics of the anodic reaction are sluggish due to the multielectron transfer processes, leading to high overpotential η_a in Equation (1).^[22] Thus, a higher cell voltage at a high current density is needed to achieve a high H₂ production rate. To achieve 1 A cm^{-2} current density, water electrolysis requires $U_{\text{cell}} \approx 2 \text{ V}$, biomass derived organic molecules, with a

$\Delta E_{\text{eq}} \approx 0 \text{ V}$, typically need around 0.4 V to drive the electrolysis process, which is energetically favorable.

HER coupled with oxidation reactions at the anode, i.e., partial oxidation for value-added chemical production, selectivity is also a critical factor when choosing the electrocatalysts, as product overoxidation would lead to a lower economic impact. An example would be the comparison of two glycerol oxidation processes investigated in Section 2. The selectivity toward various products will directly affect the selling price for H₂ as well as the global warming potential. Electrosynthesis via anodic oxidations go through multisteps, involving the adsorption of reactant molecules, interatomic bond cleavage, electron transfer, oxidation by oxygenated species to the intermediates and final product desorption, as illustrated in Figure 4D. Hence, electrochemical methods solely cannot deliver complete information about the ongoing reaction.^[26] High-performance liquid chromatography (HPLC) with rapid online sample collection,^[60]

Table 1. Summary of the thermodynamic requirements for the electrolysis of different substrates along with the energetic requirements for H₂ production.

Substrates	Type	Equation	ΔH [kJ mol ⁻¹]	ΔG [kJ mol ⁻¹]	Potential versus RHE	Potential@1 A cm ⁻²	<i>n</i>	We [kWh Nm ⁻³]	Ref.
Water	AWE	2H ₂ O + 2e ⁻ → H ₂ + 2OH ⁻ ; 2OH ⁻ → 1/2O ₂ + H ₂ O + 2e ⁻	285.8	237.2	1.229	1.8–2.0	2	4.8	[39–41]
	PEMWE	H ₂ O → 1/2O ₂ + 2H ⁺ + 2e ⁻ ; 2H ⁺ + 2e ⁻ → H ₂							
	SOE@875 °C	O ²⁻ → 1/2O ₂ + 2e ⁻ ; H ₂ O + 2e ⁻ → H ₂ + O ²⁻	250	200	0.97				
Methanol	PEM	CH ₃ OH + H ₂ O → CO ₂ + 6H ⁺ + 6e ⁻ ; 6H ⁺ + 6e ⁻ → 3H ₂	131.5	9.3	0.016	0.5	6	1.08	[30]
	Overall	CH ₃ OH + H ₂ O → CO ₂ + 3H ₂							
	AE	CH ₃ OH + 5OH ⁻ → HCOO ⁻ + 4e ⁻ + 4H ₂ O; 4H ₂ O + 4e ⁻ → 2H ₂ + 4OH ⁻					4		
Ethanol	PEM	C ₂ H ₅ OH + 3H ₂ O → 2CO ₂ + 12H ⁺ + 12e ⁻ ; 12H ⁺ + 12e ⁻ → 6H ₂	348	96.9	0.084	0.6	12	1.6–2.3	[20,22,23,33]
	Overall	C ₂ H ₅ OH + 3H ₂ O → 2CO ₂ + 6H ₂							
	AE	C ₂ H ₅ OH + 5OH ⁻ → CH ₃ COO ⁻ + 4H ₂ O + 4e ⁻ ; 4H ₂ O + 4e ⁻ → 2H ₂ + 4OH ⁻			0.11		4		
To acetaldehyde	Overall	C ₂ H ₅ OH + OH ⁻ → CH ₃ COO ⁻ + 2H ₂							
	Overall	C ₂ H ₅ OH → CH ₃ CHO + 2H ⁺ + 2e ⁻ ; 2H ⁺ + 2e ⁻ → H ₂					2		
	Overall	C ₂ H ₅ OH → CH ₃ CHO + H ₂							
To acetic acid	Overall	C ₂ H ₅ OH + 3H ₂ O → CH ₃ COOH + 4H ⁺ + 4e ⁻ ; 4H ⁺ + 4e ⁻ → 2H ₂	79.1	22	0.057		4		
	Overall	C ₂ H ₅ OH + 3H ₂ O → CH ₃ COOH + 2H ₂							
	Overall	CO(NH ₂) ₂ + 6OH ⁻ → N ₂ + 5H ₂ O + CO ₂ + 6e ⁻ ; 6H ₂ O + 6e ⁻ → 3H ₂ + 6OH ⁻		1227.2	0.37		3.32		[42]
Glycerol	PEM	C ₃ H ₈ O ₃ + 3H ₂ O → 3CO ₂ + 14H ⁺ + 14e ⁻ ; 14H ⁺ + 14e ⁻ → 7H ₂	342.8	3.9	0.003	0.7	14	1.8–2.7	[23,33,43,44]
	Overall	C ₃ H ₈ O ₃ + 3H ₂ O → 3CO ₂ + 7H ₂							
	To glycerinaldehyde	C ₃ H ₈ O ₃ → C ₃ H ₆ O ₃ + 2H ⁺ + 2e ⁻ ; 2H ⁺ + 2e ⁻ → H ₂	61.1	39.7	0.206		2		
To glyceric acid	Overall	C ₃ H ₈ O ₃ → C ₃ H ₆ O ₃ + H ₂							
	Overall	C ₃ H ₈ O ₃ + H ₂ O → C ₃ H ₆ O ₄ + 4H ⁺ + 4e ⁻ ; 4H ⁺ + 4e ⁻ → 2H ₂	88.7	35.1	0.091		4		
Overall	Overall	C ₃ H ₈ O ₃ + H ₂ O → C ₃ H ₆ O ₄ + 2H ₂							

Note: Because of the multistep oxidation, only the first two primary oxidation processes in glycerol oxidation is listed here, characteristics for glucose and HMF is not included.

in situ Fourier-transform infrared spectroscopy (FTIR),^[27,61,62] electrochemical mass spectroscopy (MS),^[63] and nuclear magnetic resonance (NMR)^[64] are needed as powerful analytic tools to deliver the full picture, in particular in relation to the identification of the resulting products. The judicious combination of electrochemical, spectroscopic, and chromatographic methods provides information on the reactant conversion rate, reaction intermediates, and product distribution at both qualitative and quantitative level. The anode reaction requires an accurate control of the reaction process, which rely significantly on the structural and electronic properties of the electrocatalysts (catalyst-substrate interaction).^[44] Thus, the overall performance of an electrocatalyst is determined by the number of active sites as well as the intrinsic activity and selectivity of every single site. The evaluation parameters, such as onset potential, overpoten-

tial, current density, and selectivity are similar to conventional electrocatalysis, but with unique characteristics for organic molecules transformations. To aid the understanding of literature reviewed below, they are summarized and justified in Section S1 of the Supporting Information.

From the discussion above we can conclude that the development of biomass electrolysis faces three main challenges: i) the development of electrocatalysts to reduce the activation energy for both the anode (molecule oxidation) and cathode (hydrogen production) reactions,^[33] determining both the energy consumption for H₂ production and the selectivity toward valuable chemicals; ii) the fundamental understanding of the main electrocatalytic and interfacial processes for different reactants. This helps to accurately control the reaction process and to manipulate the selectivity toward desired products;

and finally iii) the scale up of such systems for practical end-use. Hence, in the following section, we will be focusing on reviewing the reaction mechanism and electrocatalyst requirements for different organic molecules. The perspectives on the technology up-scaling and development would be included in the last section.

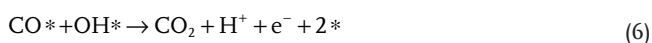
4. Hydrogen Production by Selective Electro-Oxidation of Oxygenated Compounds

4.1. Intrinsic Metal Properties for Different Chemical Bond Activation

Before introducing the electro-oxidation of specific organic compounds, it is necessary to highlight the general reaction mechanisms and the requirements for different electrocatalysts. The last section summarized the influence of reaction thermodynamics, often referred as the molecular-level Marcus theory and the kinetics, described by the Butler–Volmer equation. However, the interaction between the electrocatalyst and the reaction intermediates needs to be considered. In such case, the Sabatier principle states that intermediates binding to the catalyst should be neither too strong or too weak, in which case each reaction step should be thermodynamically neutral or downhill.^[65]

It is widely hypothesized that the removal of CO on the catalyst surface is the rate-determining step of electrochemical oxidation of many organic molecules, especially alcohols such as methanol, ethanol, and glycerol. The poisoning effect of precious metal catalysts such as Pt and Pd is also one of the most severe problems in the anode reaction. Thus, it is important to understand the CO oxidation mechanism, in order to look for active and stable anode materials that are able to either bind CO weakly but still oxidize the organic molecules, or that oxidize CO at significantly reduced overpotential.

There are two well-established CO oxidation mechanism in the literature, the Langmuir–Hinshelwood mechanism suggested by Gilman,^[66] expressed as



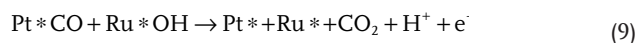
where the * denotes a free site on the catalyst surface. The first reaction is a reversible process, whereas the last two are irreversible reactions. Some researchers also interpret the last step into two reactions, i.e.,



Figure 5A has shown the intermediate's energies and barriers during CO oxidation on Pt(111) surface, with the potentials corresponding to the various free-energy profiles using computational hydrogen electrode approach. Applying a Sabatier

analysis,^[70] the optimal catalyst for the electrochemical oxidation of CO must possess a moderate binding energy toward both CO_{ads} and OH_{ads} , so as to not be limited by the adsorption of reactive intermediates or the desorption of products. Therefore, Figure 5B presents the activity of different transition metals over CO oxidation at 0.75 V, in which it is apparent that the optimal materials are ones that binds CO weaker than Pt(111), presumably Pt alloys, such as PtRu and PtMo.^[67] In practice, an earlier study, combining experimental and density functional theory (DFT) calculations on Cu-modified Pt(111), showed the interplay between CO and O binding in controlling CO oxidation. They have shown that PtCu alloys with a Cu sub-surface can weaken the binding of CO, shift the CO oxidation potential, thus decreasing the CO surface coverage.^[71]

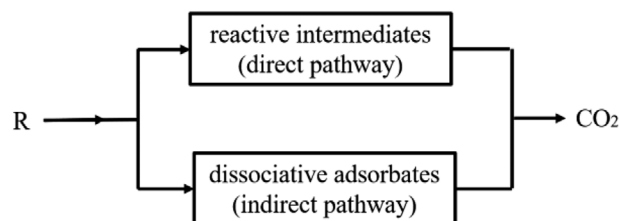
PtRu bimetallic electrocatalyst offers superior catalytic performance toward CO removal via a Watanabe–Motoo bifunctional mechanism, as expressed in the following equation



where Pt^* and Ru^* represent the freed Pt and Ru sites.^[72] The Ru atom could adsorb OH^- ions at low onset potential to supply sufficient OH to oxidize adsorbed CO (and similar carbonyl species) on Pt sites, as shown in Figure 5C.^[73] CO stripping voltammetry experiments are typically used to evaluate the activity of CO removal over different metal surfaces. By stepping from the potential where the CO adlayer is stable toward a “final potential” where the CO adlayer will be fully oxidized, the kinetics of CO oxidation can be studied. Figure 5D shows a typical example of CO stripping on Pt and PtRu catalysts.^[68] The overpotential on PtRu is significantly lower than Pt, with two peaks assigned to the oxidation of CO from the Ru and neighboring Pt (low-potential peak), and from the uncovered Pt surface (high-potential peak), respectively.

Nørskov and co-workers modeled the electro-oxidation of CO on close packed PtRu surface and found that there is a correlation between the d-band center and the CO adsorption energy. This correlation can be explained by the ligand effects, which will be explained in more detail in the following discussion. The higher the d-state energy, the stronger the bond. As shown in Figure 5D, the PtRu model has a d-band, which is shifted down by 0.6 eV, thus weakens the chemisorption bond.^[69]

Moving toward organic molecules, methanol electro-oxidation constitutes the simplest and most studied model compared to longer chained compounds. However, in the oxidation process to CO_2 , there are still six electrons involved, implies an inevitably complex mechanism, with several intermediate species participated. For these small organic molecules, the anodic oxidation generally goes through a dual-compete reaction mechanism, simplified as



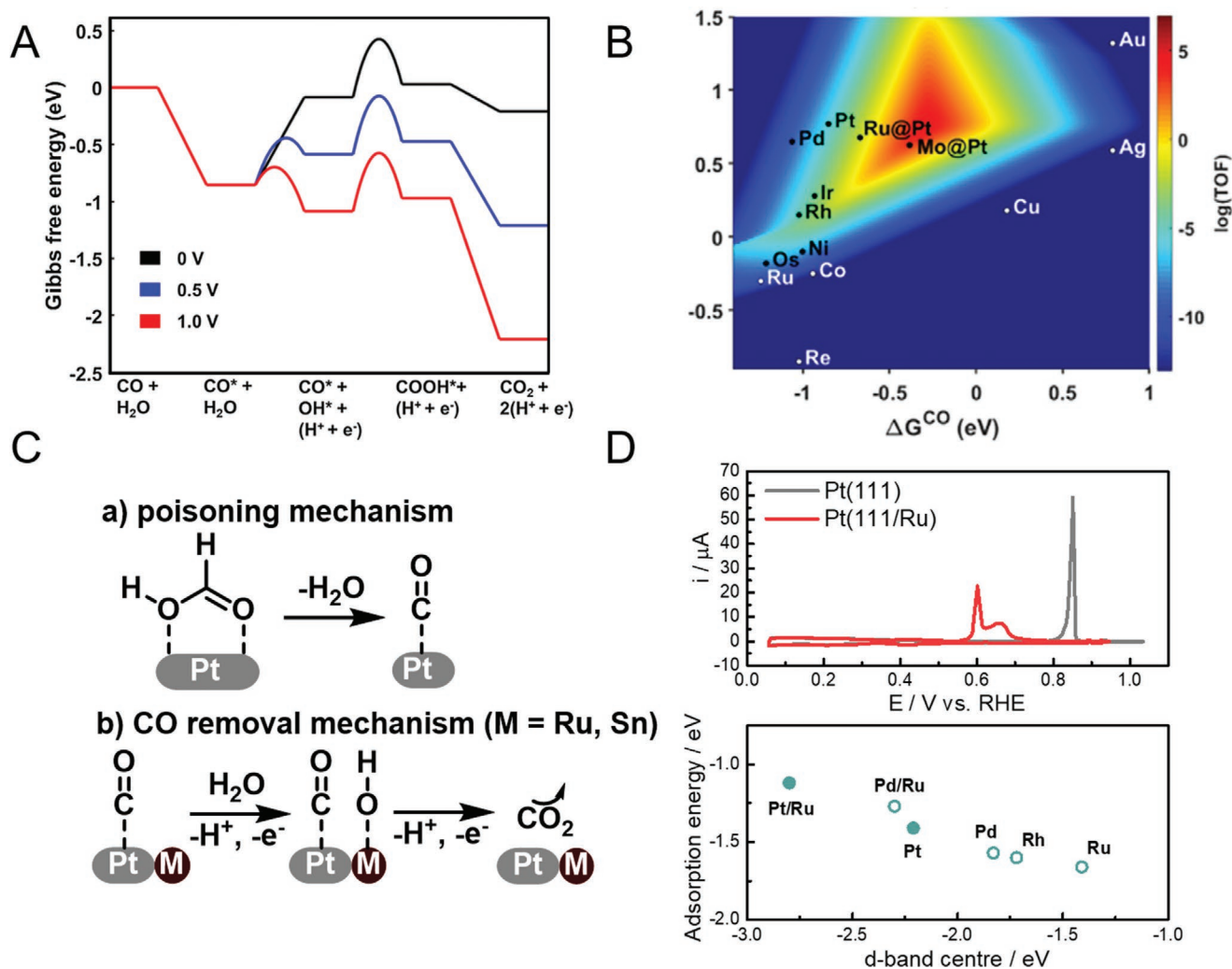


Figure 5. A) Gibbs free energy diagram on Pt(111) at three different applied potentials. Electrochemical steps and their associated barriers are accelerated when potential is increased, while chemical steps are unaffected. Each potential is given versus RHE. B) Activity maps of different metal catalysts at the applied potential of 0.75 V_{RHE} . All markers represent the most close-packed surfaces of the transition metals, along with two Pt skin alloys. Marker colors (white or black) only differ for visibility. Reproduced with permission.^[67] Copyright 2020, Elsevier. C) (a) CO-poisoning mechanism over Pt surface and (b) the bifunctional mechanism promoted by Ru, Sn for CO removal. D) Top: experimental CO stripping voltammetry from Pt(111) and Pt(111)/Ru. Adsorption of CO for 10 min at -0.15 V versus sat. Ag/AgCl, 0.1 M H_2SO_4 , scan rate 50 mV s^{-1} . Ru coverage $\approx 0.2 \text{ ML}$. Reproduced with permission.^[68] Copyright 2002, Royal Society of Chemistry. Bottom: calculated adsorption energies for CO on different metals and overlayers plotted as a function of the d-band center ϵ_d . Reproduced with permission.^[69] Copyright 2003, Elsevier.

where the direct pathway involves more weakly adsorbed or even partially dissolved intermediates, such as HCHO and HCOOH, and the indirect pathway takes place with strongly adsorbed intermediates, now commonly accepted to be CO. The sluggish kinetics of this pathway mainly result from the difficulty in CO removal, thus the understanding of CO oxidation as mentioned earlier is utterly important.

The reaction paths and possible intermediates in methanol oxidation with the free energies for the different intermediates on the Pt(111) surface plotted are shown in Figure 6A. Similar to CO oxidation, the reactivity of methanol oxidation also relies on two key descriptors: G_{CO^*} and G_{OH^*} . Structure sensitivity behavior of different Pt electrodes have been observed by Koper and co-workers, with the influence on reaction rate and reaction pathways.^[80] This phenomenon has been studied by

Mavrikakis and co-workers with DFT modeling, in which they have shown that on Pt(111) the direct pathway is thermodynamically favored at low potentials, whereas on Pt(100) both pathways are thermodynamically feasible at relatively low potentials. However, because CO_{ads} poisoning will be much stronger on the Pt(100) surface, the activity via direct pathway becomes difficult to detect. The authors predicted that for most metals studied, the indirect mechanism requires higher onset and overpotential than the direct mechanism, on both (111) and (100) facets, as shown in Figure 6B.^[75] Thus, it is important to develop efficient methanol oxidation electrocatalysts that can lower the potential needed to overcome the indirect pathway.

A possible approach toward lower overpotentials is the use of bifunctional structures, as mentioned in CO oxidation. PtRu is one good example, which is the most commercially successful

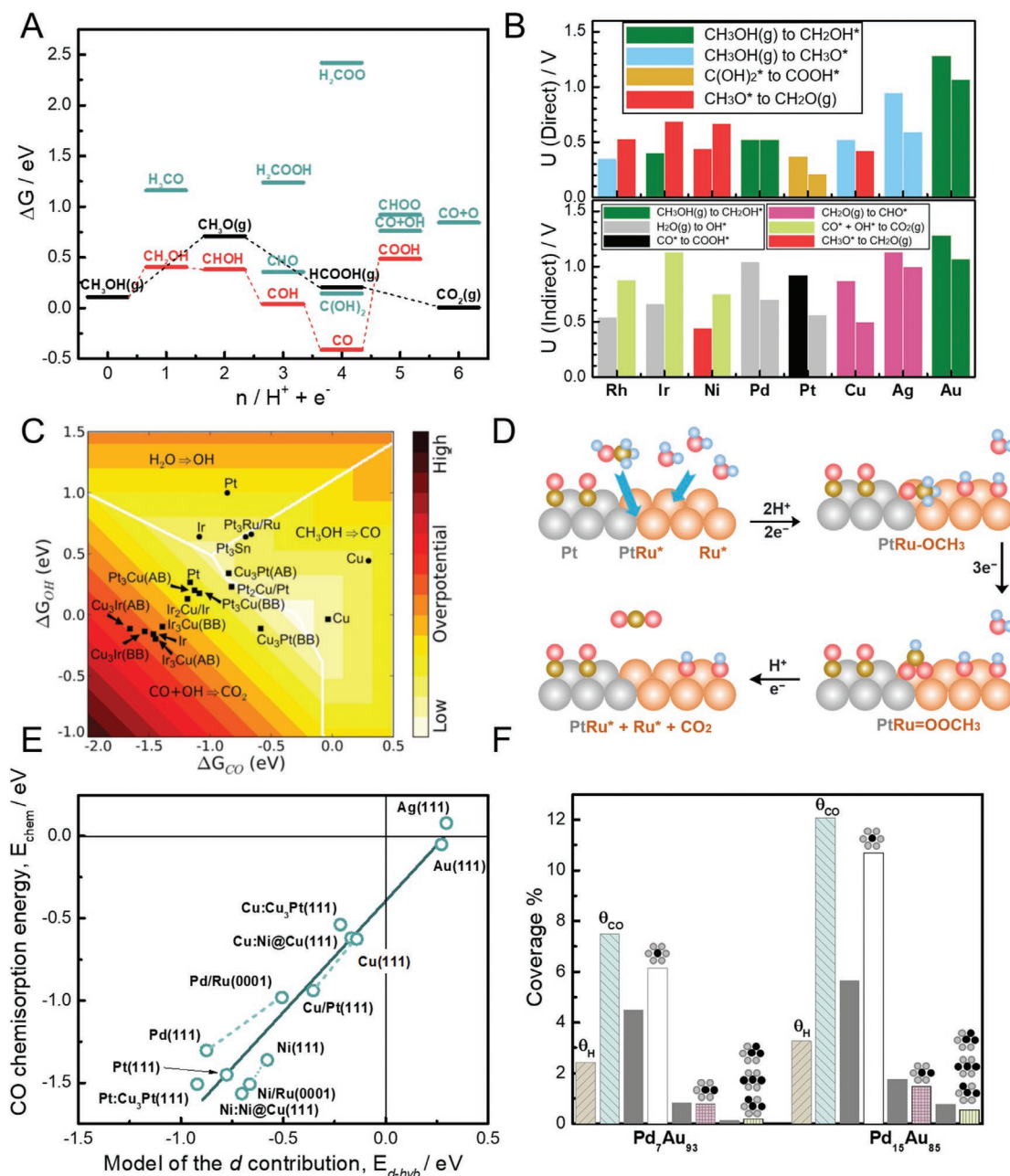
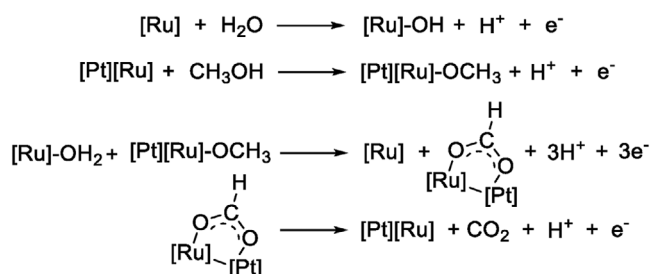


Figure 6. A) Free energies for the different intermediates on the Pt(111) surface, with $H_2(g)$, $CO_2(g)$, and $H_2O(g)$ as a reference. In red are the most stable intermediates for each step. The energy levels of gas and liquid-phase molecules, independent of the metal surface are shown in black. Intermediates with a higher energy are shown in blue. The x-axis indicates how many proton/electron pairs have been created from the original reactants (e.g., $CH_3OH + H_2O \rightarrow HCOOH(g) + 4H^+ + 4e^-$). Reproduced with permission.^[74] Copyright 2008, Elsevier. B) The onset potential and potential-determining steps for methanol electro-oxidation via the direct and indirect mechanisms on the (111) and (100) facets of 8 transition metals. For each metal, the first column represents (111) facet, the second column represents (100) facet. Top panel: direct mechanism; bottom: indirect (via CO^*) mechanism. The color of each bar indicates the potential-determining step, as explained in each legend. Reproduced with permission.^[75] Copyright 2009, American Chemical Society. C) Volcano plot for the indirect path on stepped (squares) and flat (circles) elemental surfaces and bimetallic alloys. The reference structures Ru_3Pt/Ru and Pt_3Sn are located on the border where the potential for water activation and oxidation of methanol to CO become equal to each other. Among the bimetallic catalysts studied, PtCu alloys show promising reactivity. Reproduced with permission.^[76] Copyright 2012, American Chemical Society. D) Representation of the proposed methanol electro-oxidation reaction mechanism on the act-PtRu/C. Reproduced with permission.^[77] Copyright 2015, Wiley-VCH GmbH, Weinheim. E) Hammer-Nørskov model analyses. Full DFT-GGA predictions versus model predictions on CO chemisorption. Reproduced with permission.^[78] Copyright 1996, American Physical Society. F) Surface coverages of Pd monomers, dimers, and trimers, as obtained from atomically resolved STM images (4000 alloy surface atoms were analyzed for each Pd content), the values expected for a random distribution (thin black bars), as well as corresponding H and CO coverages, derived from the electrochemical data. The error bars correspond to the statistical errors for $\theta_{Pd-Ensemble}$, to the uncertainties in θ_H due to double-layer correction and sulfate coadsorption, and to the errors in determining the CO oxidation charge for θ_{CO} , respectively. Reproduced with permission.^[79] Copyright 2001, The American Association for the Advancement of Science.

direct methanol fuel cell anode catalyst.^[81–83] A volcano plot of selected bimetallic alloys for indirect pathway is shown in Figure 6C, where the white spot represents the ideal catalyst that fulfils four conditions: a) active toward forming CO from methanol, b) activates water into OH* easily, c) binds moderately to both CO and OH, d) the potential $U_{\text{CO}} = U_{\text{OH}} = U_{\text{CO}_2} = 0$. Several model catalysts exhibit the reactivity very close to an ideal catalysts, such as Pt₂Cu/Pt, Pt₃Sn, Pt₃Ru/Ru, which with further tuning may give even higher reactivity.^[76] These predictions have been verified later by the same group, in which they have shown that by varying the Pt/Cu surface composition the methanol oxidation activity can be significantly improved.^[84]

More recently, Tong and co-workers proposed a revised methanol electro-oxidation pathway on PtRu different from the well-known Watanabe–Motoo mechanism. They suggested that the CO adsorbed on Pt sites is irrelevant but instead the Pt–Ru boundary sites facilitate the oxygen insertion that enhances the direct formate path.^[77] As shown in Figure 6D, the reaction pathways can be summarized with the following equations



[Ru] and [Pt] are active sites on their respective metals.

Apart from the bifunctional mechanism, bimetallic catalysts can also offer a further tuning of the catalyst's properties via ligand (electronic), strain, and ensemble effects, enhancing the intrinsic, specific and mass activity.^[85–87] The ligand effect refers to the heterometallic bonding interactions that could modify the surface electronic structure of the bimetallic catalysts. The strain effect stems from the change in the average bond lengths between different metal atoms, which causes surface strain. Both phenomena can affect the surface chemical properties by shifting the d-band center.^[88–90] Kitchin et al. performed DFT calculation on supported monolayer models, which have shown that there is a cumulative effect, in which both ligand and strain effects are responsible to the d-band width change, which alters the average energy and consequently affects the surface adsorption energy.^[91] Figure 6E presents the adsorption energy of CO on different mono- and bimetallic catalyst surfaces, in which it is clearly a scaling linear trend between the adsorption energy and the d-band center, same for atomic H and O.^[92] These scaling relations are sometime used to predict the ideal catalysts for methanol oxidation, as seen in the volcano plot in Figure 6C. Chan and co-workers performed theoretical investigations of transition metal Cu, Pt, and Ni surface energies under lattice strain and CO environment, in which they have found that the strain effects favor the formation of stepped terraces rather than low index facets such as (111), and the CO environment clearly favors such stepped facets.^[93]

The two effects above consider the situation where the adsorbate only is bond to one single elemental metal. Ensemble effect, on the other hand, takes into account the interaction with an ensemble of surface atoms. In such cases, the variation in the catalytic properties is related to both metals, and these ensemble sites can affect the activation barriers and thus change the reaction rates. By blocking the Pt(111) sites with cyanide, Cuesta has shown that at least three contiguous Pt atoms are needed to overcome the barrier to form CO from methanol.^[94] Neurock et al. examined the different ensemble requirements for three formic acid to CO₂ pathways, and have shown that significant differences on the activity can occur upon alloying.^[95] Because the indirect pathway (HCOOH* → CO* → CO₂) has much higher ensemble requirements (i.e., defect sites as well as a much larger surface ensemble in order to activate the C–O bond) than that for the direct and formate pathways, its reactivity can be greatly enhanced by the presence of Ru in the surface by adding the activation of water. While on the other hand, very small effect, if any, on the overall rates of oxidation can be expected from the presence of Ru. The combination of PdAu is a good example of ensemble effect. The role of atomic PdAu ensembles in electrocatalytic reactions have been investigated by Maroun et al., in which they combined in situ atomic resolution scanning tunneling microscopy and electrochemical adsorption and desorption of H and of CO stripping experiments.^[79] These techniques allowed the authors to reveal the distinct chemical properties of different ensemble structures, as shown in Figure 6F.

Therefore, three main contributions can be put forward for the higher reactivity of bimetallic electrocatalysts: i) the “bifunctional mechanism” where each metal promotes individual reaction steps; ii) the surface electronic structure changes affect the interaction with adsorbates; and iii) geometric ensembles both contributing to the same reactions. These contributions stem from how the alloy metal atoms are arranged, and may combine to enhance the overall oxidation activity. Above we have discussed how ensemble effects can affect the CO* formation,^[94,95] then in Figure 7 illustrates the reaction diagrams for CO oxidation over Pt and Pt–Ru alloy surfaces.^[96] Compared to pure Pt(111) surface (Figure 7A), the inclusion of Ru atoms in the surface facilitates the H₂O → OH* process, but the increase of the CO* + OH* coupling barrier decreases the rate of CO oxidation, indicating a pure bimetallic effect does not work solely to enhance the reaction rate (Figure 7B). A Ru substrate under the Pt monolayer however, slightly increases the endothermicity of OH* formation, but reduced the barrier for the CO* + OH* coupling significantly due to ligand effect (Figure 7C), thereby improves the CO oxidation rates. In Figure 7D where combines the PtRu surface alloy and the pseudomorphic Pt monolayer over Ru, a smaller reaction energy for water oxidation and CO* + OH* coupling energy can be observed. This indicates that both bifunctional and ligand effects may combine to improve the CO oxidation rate.

As the carbon chain becomes longer in many other biomass molecules, the reaction mechanism becomes even more complex, due to the involved C–H, C–C, and C–O bond breaking, which leads to a variety of intermediate products. It should be pointed out that the electrosynthesis process is not always potential controlled, as some of the reaction follows an “EC”

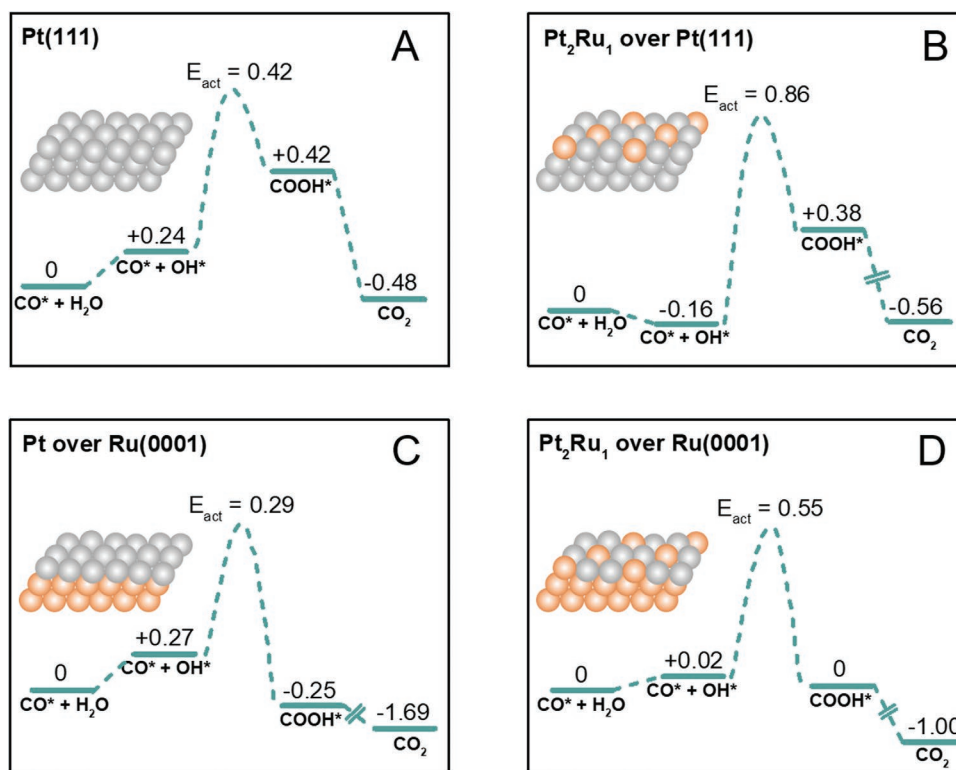


Figure 7. Reaction energy diagrams for CO oxidation over Pt and Pt–Ru alloy surfaces. A) Pt(111), B) Pt₂Ru₁ monolayer over a Pt(111) substrate, C) Pt monolayer over a Ru(0001) substrate, and D) Pt₂Ru₁ monolayer over a Ru(0001) substrate. All energies were computed with 3*3 surface cells. Reproduced with permission.^[96] Copyright 2007, Springer. Inserted are illustrations of the atomic arrangements of each model.

mechanism: an electron transfer reaction is in equilibrium, followed by an essentially potential-independent chemical step, for example, the aldehyde oxidation into carboxylic acid under alkaline condition.^[97] Herrero et al. examined the Tafel slope of such reactions and interpreted that a value of 120 mV dec⁻¹ indicates the first electron transfer is normally the rate-determining step, whereas a value of 60–80 mV dec⁻¹ is associated with a chemical step after the first electron transfer.^[98] Therefore, it is also necessary to consider the chemical activities of different metals, in which the electrolyte pH plays an equally important role as the applied potential.

Alcohol oxidation proceeds through the sequential removal of two hydrogen atoms (H_{α} from O–H and H_{β} from C–H) and electrons into a carbonyl. The resulting carbonyl can convert into a geminal diol with H₂O, and be further oxidized into a carboxylic acid, as illustrated in **Figure 8A**. Although it follows a similar mechanism than alcohol oxidation, aldehyde oxidation can occur without catalyst under air and alkaline conditions.^[99]

If H_{β} abstraction is faster than H_{α} abstraction, the reaction rate will be pK_a-dependent. Considering that for most alcohols their pK_a is above 14, alkaline conditions will give better results than in acidic conditions.^[65] This pH-dependent phenomenon is also seen for CO₂ reduction reactions and have been extensively studied with DFT by Chan's group. Illustrated in their work, the pH effect can affect the reactant adsorption by dipole-field interactions.^[100–103] The interfacial electric field at an electrochemical interface, determined by the absolute potential (e.g., on a standard hydrogen electrode scale), stabilizes the

polar reactants and intermediates such as CO₂*. A given field stabilization is consistent with a more positive overpotential at higher pH, which results in higher reaction activity at higher pH.^[101] A good example of this field stabilizing effect is the local cation-induced change on adsorbed CO₂,^[104–106] which have been observed for different alcohol oxidation as well.^[107–110] This proves the appliance of such theory for alcohol electro-oxidation, which should be further adapted and adjusted to explore the reaction mechanisms of such reactions.

Au is inactive in acidic conditions, despite its capacity to form –OH groups on the surface at high potentials (Figure 8B(a)).^[26,111] Even in alkaline conditions Koper et al. have extensively shown that Au cannot perform H_{α} abstraction, as it is performed by the hydroxide ions in solution.^[65,112–114] The presence of Au is needed for H_{β} abstraction through the surface-bonded hydroxides, with Au acting as an electron acceptor.^[99] This second step is faster than H_{α} abstraction, and in the specific case of Au, Koper and co-workers showed that adsorbed CO could act as a promoter for this step.^[115] In contrast with Pt and Pd, the full d-band of Au makes it less active to bind oxidation intermediates, but also prevents CO poisoning and –OH saturation at the surface.^[116] At potentials above 0.9 V_{RHE}, Au can further adsorb intermediates through the carbon, allowing further C–C cleavage.^[117]

Unlike other metals, Pt and Pd are directly active for C–H bond cleavage, making the H_{β} abstraction step faster than H_{α} abstraction, even under acidic conditions (Figure 8B(b)). Indeed, Lamy and co-workers showed that Pt could directly

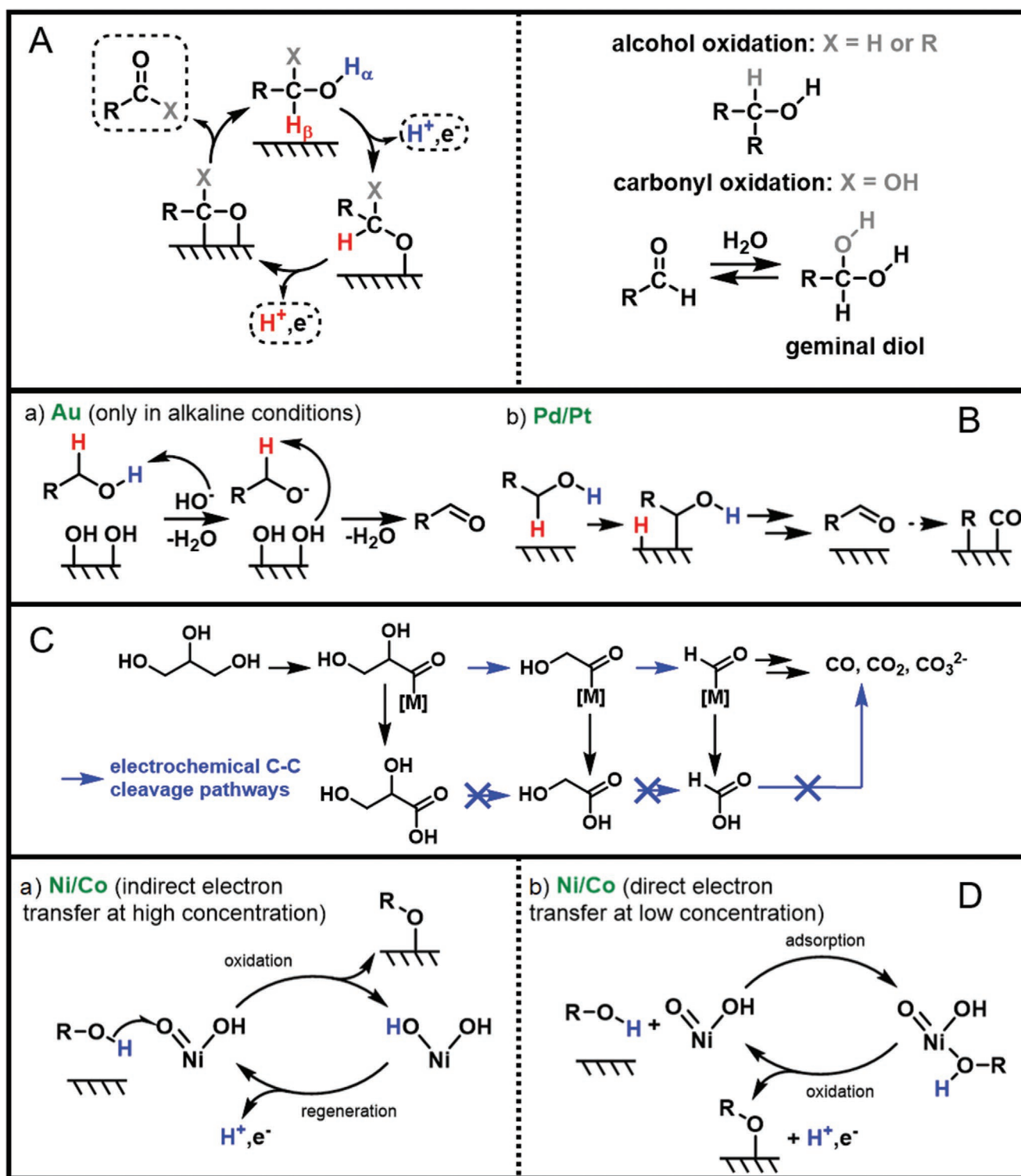


Figure 8. A) General steps for alcohol and aldehyde electro-oxidation. B) Alcohol oxidation mechanisms for novel metals: (a) Au, (b) Pt/Pd. C) Glycerol oxidation C–C bond cleavage mechanism. D) (a) Indirect and (b) direct oxidation mechanisms of alcohol over Ni/Co-based electrocatalyst surface.

cleave C–H bond in acid at potentials below $0.75 V_{\text{RHE}}$, both for EtOH and glycerol.^[118,119] At potentials above $0.8 V_{\text{RHE}}$, oxygenated species form at the surface (PtOH, PtO) and are responsible for H_{β} abstraction.^[120,121] This phenomenon has also

been confirmed with DFT simulation of ethanol oxidation over Pt(111) surface.

Pt and Pd have been shown to be highly active for C–C bond cleavage in electrocatalytic conditions, by adsorbing

intermediates through the carbon.^[122] While higher overpotentials and high basicity favor C–C cleavage for Pd, the opposite effect happens for Pt.^[123] C–C cleavage potentially leads to selectivity loss and CO poisoning,^[80,124] that can only be overcome by applying high enough potential to further oxidize CO_{ads} into CO₂.^[125] Fernández et al. employed *in situ* FTIR and isotopically labeled glycerol (¹³CH₂OH–¹²CHOH–¹³CH₂OH) to investigate the C–C bond cleavage and CO₂ formation on Pt in acidic media.^[120,126,127] They have found out that the terminal ¹³CH₂OH groups are easier to electro-oxidize and can happen at low potentials around 0.3 V_{RHE}, while the mass production of ¹²CO₂ from the central ¹²CHOH group can only be observed above 1.2 V_{RHE}. Li and Harrington covered in detail glycerol electro-oxidation mechanism through an overview of previous studies. In particular, they argued that C–C cleavage mostly occurs directly on glycerol and its adsorbed decomposition intermediates, as shown in Figure 8C, rather than on the desorbed C₂/C₃ products (such as glyceraldehyde, dihydroxyacetone).

For Ni and Co two reaction mechanisms were proposed, as illustrated in Figure 8D: i) direct electron transfer in which alcohol molecules adsorb on the M(OH)₂ and get oxidized by the OH[−] ions trapped on the surface; ii) indirect electron transfer from the reactant to MOOH, restoring the M(OH)₂.^[128–130] The works reported by Fleischmann et al. in 1970s point toward the indirect reaction pathway.^[131,132]

At lower glycerol concentration though, Houache et al. observed direct electron transfer pathway for Ni.^[133] This was confirmed by Taitt et al. for HMF, as they observed another oxidation peak in linear sweep voltammetry (LSV) above the potential of Ni(OH)₂ oxidation to NiOOH.^[134] Under these conditions, oxidation rate becomes dependent of potential.^[128]

With the above knowledge at hand, in the following sections we will review in detail for different organic molecules, how the choice of electrocatalysts will affect the reaction activity and selectivity.

4.2. Selective Electro-Oxidation of Glycerol

Glycerol, a byproduct from the biodiesel industry, is recognized by the U.S. Department of Energy (DOE) as one of the top ten biomass-derived platform molecules for the production of high-value chemicals.^[135] Amongst them, the partial oxidation derivatives, such as glyceraldehyde, glyceric acid, and dihydroxyacetone, are widely used in the cosmetics, pharmaceutical, and food industry.

The electrocatalytic oxidation of glycerol allows generating both value-added chemicals and hydrogen concomitantly, sparking much attention over the last decade. This concept was first introduced by Shen and co-workers, who adapted the technology applied to direct alcohol fuel cells for an alkaline electrolyzer with Pd–(Ni–Zn)/C on Ni mesh as anode, and commercial Pt/C on carbon paper as cathode.^[23] At current density of 40 mA cm^{−2}, H₂ and over 70% glycerate and tartrate chemicals were produced with 10 wt% glycerol in 2 M KOH electrolyte. The voltage needed for glycerol electrolysis is 0.6 V compared to 1.58 V for water electrolysis, and the power consumption for H₂ production is 1.43 kWh Nm_{H₂}^{−3}, less than

half of what is needed for water electrolysis (3.78 kWh Nm_{H₂}^{−3}). Since then, increasing efforts have been made to understand glycerol electro-oxidation reaction pathways over different metal catalysts to achieve high energy efficiency for H₂ production, high glycerol conversion rate and tunable selectivity.^[40,43,136]

Glycerol can be oxidized at different carbon atoms within its structure.^[86] Figure 9A illustrates the identified general oxidation pathways, but the nature of different metal catalysts can largely affect the chemical transformation processes, as summarized in Section 4.1.^[137] Presented here are the most favorable routes in each step, however, many factors, such as the electrolyte pH and the structure of catalysts can largely affect the reaction routes.

4.2.1. Platinum Catalysts

The glycerol oxidation on Pt catalysts goes through multiple steps. DFT calculations showed that energy barriers for C–H/O–H bond cleavage steps are significantly lower than those for C–C or C–O bond cleavage steps (by more than 0.5 eV).^[138] Hence on Pt(111), early in the decomposition process, both C–C and C–O bond cleavage will be kinetically slow compared to dehydrogenation reactions. After several steps of dehydrogenation, C–C bond breaking energy barriers are lowered, allowing further oxidation to occur.

Glycerol oxidation on Pt follows the principle summarized in Section 4.1 but tends to exhibit different product selectivity in basic and alkaline conditions. As shown in Figure 9B, which summarizes the product concentration change during anodic potential scan, it can be concluded that the acidic media leads to a lower activity but provides more favorable conditions for selective alcohol oxidation, while alkaline condition promotes over oxidation to various products.^[26]

The structural properties of Pt, such as crystal structure, particle sizes, defect density, and exposed high-index facets can also influence the activity and reaction pathways. First, the Pt surfaces structure has a strong impact on promoting primary and secondary alcohol oxidation in acidic media.^[125] As shown in Figure 9C, Pt(111) and Pt(100) surfaces exhibit different binding modes of dehydrogenated glycerol. On the close-packed Pt(111) surface, an enediol-type intermediate is formed, whereas the Pt(100) forms a Pt=C bond with glycerol. The first intermediate results in a mixture of dihydroxyacetone and glyceraldehyde, while only glyceraldehyde is obtained through the second intermediate. Second, downsizing the Pt nanoparticles can bring higher specific activity because of the enlarged density of active sites. Kim and co-workers incorporated Pt nanoclusters in microporous 3D graphene-like carbon and improved the glycerol conversion to 7.7%, compared to 2.3% with commercial Pt/C.^[139] The as-prepared catalyst also enhanced the further oxidation of glyceraldehyde to glyceric acid. The enhanced glycerol electro-oxidation performance is attributed to the increase of Pt active sites and the physicochemical properties of Pt by interacting with the 3D carbon structure, resulting in a reduction in the absorption energy toward glycerol. Third, high-index facets lead to maximizing the active site exposure. By intercalating Pt growth within few-layered graphene, Loh and co-workers fabricated Pt-sandwiched vertically erected graphene nanowall

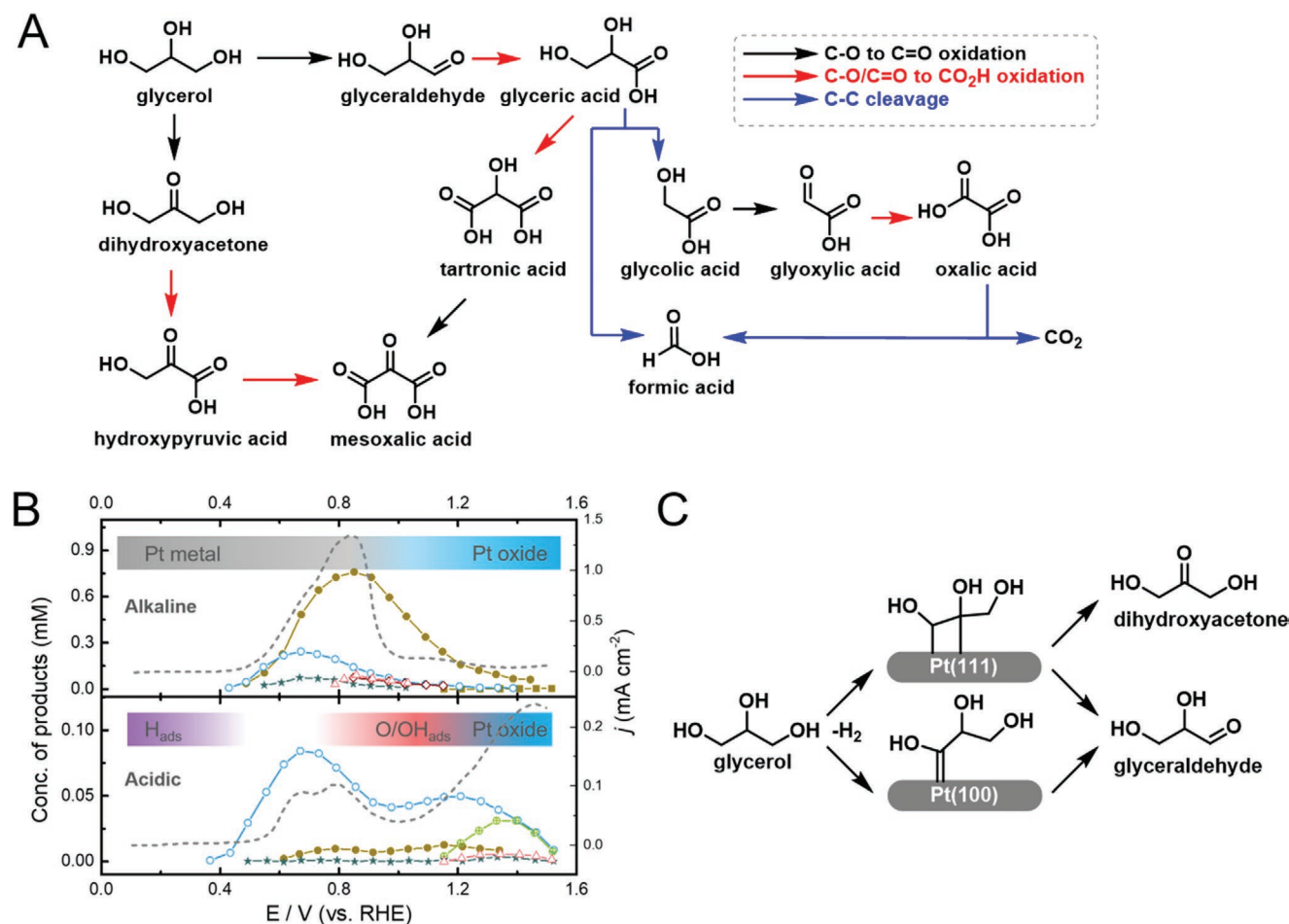


Figure 9. A) The general reaction pathways of glycerol oxidation over metal catalysts in electrochemical processes. B) Glycerol (0.1 m) electro-oxidation product on Pt electrode in 0.1 m NaOH (alkaline) and 0.5 m H₂SO₄ (acidic) media during linear sweep voltammetry with a scan rate of 1 mV s⁻¹ (dashed line: current density; ●: glyceric acid; ○: glyceraldehyde; ☆: dihydroxyacetone; ◇: tartronic acid; ⊕: formic acid). The bar inserted indicate the ion adsorption and Pt oxidation states under different potentials. Reproduced with permission.^[26] Copyright 2011, Wiley-VCH GmbH & Co. KGaA, Weinheim. C) Pt(111) and Pt(100) difference for glycerol oxidation selectivity. Reproduced with permission.^[25] Copyright 2016, American Chemical Society.

electrodes with superior mass activity of 2.91 A mg_{Pt}⁻¹ and a 79% selectivity toward formate at 60 °C.^[140] The high catalytic activity and C–C bond cleaving ability stem from the high-index facets (100)/(111)/(100), resulting in a high active site density and utilization.

4.2.2. Palladium catalysts

Pd possesses similar catalytic activities to Pt while being at least 50 times more abundant on earth than Pt. In contrast with Pt, studies on Pd-based electrocatalysts mostly focused on different supporting materials. In an early report by Vizza and co-workers, Pd nanoparticles supported on multiwalled carbon nanotubes (Pd/MWCNTs) showed superior catalytic activity toward glycerol electro-oxidation compared to commercial Pd/C. This can be associated to the efficient dispersion of metallic particles and intrinsic properties of MWCNTs in facilitating glycerol diffusion to the catalyst surface during this diffusion-controlled process.^[141] Wang and co-workers used a hybrid support consisting of graphitic carbon nitride (CN)

and graphene to fabricate Pd-CN_x/G electrocatalyst with high selectivity toward C₃ products.^[142] The authors suggested that the interaction between Pd and nitrogen atoms weakened the adsorption ability of Pd toward C₃ products, especially glyceric acid, thus preventing their further oxidation. In a recent study, Pd nanoparticles have been deposited on PEDOT-coated graphite electrodes via electroless deposition, an autocatalytic process where the electrode develops a potential in a plating solution containing different polymerization charges and different doping ions (polystyrene sulfonate (PSS) and dodecyl sulfate).^[143] The Pd/PEDOT-PSS catalyst showed a high mass activity for glycerol electro-oxidation in alkaline condition owing to the high specific metal loading, which diminishes with increasing Pd content as a result of impeded access of glycerol or nanoparticles aggregation.

4.2.3. Gold Catalysts

Pd or Pt electro-oxidation catalysts suffer from deactivation due to overoxidation and poisoning from CO-like intermediates.

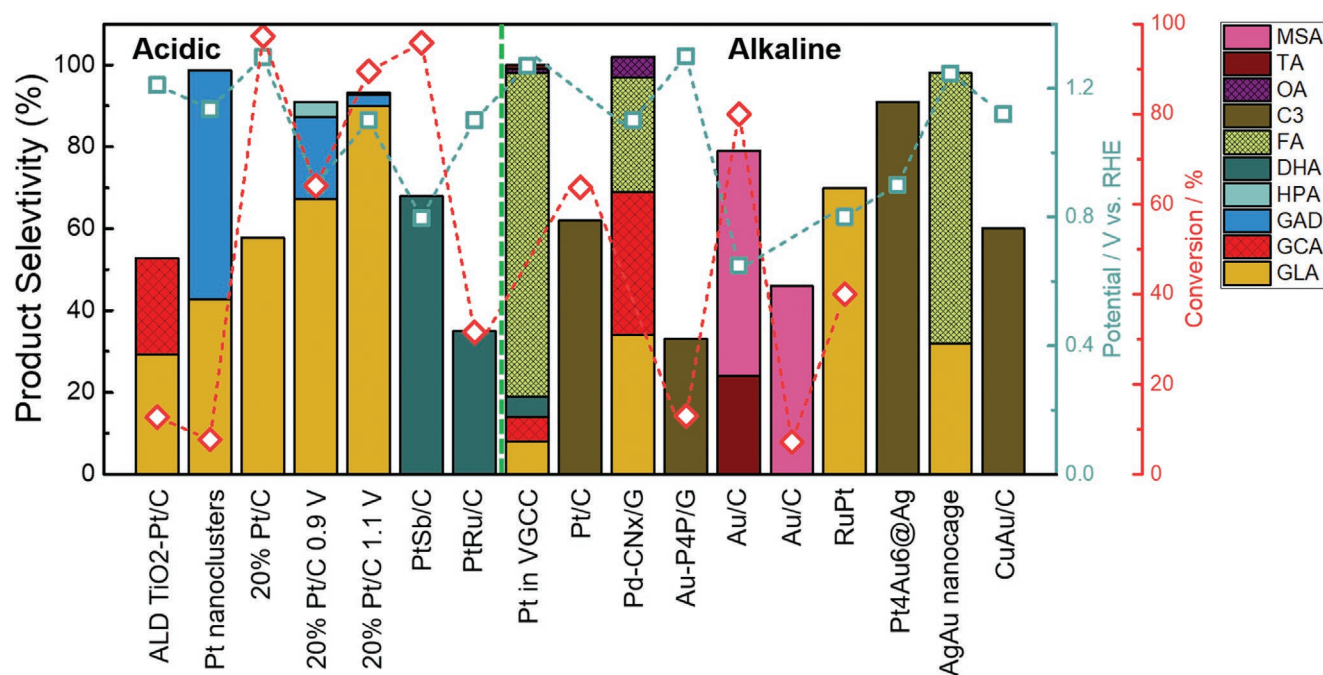


Figure 10. Operating potential, glycerol conversion, and product selectivity of various catalysts in acidic and alkaline conditions. (GLA: glyceric acid, GCA: glycolic acid, GAD: glyceraldehyde, HPA: hydroxypyruvic acid, DHA: dihydroxyacetone, FA: formic acid, C3: three carbon products, OA: oxalic acid, TA: tartronic acid, MSA: mesoxalic acid; products are the corresponding acids in their salts form for alkaline conditions.) Detailed reaction conditions are included in Table S12 of the Supporting Information.

On that note, Au as an electrocatalyst often exhibits high stability,^[115] a key feature for potential commercialization.^[144] In contrast with platinum group metals (PGMs), CO acts as a promoter for Au on its surface rather than a poison. Koper and co-workers have demonstrated that CO is irreversibly adsorbed on Au(111) surfaces in aqueous basic condition, promoting the electrocatalytic oxidation of certain alcohols, in particular methanol.^[115] Adsorbed CO promotes β -hydrogen elimination to accelerate C–H bond breaking and the coadsorption of alcohols. The slower surface oxidation of Au compared with Pt allows to apply higher effective overpotential,^[26] and its unique mechanism for H extraction, as discussed in Section 4.1, determined the selective formation of glyceric acid at low potentials (0.6–0.8 V_{RHE}) and glycolic acid at high potentials (0.8–1.5 V_{RHE}).^[26,145–147]

A summary of different catalysts' performance for glycerol oxidation is shown in **Figure 10** and Table S12 (Supporting Information), which clearly shows that higher product selectivity can be achieved in acidic conditions.

4.2.4. Alloys

The fabrication of bimetallic or trimetallic electrocatalysts can help lower noble metal consumption as well as improve the activity and selectivity toward glycerol oxidation by the three effects discussed in Section 4.1.

As an example of the contribution from bifunctional mechanism, a PtRu catalyst was reported to show excellent activity and stability for glycerol electro-oxidation during CV and long-term chronoamperometry tests.^[148] The catalyst exhibited larger

forward-to-reverse peak current density ratio (I_f/I_r) during CV scan, indicating less intermediate accumulation, due to the partially oxidized Ru surface as confirmed by X-ray photoelectron spectroscopy (XPS) Ru (3p) spectra. The higher chronoamperometry end current compared to commercial Pt/C also suggests a higher tolerance toward CO-like poisoning species and decelerated catalyst deactivation. The shift in the density of Pt vacant d-orbital states due to the presence of Ru can also affect the glycerol binding energy with a volcano-shaped relation to the catalytic glycerol oxidation activity.^[73] It should be noted that Ru/C was shown to be inert for glycerol electro-oxidation.^[149]

A similar strategy can also be applied to Pd-based catalysts.^[149–151] PdRu nanocages developed by Xia and co-workers exhibited an alloy surface with hollow interiors, ultrathin (i.e., 2.5 nm) and porous walls which increased the atomic efficiency of metal atoms, achieving a 6.2-fold enhancement of catalytic mass activity relative to the commercial Pd/C.^[149]

In terms of the contribution from surface electronic structure, a bimetallic PdPt nanowire network showed forward current density of 0.086 A cm^{-2} , 1.8-fold higher than that of Pt/C.^[152] The measured electrochemical active surface area of PdPt nanowires was lower than that of Pt/C, indicating that the higher activity did not stem from higher specific activity, but from improved intrinsic catalytic properties. By fitting the linear plot of current density at the anodic scan peak versus the square root of scan rate, a higher slope value could be derived for PdPt nanowires relative to Pt/C, suggesting that bimetallic catalysts showed an improved electro-oxidation kinetics and should account for the higher catalytic activity.^[153]

Combining noble metals with early transition metals constitutes another way of designing bimetallic electrocatalysts

while reducing the noble metal content.^[154,155] The alloyed 3d metals can also downshift the *d*-band center of Pt/Pd atoms, resulting in a weaker bonding to the surface intermediates and/or products thus increasing the stability.^[92,156,157] Pt alloys based on Ni, Fe, Co, and Cu have all shown remarkable catalytic performances toward glycerol electro-oxidation, with their mass and specific activities 2–7-fold higher than commercial catalysts.^[158–162] Similarly, PdNi catalysts feature a large negative shift of the onset potential due to the oxidative desorption at low potential, involving a OH⁻ transfer from Ni(OH)₂ to adsorbed organic molecules on the Pd active sites.^[163] However, the authors failed to explore the product selectivity in such bimetallic catalysts, which is expected to be distinctive given the unique electrocatalytic preferences of those transition metals in oxygen reduction reaction (ORR), OER, HER, and CO₂ reduction reaction (CO₂RR).^[164] On that note, a study by De Andrade and co-workers which compares the performance of Ni@Pt/CNTs, Ru@Pt/CNTs, and Sn@Pt/CNTs toward glycerol oxidation has shown the importance of investigating catalytic activity as well as product selectivity of different

metal catalysts.^[165] They found that even though Ni@Pt/CNTs had the lowest onset potential and highest current density, the detected products and mass balance after 12 h was lower than Ru@Pt/CNTs, which may be due to complete oxidation to C₁ products.

The combination of PdAu is a good example of ensemble effects, which refers to the variation in the catalytic property of an ensemble and have been reported to show promising catalytic activity toward alcohol oxidation.^[168–173] Au can further determine product selectivity. For example, Au–Pd favored the oxidation of terminal hydroxyl groups (glycerate and tartro-nate), while Au–Pt favored C–C breaking to form glycolic acid.^[144] Besides, Au can significantly diminish Pt and Pd deactivation and decreases hydrogen adsorption to Pd, improving the catalyst reusability.^[174] DFT calculations studying the glycerol absorption models on bare and transition-metal surface-alloyed Au(111) have shown a negative correlation between the strength of glycerol molecule adsorption and the *d*-band center of surface layer of transition metal surface-alloyed Au(111), as shown in Figure 11A.^[166] Wan and co-workers demonstrated

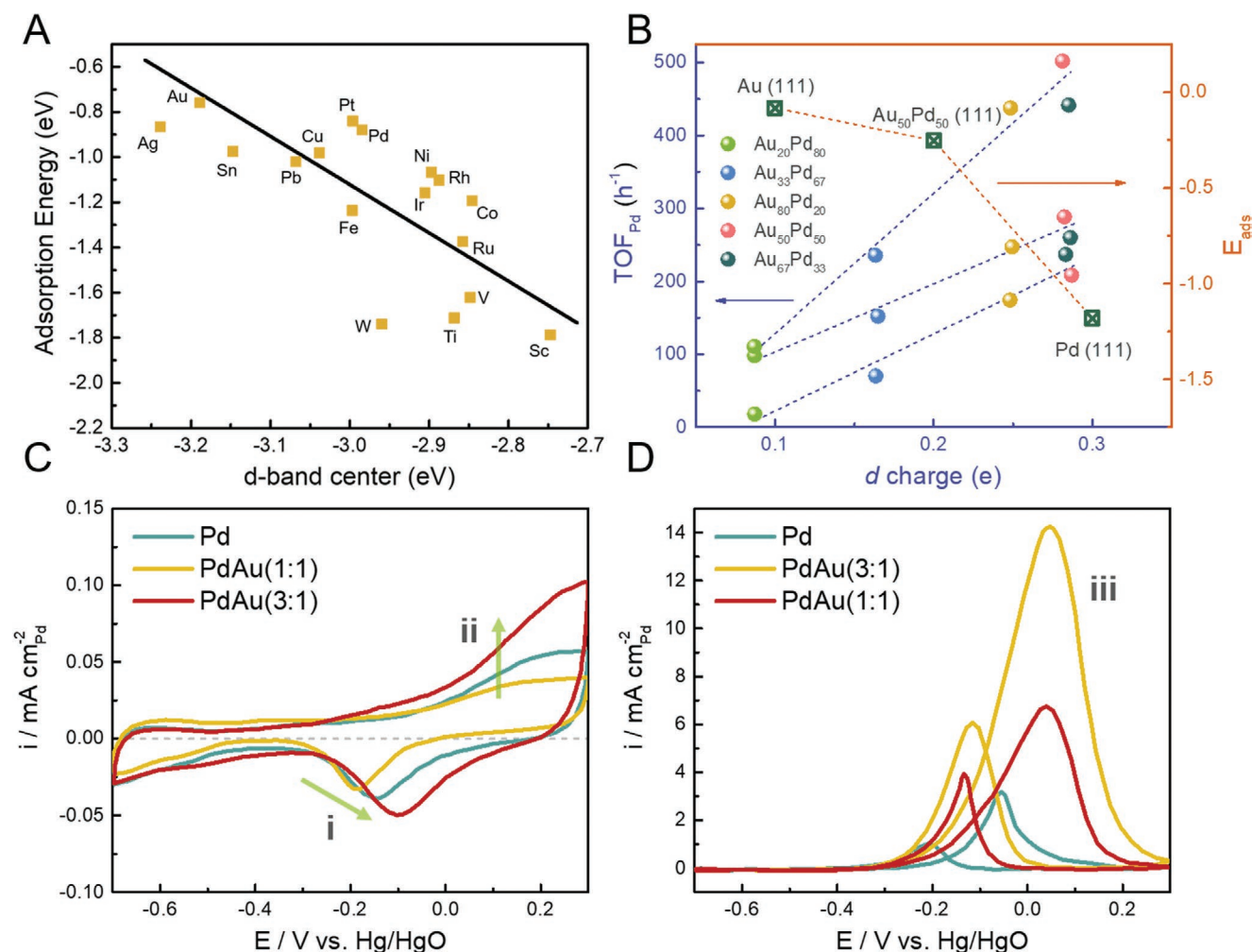


Figure 11. A) Glycerol adsorption energy (eV) on transition-metal alloyed Au(111) surface as a function of the calculated *d*-band center (eV). Reproduced with permission.^[166] Copyright 2016, American Chemical Society. B) Relationship between the *d*-charge gain at Pd site (orange line) and TOF_{Pd} of the AuPd alloys (navy line). Reproduced with permission.^[167] Copyright 2019, Nature Research. CVs of Pd, PdAu (3:1), and PdAu (1:1) electrodes in an Ar-saturated 1 M KOH solution C) without and D) with 0.5 M glycerol at room temperature. Reproduced with permission.^[168] Copyright 2015, Elsevier.

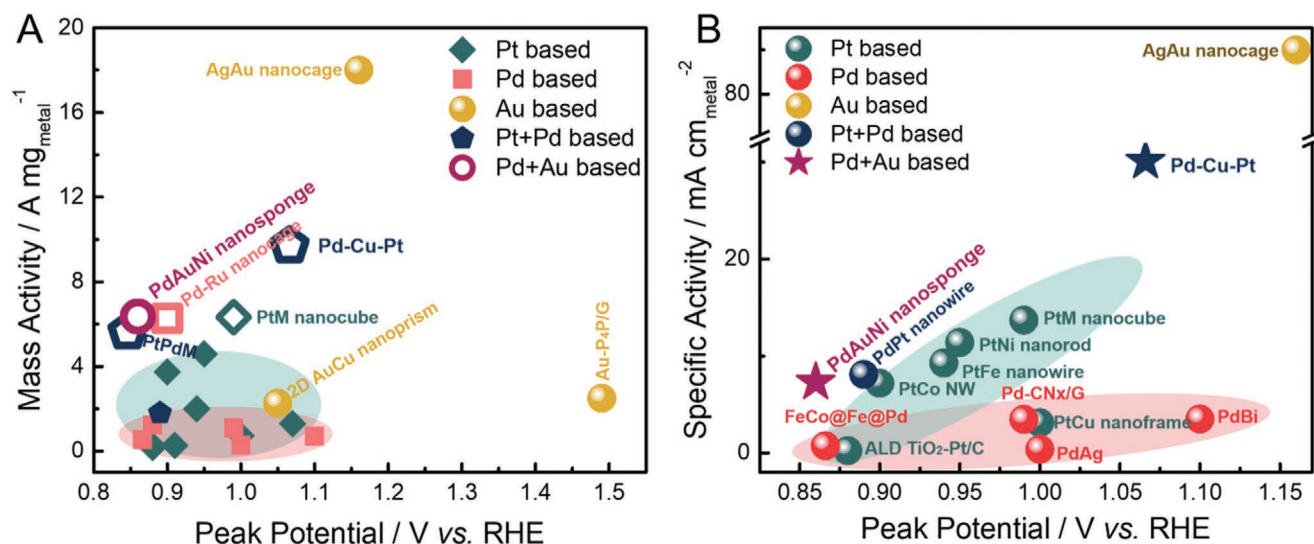


Figure 12. An overview of state-of-art glycerol oxidation catalysts. A) Mass and B) specific activity different catalysts in alkaline electrolyte (except ALD TiO₂-Pt/C, which was tested in 0.5 M H₂SO₄ + 2 M glycerol). The peak potential represents the potential where the electrocatalysts exhibit the highest current density. Presented data were originally reported as follows: PdAuNi nanosponges,^[177] Pd-Ru nanocages,^[149] Pd-Cu-Pt,^[178] PdPt nanowires,^[152] PdBi,^[179] Pd-CNx/G,^[142] PdAg,^[163] FeCo@Fe@Pd,^[180] PtPdM,^[181] PtM nanocubes,^[161] PtNi nanorod,^[160] PtFe nanowires,^[158] PtCo nanowires,^[159] PtCu nanoframes,^[162] 2D AuCu nanoprisms,^[182] Au-P4P/G,^[183] AgAu nanocage.^[154]

a similar behavior by examining the electronic structure of monodispersed AuPd catalysts with continuous change in Pd-Au coordination numbers. X-ray absorption near edge structure and XPS confirmed that the surface Pd atoms obtained d-charge gain from Pd-Au bonds, corresponding to a decrease in d-band center of Au. DFT calculation indicated that the maximum d-charge gain in Pd led to a pronounced improvement in the adsorption strength of primary alcohols and therefore higher activity and selectivity toward the oxidation of various alcohols, with the maximum turnover frequency (TOF) shown in Figure 11B.^[167] In terms of electrochemistry, the CV of PdAu in Figure 11C,D suggests that increasing Au content leads to the positive shift of both the PdO reduction peaks (i) and glycerol oxidation peaks (iii), while the current increase at Pd-OH_{ads} formation (ii) and PdO reduction peak (i) suggests that alloying Pd with Au lead to a higher amount of OH adsorption, due to the ensemble effect between Pd and Au. The authors did not provide detailed explanation on the ensemble effects induced by Au alloying. However, according to other reports on Pd-Au ensemble electrocatalysts, we assume the ensembles of Pd and Au have resulted in an average decrease in the binding energy of O and OH radicals, resulting in the easier oxygen removal during reduction scan while higher energy requirements for oxygen insertion for glycerol oxidation.^[175,176] The higher amount of OH adsorption, on the other hand, favors the glycerol oxidation and leads to the higher current density.^[168]

Figure 12 compares the electrochemical performance of different catalysts reported in various literature. Pd-based electrocatalysts in general exhibit low mass/specific activity while Pt-based electrocatalyst show increased activity with higher peak potential, i.e., higher kinetics. Au, on the other hand, is more unpredictable, and therefore its catalytic performance will largely be determined by the alloying metals and the catalyst morphology.

4.2.5. Ternary Catalysts

Trimetallic electrocatalyst can combine the different mechanisms mentioned above, and offer even more flexibility toward catalyst tuning.^[177,178,180,184-187] As a result, ternary catalysts are among the ones exhibiting higher mass and specific activities with low peak potential (Figure 12). For example, Kim et al. developed a PtRuSn/C ternary electrocatalyst with atomic ratio of 5:4:1.^[188] By comparing trimetallic PtRuSn/C with bimetallic PtRu/C and pure Pt/C, the authors determined the complementary roles of Ru and Sn in removing CO-like poisoning species (Figure 5C). PtPd alloyed with 3d metals (Fe, Co, Ni) have been reported to exhibit good glycerol electro-oxidation activity due to the further tuned electronic and surface strain effects by transition metals. With lower metal loading, PtPdNi showed the highest mass activity (5.63 A mg_{Pt+Pd}⁻¹) toward glycerol oxidation, 5.4 times higher than commercial Pt/C and Pd/C catalysts.^[181] Furthermore, the introduction of Cu in Pd-Cu-Pt electrocatalysts exhibit remarkable CO tolerance, as observed from the delayed CV peak during in situ CO-oxidation and the absence of CO intermediate adsorbates during in situ FTIR, due to the presence of surface Cu atoms that promote oxygen species (*OH) formation.^[178]

4.2.6. p-Block Metals

Bi, Sb, Sn, and Pb have been widely used in glycerol oxidation to improve the Pt oxidation selectivity via geometric blocking effect, electronic structure alternation, or intermediate molecule stabilization.^[189-193] Kwon et al. adsorbed Bi atoms on a Pt surface and found that glycerol was nearly 100% converted to dihydroxyacetone at 0.5–0.6 V_{RHE}.^[194] This selectivity was attributed to Bi blocking the pathway for primary oxidation but also to Pt-Bi surface active sites that poised for secondary alcohol

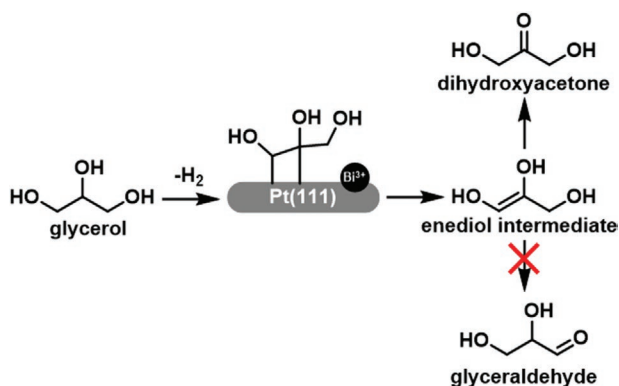


Figure 13. Selectivity to dihydroxyacetone induced by Bi adsorbed on Pt(111) surface. Reproduced with permission.^[194] Copyright 2012, American Chemical Society.

oxidation. Further studies showed the interaction of the Bi adatom with the enediol intermediate, driving selectivity toward the most stable isomer dihydroxyacetone (Figure 13).^[195,196]

The same group showed that irreversibly deposited Sb on Pt/C was the most promising modifier for selective production of dihydroxyacetone, with a low onset potential and enhanced peak current density.^[197] By contrast, Sb in solution (via reversible adsorption) completely inhibited glycerol oxidation. Similarly,

Fernández and co-workers demonstrated the irreversibly adsorbed Bi,^[193] Pb,^[198] and Sb^[192] atoms on Pt results in higher activity in alkaline than in acidic media, due to a higher stabilization of the negatively charged intermediates by the positively charged adatoms. Other bimetallic PtSb/C,^[199] PtSn/C,^[200,201] and Pd_xBi^[179] alloys have also been investigated, with a similar promotion mechanism from ligand effects as discussed in the previous sections.

4.2.7. Earth-Abundant Elements

Earth-abundant element based electrocatalysts for electrochemical alcohol oxidation have been studied to potentially replace the expensive and rare noble metal-based catalysts. Among them, Ni-based catalysts have received increased attention due to their competitive price, high stability in alkaline media, low poisoning effect, and high catalytic activity toward various alcohol oxidation.^[204–208] Akin to Ru, Ni possesses the capability of generating efficient OH_{ads} at lower overpotential and thus facilitates oxidative desorption of the intermediates. The reaction pathways of glycerol oxidation over Ni electrodes are similar as described in Figure 8D, which can take place via direct and indirect electron transfer process. Here the absence of a cathodic peak associated to β-NiOOH to β-Ni(OH)₂ transformation in Figure 14A, as observed by Bott-Neto et al. and Baranova

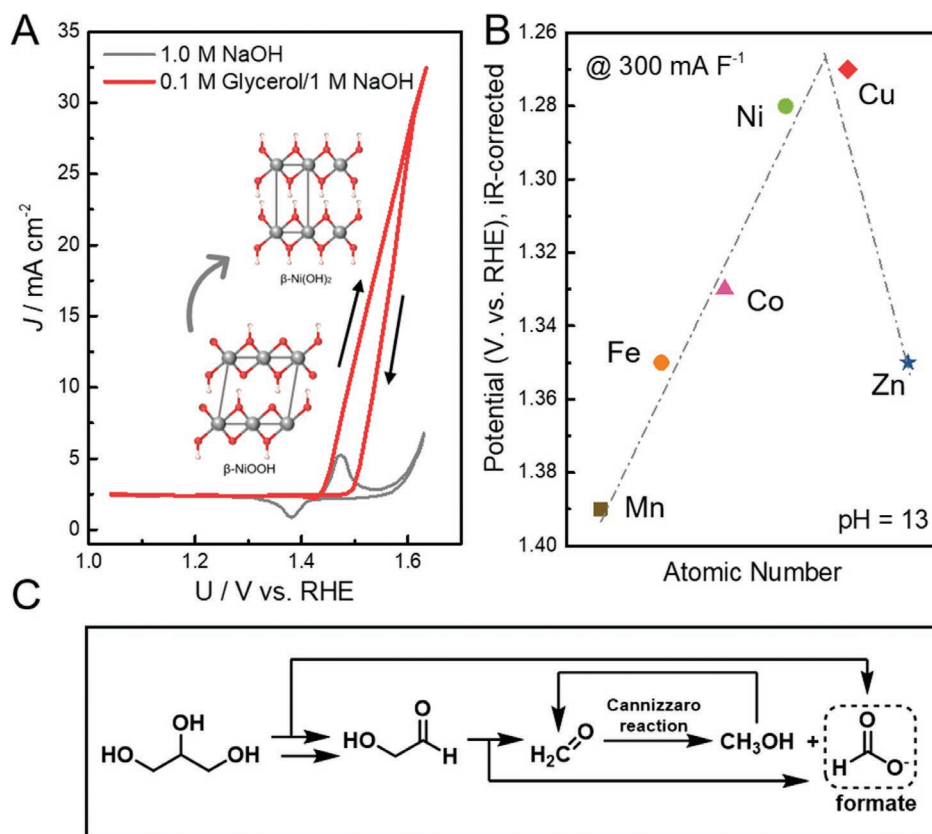


Figure 14. A) CV of Ni electrode in 1 M NaOH in the absence and presence of 0.1 M glycerol at 50 mV s⁻¹. Reproduced with permission.^[202] Copyright 2019, American Chemical Society. B) The intrinsic glycerol oxidation activity trend within the series of MCO₂O₄ (M = Mn, Fe, Co, Ni, Cu, Zn) catalysts (in the order of increasing atomic number of M from left to right). Reproduced with permission.^[135] Copyright 2020, American Chemical Society. C) Proposed mechanistic scheme for glycerol oxidation to formate on Ni-Mo-N/CFC in alkaline medium. Reproduced with permission.^[203] Copyright 2019, Nature Research.

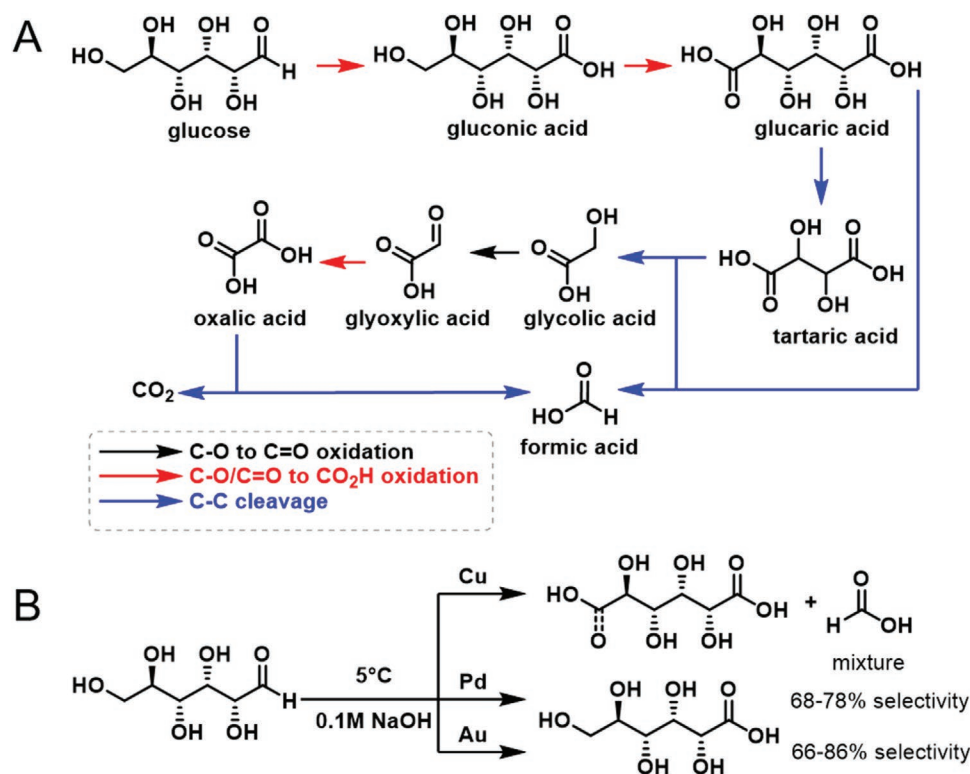


Figure 15. A) Glucose electro-oxidation pathways. B) Glucose electro-oxidation on different bare metal electrodes.

and co-workers suggests the indirect electron transfer process is more likely to happen.^[202,209] However, further investigation to confirm this hypothesis is required to gain more insights, presumably via in operando X-ray adsorption spectroscopy/X-ray diffraction experiments and/or DFT simulations.^[210]

Co and Cu oxide catalysts have also shown promising activities toward glycerol electro-oxidation.^[211–214] A series of MCo₂O₄ (M = Mn, Fe, Co, Ni, Cu, and Zn) were investigated in a recent study, with CuCo₂O₄ being reported to have the highest intrinsic glycerol oxidation activity with an onset potential at 1.1 V_{RHE}.^[135] The overpotential at 300 mA F⁻¹ shows a pyramid-shaped trend over the atomic numbers, as shown in Figure 14B. At constant potential at 1.3 V_{RHE}, the CuCo₂O₄ achieved the highest selectivity (80.6%) for the production of formate with an overall Faradaic efficiency of 89.1%. Similar high selectivity has also been reported with a Ni–Mo–N nanoplate catalyst.^[203] At 1.36 V cell voltage, 10 mA cm⁻² current density was achieved, with high Faraday efficiencies for H₂ (99.7%) and formate (95%) generation. High selectivity toward formate comes from a sequence of converging oxidation and C–C cleavage steps all leading to the C₁ molecule (Figure 14C).

4.3. Selective Electro-Oxidation of Glucose

Glucose, a main compound in the food industry and in blood, is used as an energy source in most living organisms.^[215] This monosaccharide can be naturally formed from H₂O and CO₂ via photosynthesis of algae and plants, and constitutes a major biomass waste in pulp and paper processing industry. Through

different strategies, it can be transformed into various oxidation products such as gluconic acid, glucaric acid, and formic acid (Figure 15).^[216]

Moggia et al. studied the electrochemical oxidation of glucose under alkaline conditions, and compared three bare metallic electrodes (Cu, Pt, and Au).^[217] Au was found to be the most selective metal, with up to 86.6% selectivity to gluconic acid at 0.55 V_{RHE}, whereas Pt could only reach 78.4% selectivity at 1.10 V_{RHE}. By contrast, Cu easily cleaved C–C bonds, resulting in a mixture of glucaric, gluconic, and formic acid.

Base metal catalysts have been reported for glucose electro-oxidation as well. Zheng et al. reported an alkaline–acid asymmetric electrolytic cell that allows concomitant HER and glucose oxidation reaction.^[218] For this, they made a bifunctional electrode with Fe-doped CoSe₂ nanowires supported on conductive carbon cloth (Fe_{0.1}–CoSe₂/CC), which showed highly attractive electrocatalytic activity and stability in alkali for glucose oxidation and HER in acid (90 μmol H₂.h⁻¹), respectively. The performance of various catalysts for GOR have been summarized in Table 2.

Perhaps one of the most notable examples is Liu et al.'s mixture of NiFeO_x and NiFeN_x catalysts (Figure 16).^[150] NiFeO_x proved to be highly active for glucose oxidation in alkaline conditions, with a Faradaic efficiency of 87% and glucaric acid yield of 83%. Their mechanistic studies showed that FeOOH and NiOOH are crucial intermediates in the reaction, and the catalyst reached a TOF value of 0.16 s⁻¹. For HER, NiFeN_x had an excellent overpotential of 40.6 and 104 mV (at 10 and 100 mA cm⁻², respectively), close to those of 20% Pt/C catalyst. Thus, the authors constructed a glucose electrolyzer with NiFeO_x as the

Table 2. Summary of glucose electrolysis with different catalysts, the reaction conditions, glucose conversion rate, C balance (%), and product selectivity (%).

Ref.	Catalyst	Electrolyte	Temperature °C	Voltage [V]	Time [h]	Conversion rate %	C balance %	Selectivity %
[219]	Pd ₃ Au ₇ /C	0.1 M G/0.1 M NaOH	20	0.4	6	69.2 (glucose)	88.7	83.8 (gluconic)
[218]	Fe _{0.1} -CoSe ₂ /CC	0.5 G/1.0 M KOH	20	0.72	–	–	–	–
		0.5 G/1.0 M H ₂ SO ₄				90 μmol H ₂ ·h ⁻¹	–	–
[217]	Cu	0.04 M G/0.1 M NaOH	5	1.10	65	–	–	44.5 (gluconic)
	Pt							78.4 (gluconic)
	Au			0.55				86.6 (gluconic)
[50]	NiFeO _x	0.1 G/1.0 M KOH	20	1.30	18	90.6	85.3	71.2 (glucaric acid)

anode and NiFeN_x as the cathode. Via chronoamperometry, they showed that the electrolyzer delivered a current density of 101.2 mA cm⁻² at a voltage of 1.4 V and was stable over 24 h electrolysis.

4.4. Selective Electro-Oxidation of HMF

HMF obtained from dehydration of fructose (an isomer of glucose), is a furanic compound readily available from biomass. HMF has less selectivity issues for electro-oxidation than other substrates, as all the intermediates converge toward 2,5-difurandicarboxylic acid (FDCA, **Figure 17**). It either gets its hydroxyl group oxidized first, resulting in diformylfuran or gets its carbonyl function oxidized, resulting in 5-hydroxymethyl-2-furoic acid. Both are further transformed into 5-formyl-2-furancarboxylic acid, the last intermediate before FDCA formation. It has seen great application in replacing terephthalic acid in polyethylene terephthalate plastics,^[220] hence most papers focusing on FDCA formation.

Non-electrochemical routes to make FDCA from HMF require oxidants such as O₂, tBuOOH, H₂O₂ or (2,2,6,6-Tetramethylpiperidin-1-yl)oxyl (TEMPO), that are potentially harmful

on large scale and overall decrease the atom economy of the process.^[229]

An early example of HMF electro-oxidation was reported in 1991 by Grabowski et al., using NiOOH.^[230] They obtained 71% product yield after 4 h at 0.6 V_{SHE}. Between this report and the early 2010s, there has been very few developments. Interestingly, most electrocatalysts contain base metals (such as Ni, Co). Only a few reports involve noble metals, such as Chadderdon et al.'s,^[231] who prepared and compared various Pd_xAu_{3-x}/C catalysts (x = 0–3) for HMF electro-oxidation. At full conversion of HMF after 1 h at 0.9 V_{RHE}, the most efficient catalyst was Pd₁Au₂/C with 83% selectivity to FDCA. Interestingly, Pd/C only gave 29% selectivity whereas Au/C led to 98% selectivity to 5-hydroxymethyl-2-furoic acid meaning Au is only able to oxidize C=O bonds at low potentials.

HMF stability decreases substantially as pH increases due to its polymerization into insoluble humins.^[232] Choi and co-workers showed that 0.5 M HMF degraded by more than 70% at pH 14 (using 1.0 M KOH, unstirred) after 8 h. At pH 13 under the same conditions, the solution only degraded by 15%.^[223] This also explains why substrate concentration is substantially lower than for other hydrogen donors (10 × 10⁻³ M typically, as opposed to 1.0 M). However, most HMF electro-oxidation

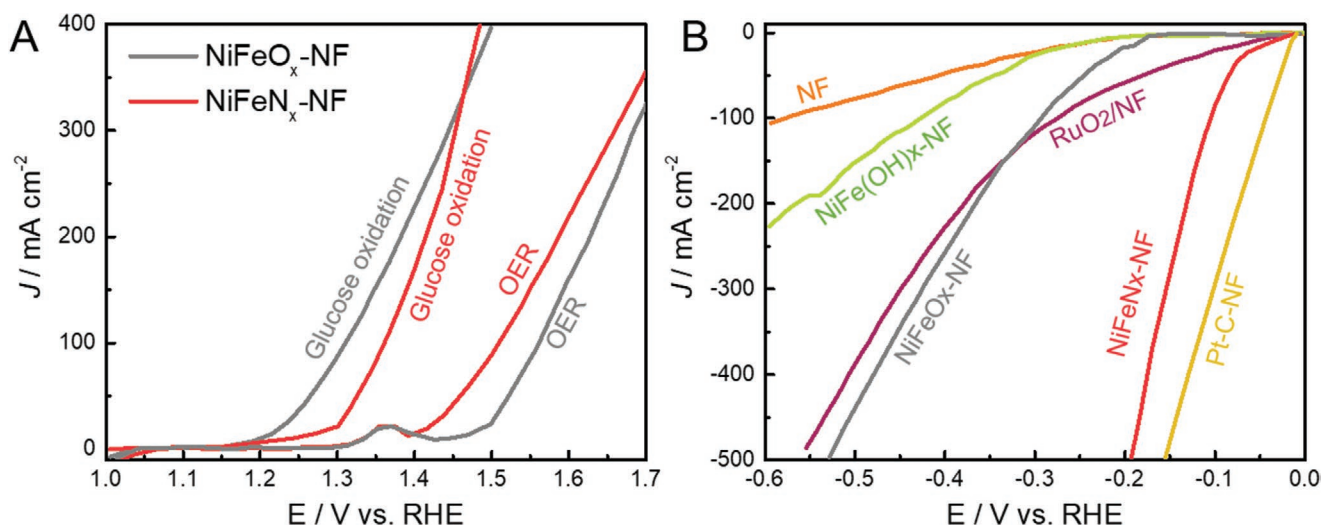


Figure 16. A) LSV profiles of the NiFeO_x-NF and NiFeN_x-NF catalysts for glucose oxidation and OER (scan rate of 5 mV s⁻¹; electrolyte: 1 M KOH; glucose concentration 100 × 10⁻³ M). B) LSV profiles of the different electrodes for HER in 1 M KOH electrolyte (scan rate of 5 mV s⁻¹). Reproduced with permission. ^[50] Copyright 2020, Nature Research.

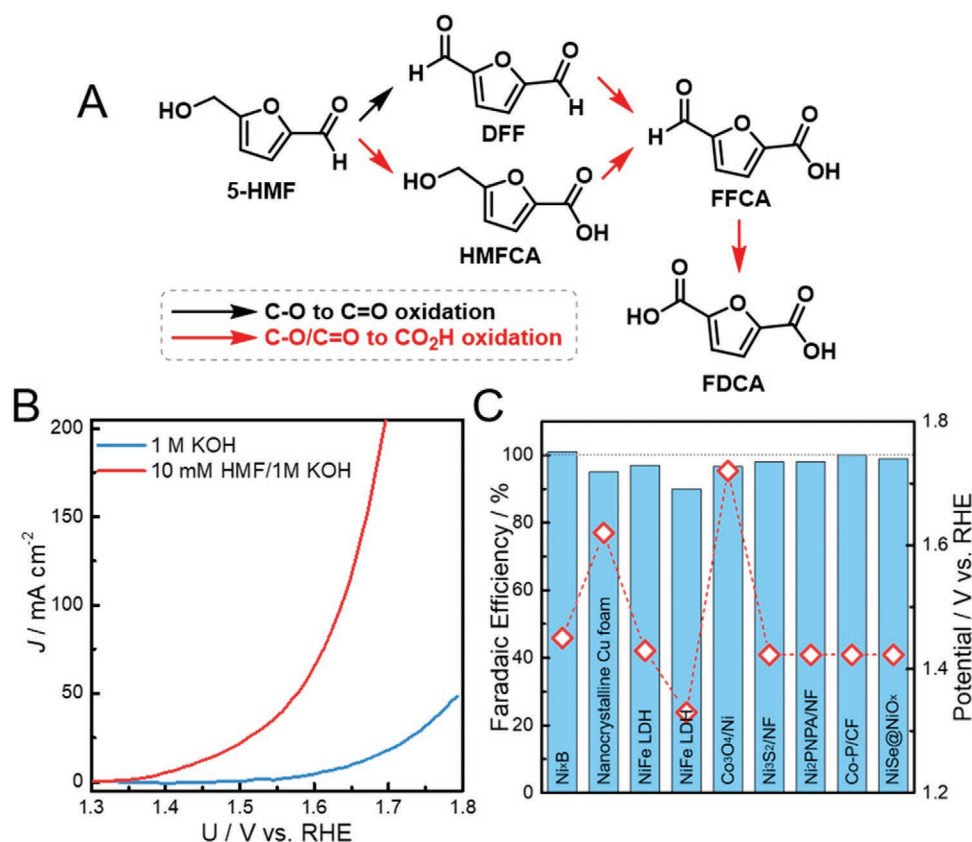


Figure 17. A) 5-HMF oxidation pathway. DFF: 2,5-diformylfuran, HMFCFA: 5-hydroxymethyl-2-furancarboxylic acid, FFCA: 5-formyl-2-furancarboxylic acid. B) Polarization curve of a Ni₂P NPA/NF catalyst in 1 M KOH with and without 10×10^{-3} M HMF. Reproduced with permission.^[221] Copyright 2016, Wiley-VCH GmbH & Co. KGaA, Weinheim. C) A comparison of different HMF oxidation catalysts in 1 M KOH and various concentration of HMF: Faradaic efficiency for FDCA production at given voltage (right panel). Data sourced from Ni_xB,^[222] nanocrystalline Cu foam,^[223] NiFe LDH,^[224] Co₃O₄/Ni,^[225] Ni₃S₂/NF,^[226] Ni₂P NPA/NF,^[221] Co-P/NF,^[227] NiSe@NiO_x.^[228] Detailed experimental conditions are summarized in Table S13 of the Supporting Information.

examples are run under very basic conditions (pH 13–14), to both preserve the metallic catalyst and assist the dehydrogenation steps. This is problematic for FDCA purification though, as it only precipitates at pH < 1, generating sizeable amounts of waste from the acidification of the solution at the end of the reaction.

Kubota and Choi reported the utilization of MnO_x as anode which allowed the reaction to occur at pH 1, 60 °C.^[233] Under acidic conditions, humin formation was prevented (<12%). Upon cooling down the reaction, FDCA precipitates, making it easy to retrieve without using stoichiometric amounts of acid. The MnO_x anode could oxidize both the alcohol and the aldehyde groups of HMF to form FDCA, whereas Pt could only oxidize the alcohol groups to form diformylfuran. Due to acidic conditions, FDCA further degraded to maleic acid (22%), a precursor to succinic acid.

There have been quite a few reports on making electrolyzers that can both oxidize HMF into FDCA and generate H₂ from H₂O. Indeed, they require a voltage up to 200 mV smaller than the ones based on pure water-splitting, while generating a valuable chemical. The Sun group prepared 3D Ni₂P nanoparticle arrays on nickel foam (Ni₂P NPA/NF), and tested it for such applications.^[221] Remarkably, the required voltages to reach 10 and 50 mA cm⁻² were reduced from 1.65 and 1.80 V for water

splitting to 1.44 and 1.58 V in presence of 10×10^{-3} M HMF, as shown in Figure 17B, with a production of H₂ of 120 μmol h⁻¹ and a selectivity to FDCA at >99%. Similar results were obtained by the same group with Ni₂S₃/NF^[226] and by Gao et al. with NiSe@NiO_x.^[228]

Co gave overall higher H₂ production than Ni (>250 μmol h⁻¹ compared to <150 μmol h⁻¹). Zhou et al. used cobalt oxide nanoparticles supported on nickel foam (Co₃O₄/Ni), reaching 270 μmol h⁻¹ of H₂.^[225] Finally, the Sun group explored a cobalt phosphide catalyst (Co-P), that gave similar voltages for 10 and 50 mA cm⁻² (1.40 and 1.55 V, respectively) but this time with a significantly higher H₂ generation rate of 500 μmol h⁻¹.^[227] However, selectivity to FDCA fell to 80% compared to 95% for the other metals.

The next covered examples focus on FDCA production rather than H₂ generation, again mostly with base metals.^[228,234] For instance, oxidized Cu surfaces are not catalytic for OER, thus avoiding competition for HMF oxidation as shown by Choi and co-workers using nanocrystalline Cu electrodes.^[223] They managed to attain Faradaic efficiency and FDCA selectivity above 95% over five consecutive uses. Interestingly, the catalyst was made by electrodeposition of Cu²⁺ salts over a Cu foil, resulting in a dendritic structure with high surface area. Upon sweeping the potential from the open circuit potential to 1.97 V_{RHE} at pH

13, the surface gets passivated from Cu^0 to a mixture of oxides that are responsible for the catalytic performance.

The same group has also compared three different MOOH electrodes ($M = \text{Ni}, \text{Fe}, \text{Co}$) for FDCA production.^[134] NiOOH was clearly the most active electrode, reaching 96% FDCA yield after 4.7 h at 1.47 V_{RHE} while both other catalysts only reached <35% yield at higher voltages 1.56–1.71 V_{RHE} . Although CoOOH can initiate HMF oxidation at a lower potential than NiOOH due to the $\text{Co}(\text{OH})_2/\text{CoOOH}$ conversion occurring at a less positive potential, the rate of $\text{Co}(\text{OH})_2/\text{CoOOH}$ -mediated HMF oxidation was too slow to generate sufficient current density for constant potential HMF oxidation.

Liu et al. prepared NiFe layered double hydroxide (Ni Fe LDH) nanosheets grown on carbon fiber paper.^[224] HMF was oxidized at a potential of 1.23 V_{RHE} in a yield of 98% with a Faradaic efficiency of 99.4% over 7 h. Notably, the catalyst was used at higher concentrations of substrate (up to $100 \times 10^{-3} \text{ M}$ against $5 \times 10^{-3} \text{ M}$).

However, a report by the Schuhmann group showed that NiFe LDHs lack stability during prolonged exposure to highly alkaline electrolyte solutions.^[235] Thus they explored nickel boride supported on nickel foam ($\text{Ni}_x\text{B}/\text{NF}$) for HMF oxidation.^[236] The resulting catalyst was highly active and stable over time, and the authors showed its suitability for HMF oxidation in a flow-through reactor, with an FDCA yield of 98.5% and a Faradaic efficiency of 100%.

The Faradaic efficiency to FDCA in alkaline condition by Ni and Co-based catalysts are included in Figure 17C. In general, at the voltage lower than water electrolysis, these earth abundant element electrodes showed high current density and high Faradaic selectivity toward FDCA, which is promising for future applications.

5. Electrochemical Reforming

Small-chain alcohols and urea, produced as target or byproducts in biomass valorization reactions, are potential substrates for electrochemical reforming reactions due to their relatively high hydrogen content.^[86] This factor distinguishes this process from the selective partial oxidation reviewed above, as it is dedicated toward H_2 production, so a complete oxidation process toward H_2 and CO_2 with maximum electron transfer numbers is desired.^[237] Thus, research on electro-reforming has primarily focused up to now on the reaction activity toward, C–H/C–C bond scission, rather than carefully tuning the reaction parameters and catalyst composition for better product selectivity. This section of the review focuses on the reaction mechanisms of electro-reforming of these organic molecules while summarizing the requirements for electrocatalysts development.

5.1. Methanol

Olah proposed in the early 2000s using methanol as a fossil fuel substitute, for energy storage and for transportation and synthetic hydrocarbon precursor.^[238] Although it is currently mostly produced from fossil-fuel-based syngas, methanol could be bio-sourced, i.e., via anaerobic digestion.

Methanol electrolysis has shown promising performance in many research works. In 2006, Shen and co-workers mixed tungsten carbide with 50 wt% Pt/C (Pt-WC/C) and used as the cathode which showed promising results, achieving 200 mA cm^{-2} current density at <0.47 V cell voltage for temperatures above 30 °C (Figure 18A).^[239] Take et al. reported methanol electrolysis in a membrane electrode assembly configuration. They have found that a moderate methanol is beneficial to reach higher current density without significantly increasing the cell voltage (Figure 18B). At constant methanol concentration, while the faraday efficiency of H_2 production is close to 100%, the CO_2 production remains very low (Figure 18C), which indicates the presence of methanol partial oxidation process. The electricity needed in their methanol electrolysis was 60% of that required for water electrolysis (Figure 18D).^[240]

The reaction mechanism and catalyst requirements of methanol oxidation have been discussed in detail in Section 4.1, in which noble metal based bimetallic catalysts, especially PtRu have shown superior catalytic activity owing to the fast CO removal via bifunctional mechanism.^[72] Apart from PtRu, other efficient electrode materials have also been developed to withstand CO poisoning effect. Au electrodes exhibit a promoting effect of CO for C–H bond breaking, which could act as an effective promoter for methanol electro-oxidation.^[115] Shape-controlled $\beta\text{-PdH}_{0.43}$ polycrystals and tetrahedra have also showed high methanol oxidation specific activity with weaker CO adsorption compared to Pd, possibly due to the larger lattice parameters which altered the valence band structure via strain effect.^[241] N-doped mesoporous carbon and 3D vertically aligned carbon nanofiber-supported Pt electrocatalyst also showed higher CO tolerance. Indeed, the formation of –OH groups on carbon support helps stripping off CO-like species on the adjacent Pt atoms.^[242,243]

For earth-abundant metal catalysts, a $\text{CuO}/\text{Co}(\text{OH})_2$ nanosheet composite showed high activity and excellent stability for methanol oxidation. With optimized Cu/Co ratio, at 1.65 V_{RHE} , the electrode could deliver high mass activity of 764 A g^{-1} , high area-specific activity of 159 mA cm^{-2} , as well as good TOF value of 2.55 s^{-2} . The improved performance was attributed to the Cu incorporation into $\text{Co}(\text{OH})_2$, which results in the enhanced Co oxidation state and the formation of $[\text{Co}(\text{OH})_2]^+$ species that favors the methanol adsorption and oxidation/dehydrogenation.^[244] Similarly, a cobalt hydroxide@hydroxysulfide nanosheets catalyst grown on carbon paper ($\text{Co}(\text{OH})_2/\text{HOS}/\text{CP}$) could also boost the electrocatalytic performance for methanol oxidation. The overpotential at the anode and cathode resulted 155 and 148 mV at 10 mA cm^{-2} , respectively, which enabled a two-electrode electrolyzer driven at a cell voltage of 1.497 V.^[245] The authors reported 100% Faradaic efficiency (sometimes even higher than 100%) for H_2 and formate formation, which raises the question whether some formate generated is from the carbon paper corrosion or other carbon sources. Isotope labeling experiments are thus needed for better clarification.

5.2. Ethanol

Compared to methanol, the C–C bond makes complete ethanol oxidation into CO_2 more difficult to achieve. To achieve high

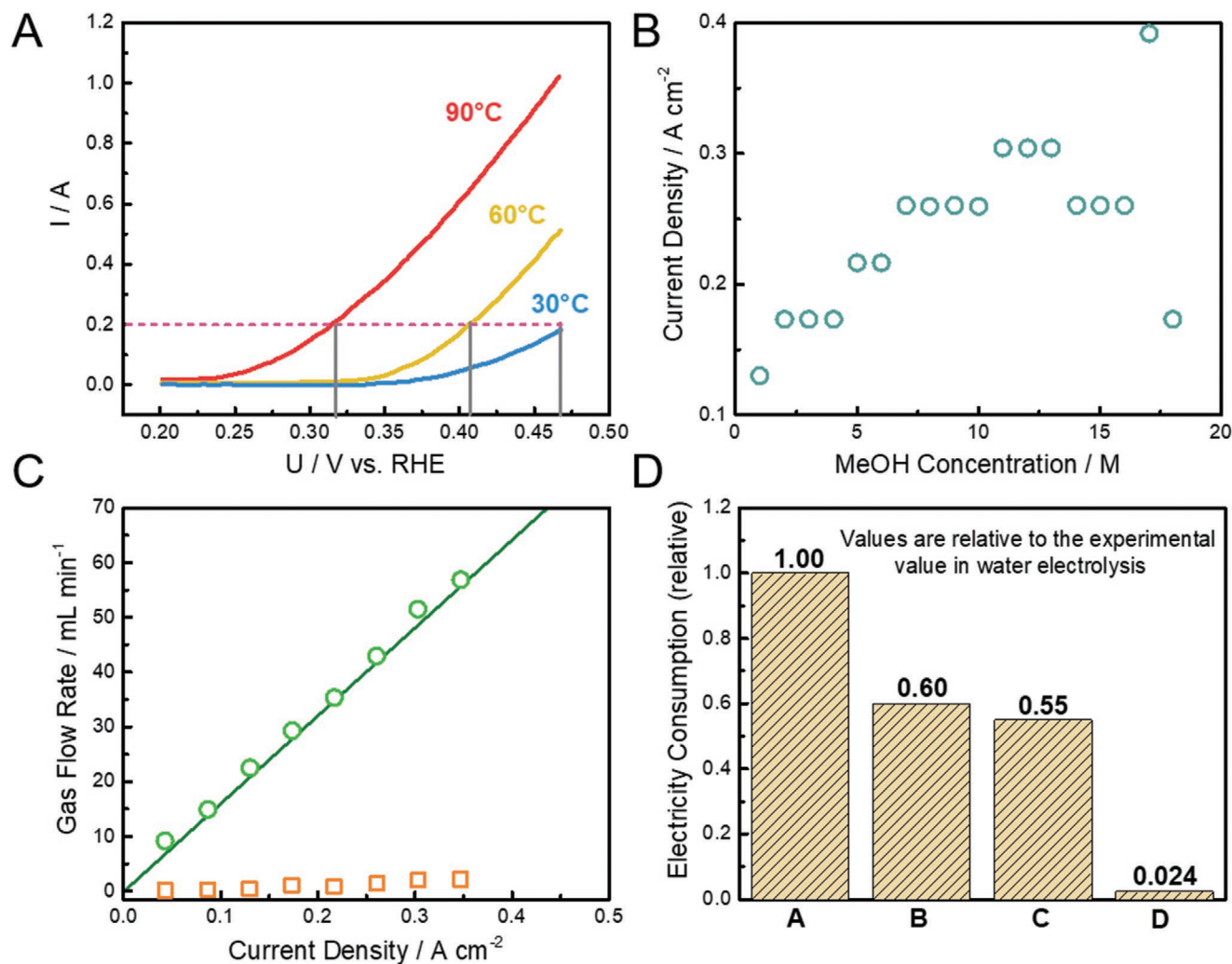


Figure 18. The influence of different parameters in methanol electrolysis. A) Effect of temperature on the performance of the electrolyzer in 2 m methanol + 0.5 m H₂SO₄ electrolyte. Reproduced with permission.^[239] Copyright 2007, Elsevier. B) Dependence of current density at which voltage rapidly increased with methanol concentration. C) Dependence of flow rate of each component in the cathode exhaust gas in the electrolysis cell on current density. The solid line means the theoretical hydrogen-production rate. Methanol concentration: 17 m. D) Comparison of electrical energy needed to produce hydrogen in methanol electrolysis and water electrolysis. Values are (A) experimental value in water electrolysis, (B) experimental value in methanol electrolysis, (C) theoretical value in water electrolysis, and (D) theoretical value in methanol electrolysis. Methanol concentration: 17 m. Current density: 0.35 A cm⁻². Reproduced with permission.^[240] Copyright 2007, Elsevier.

proton and electron transfer, the C–C cleavage must occur without poisoning the catalyst with C₁ intermediates. Thus, more energy is required and research in this field has focused primarily on precious metals such as Pt and Pd which are more active toward C–C bond cleavage as explained in Section 4.1. Early studies of ethanol oxidation reaction involved online differential electrochemical mass spectroscopy and in situ FTIR for analyzing the ethanol transformation mechanism on Pt and PtRh based electrodes.^[247–249] The ethanol dissociation and oxidation mechanism is summarized in Figure 19A, in which the C–C bond cleavage takes place due to the dissociative adsorption of both C atoms and are further oxidized into CO₂ at higher potential.^[80] This phenomenon was experimentally observed by Koper and co-workers with surface enhanced Raman spectroscopy, in which they found the peaks associated to C–H, Pt–CH, C–O, and Pt–CO vibration modes change

intensity while increasing potential.^[80] As shown in Figure 19B, the bands for C–H and Pt–CH appears at 0.1 V_{RHE} and showed a linear decrease to 0 when increasing the potential to 0.45 V_{RHE}. At the same time, the bands associated with adsorbed CO showed increasing intensities up to 0.45 V, followed by a decrease between 0.5–0.7 V_{RHE}. These results suggest that the adsorbed CH_x species will be converted to CO between 0.1–0.45 V_{RHE}, and the two CO* are further oxidized into CO₂ at higher potentials. Later, Braucherig et al. performed DFT calculation of different ethanol oxidation steps on Pt(111) surface at different potential to reveal the trends for different bond breaking.^[246] At 0.68 V_{RHE}, as shown in Figure 19C, they have found that the C–C bond activation become more exothermic after the initial dehydrogenation step. However, the authors also found out that, as the potential increases, the dehydrogenation reactions become linearly more exothermic, whereas the

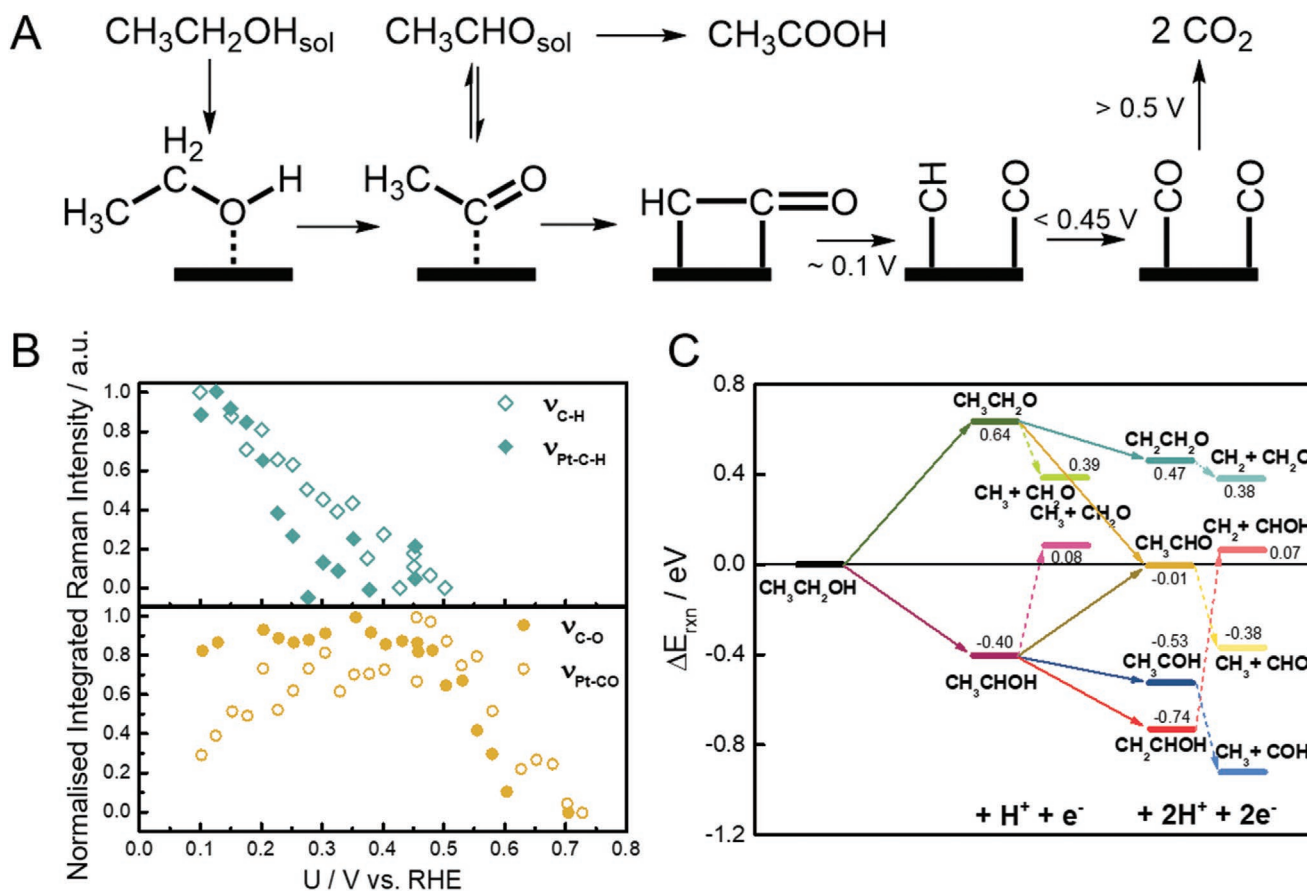


Figure 19. A) Schematic representation of the mechanism for the dissociation and oxidation of ethanol and acetaldehyde to carbon dioxide on a polycrystalline Pt electrode. B) Integrated Raman intensities from surface enhanced Raman spectroscopy for the bands associated with (top) the CH_x fragments and (bottom) the CO fragment resulting from the dissociation of ethanol as a function of potential. (A,B) Reproduced with permission.^[80] Copyright 2006, American Chemical Society. C) Reaction energies of elementary steps (referenced to adsorbed ethanol) for dehydrogenation and C–C cleavage reactions (dashed lines) for Pt(111) at $0.68\text{ V}_{\text{RHE}}$. Reproduced with permission.^[246] Copyright 2013, Elsevier.

C–C bond scission remain unaffected as they are not explicitly potential dependent. This explains the low complete oxidation efficiency in many Pt and Pd-based catalyst systems, as the dehydrogenation steps are much easier at higher potentials where CO can be oxidized into CO_2 .

Coutanceau and co-workers investigated ethanol oxidation in a PEM fuel cell with three Pt-based electrocatalysts (Pt/C, $\text{Pt}_{90}\text{Sn}_{10}/\text{C}$, and $\text{Pt}_{80}\text{Sn}_{20}\text{Ru}_4/\text{C}$). Amongst them, the ternary catalyst showed the highest current density over the whole potential range with the lowest onset potential, $0.2\text{ V}_{\text{RHE}}$ ($0.4\text{ V}_{\text{RHE}}$ for Pt/C), indicating its higher catalytic activity toward ethanol electro-oxidation. Sn greatly enhances C–C bond scission, resulting in more than double CO_2 yield. H_2 production, on the other hand, is independent to the ethanol concentration or the anode catalyst, and it is determined by the current density, proving that the process obeys the Faraday's law. The calculated power required based on the H_2 production rate is below $2.3\text{ kWh}(\text{Nm}^3)^{-1}$ (since $U_{\text{cell}} < 0.9\text{ V}$), at least two times lower than that for water electrolysis.^[22]

Incorporation of Rh and Sn into Pt nanostructures offers certain advantages over pure Pt such as promoting the C–C bond cleavage and minimizing the CO poisoning species due to the bifunctional mechanism.^[250,251] In terms of alloying with

transition metals, Bu et al. reported a hierarchical platinum–cobalt nanowire electrode (Pt_3Co NWs) with Pt-rich facets and ordered intermetallic structure, which showed great activity and durability for ethanol electro-oxidation due to the simultaneous downshift of the d-band center and surface strain of Pt surface atoms.^[252] In a recent work Duan and co-workers created single-nickel-atom-modified Pt nanowires offering an effective approach to optimize the activity of surface Pt atoms and enhance the mass activity by three times. DFT calculations and CO stripping experiments provided consistent results with weakened CO adsorption energy on single Ni atom-modified Pt top sites and decreased CO oxidation onset/peak potential, suggesting that the enhanced activity could be attributed to at least partly to the improved CO tolerance.^[253]

Pd based materials have also been intensively studied for ethanol electrolysis to understand its catalytic origin as well as the deactivation mechanism.^[254–259] Vizza and co-workers performed a net energy analysis of H_2 production by bio-ethanol electrochemical reforming, from which an energy saving of 26.5 kWh/kg H_2 could be achieved compared to PEM water electrolyzer stacks (45 kWh/kg H_2). The anode electrode consists of Pd nanoparticles deposited onto TiO_2 nanotube arrays, which provides a high electrochemical active surface area

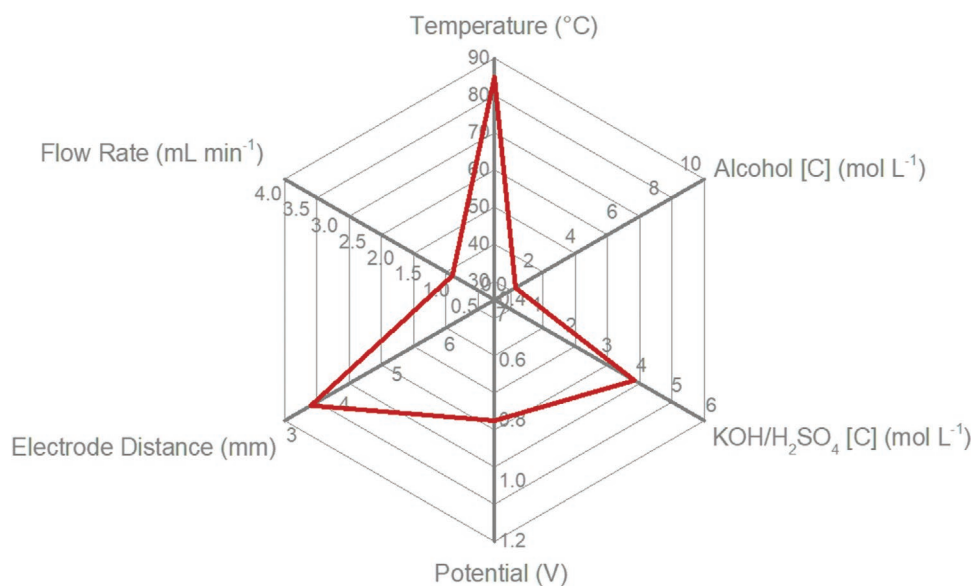


Figure 20. Summary of optimal reaction conditions for alcohol electrolysis. Data sourced from literature.^[263–266]

(45.9 m² g_{Pd}⁻¹) and superior alcohol oxidation activity. Other substrates (ethylene glycol, glycerol, and 1,2-propanediol) have also been tested under the same conditions, from which they showed that the cell voltage and energy consumption increases with the carbon chains.^[20] The same group reported a similar electrolysis system with Pd-(NiZn)/C on Ni foam anode with Pd loading 1 mg cm⁻², which displayed as well a large reduction power when adding different organic substrates (10 wt%) in 2 M KOH, with 42.6 kWh kg_{H₂}⁻¹ reduced from ethanol electrolysis.^[33] Bimetallic Pd-based electrocatalysts such as Pd-Co films and Au-Pd core-shell nanoparticles have also shown superior performance toward ethanol oxidation.^[34,260] In all the systems a higher reforming temperature is demonstrated to promote the C-C bond breaking and results in a higher H₂ production rate. Therefore, in a recent report the electrochemical reforming of ethanol was conducted at 150 °C in an autoclave cell which allows the safe pressurization of H₂. Alkaline conditions as well as a high temperature are very aggressive to PdCo-Ni_{foam} catalysts, for which the authors introduced an external layer of phosphates to prevent Pd dissolution and resulted in stable current density up to 10 h.^[261] Similar stabilizing strategy with P has also been reported with graphene-supported PdP₂ nanocrystals where P could modify the electronic structure of Pd and Pd-rich surface and improve the charge-transfer kinetics as well as the stability.^[262]

The electrochemical reforming reactions of diols and polyalcohols, such as ethylene glycol,^[267–269] 1,3-propanediol^[270] have also been reported over the last decade, which all have shown promising performances toward H₂ production with reduced electricity consumption. The reaction parameters for general alcohol electro-reforming are summarized in **Figure 20**. Their contributions to the H₂ production rate are also evaluated based on the above reports.

Present as the most and second abundant source of biomass, cellulose, and lignin are considered the most attractive proton and carbon source due to their availability and low-cost. Biomass electrolysis of these raw feedstocks, lignin,^[271–275]

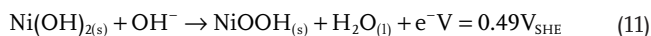
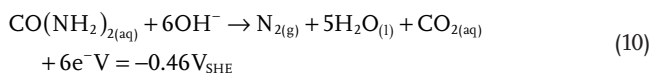
and cellulose^[276,277] has therefore also been studied. Similar to methanol and ethanol electrolysis, the primary focus on lignin and cellulose electrolysis is H₂ production with less electricity consumption. For instance, Deng and co-workers presented a novel electrolysis approach using cellulose, lignin, and even wood and grass powders.^[278] The calculated electricity consumption at 0.2 A cm⁻² was 0.69 kWh Nm⁻³ H₂, which is only 16.7% of that for water electrolysis. The oxidative products from lignin are typically benzylic molecules, such as vanillin, while the products from cellulose include gluconic acid, oxalic acid, and formic acid. Although the electrocatalytic routes for these raw materials transformation remain unclear, there are existing simulation models of these long chain molecules, which can shed light on the dissolution, regeneration, and catalytic conversion mechanism.^[279]

5.3. Urea

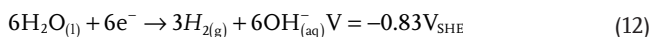
As a promising hydrogen storage material, urea is widely available, nonflammable, relatively nontoxic, easy to store and transport, and displays a volumetric energy density of 16.9 MJ L⁻¹, even higher than that of compressed liquid hydrogen.^[280] The large amount of urea generated from industrial, agricultural and human waste could cause contamination to the atmosphere and ground water, raising severe environmental issues.^[281] On that note, urea electrolysis in alkaline media is widely used to remediate urea-rich waste water to produce valuable hydrogen fuel, preventing toxic ammonia emissions and nitrate contamination.^[282] Ni is the optimal catalyst for urea oxidation reaction and is earth abundant and significantly (≈1500 times) cheaper than Pt.^[283] As a consequence, urea electrolysis holds great potential for efficient hydrogen production, which has attracted increasing attention over the last decade.

In 2009 Botte and co-workers first demonstrated the technology of urea electro-oxidation. They compared different electrocatalysts (Pt, Pt-Ir, Rh, and Ni) and found Ni is the most

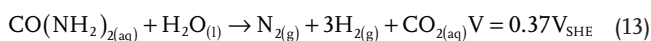
active catalyst in terms of current density.^[42] Owing to the redox-active characteristics of 3d transition metal elements, the corresponding hydroxides can be applied as electrocatalysts for energy conversions.^[237] The urea oxidation on Ni based anode catalysts consists of two competing reactions



H₂ is produced at the cathode via water reduction



The overall reaction can be expressed as:



with the desorption of *COO intermediate identified as the rate-determining step.^[286] The investigation of urea electro-oxidation mechanism and kinetics on Ni electrodes in alkaline medium have confirmed that urea oxidation occurs after the formation of surface Ni³⁺, which then reacts with the urea molecules and regenerate active sites for further adsorption and oxidation. The effect of scan rates and rotating disk electrode voltammetry, illustrated by the Koutecky–Levich plot, prove the presence of diffusion and kinetically controlled mechanisms, which are affected by urea concentration, pH as well as rotation speeds.^[287]

As showed above, urea oxidation is a six-electron transfer process with complicated gas evolution steps, suffering from intrinsically sluggish kinetics. Thus, high-performance Ni electrodes are required to reduce the reaction barriers. The design principles can be classified in three ways: increasing Ni valence state, engineering active sites, and constructing fast mass-transporting electrode structure.

For Ni valence state, it is commonly believed that increasing the intrinsic Ni³⁺ concentration or generating high-valence species could bring higher catalytic activity, owing to the more intensive interaction between the metal 3d and oxygen 2p band centers that enhance the electrochemical reaction kinetics.^[281,288] DFT calculations also suggested that urea molecules are more easily adsorbed onto the NiOOH species surface.^[286] Yu et al. developed efficient urea oxidation and HER electrodes by annealing solid NiMoO₄·xH₂O in Ar (NF/NiMoO-Ar) or H₂/Ar atmosphere (NF/NiMoO-H₂).^[289] Mo⁶⁺ promotes the transition of Ni²⁺ to Ni³⁺, resulting in excellent urea electrolysis activity and stability, with 10 mA cm⁻² current density at a cell voltage of 1.38 V for over 50 h operation. Beyond Ni³⁺, Peng and co-workers have revealed in a recent study that a lattice-oxygen-involved reaction pathway could largely boost urea electro-oxidation reaction by creating NiOO (Ni⁴⁺) active sites, which would facilitate the rate-determining *COO desorption step with lower free energy requirement than NiOOH, as displayed in **Figure 21A–C**, therefore leading to significantly faster reaction kinetics with four times higher TOF than conventional Ni³⁺.^[284]

Forming Ni based LDH and hybrid systems is an effective approach to engineer the active sites. LDH have been intensively studied to serve as an alternative to IrO_x OER catalysts in

alkaline conditions for water electrolysis.^[210] Recently they have also been proven to be active for urea oxidation.^[288,290] Details about the controllable synthesis and properties of LDH can be found in a recent review.^[237] The ratio between Ni and other transition metals (Fe, Co) is crucial for modulating the Ni active sites, while the degree of amorphous and crystalline phases also needs careful consideration in order to balance the active site generation and intrinsic conductivity.^[288] In the development of NiCo LDH, Zeng et al. demonstrated that the interlayer spacing in the LDH structure plays a pivotal role, with higher activity/selectivity under larger spacings.^[290]

Hybrid systems can have more active sites without sacrificing the electronic conductivity.^[291–294] For example, Li et al. designed CoS₂/MoS₂ Schottky heterojunctions to manipulate the surface charge distribution for synergistically boosting the adsorption and scission of chemical bonds of urea molecules.^[285] The resulted electrode showed superior activity toward urea electrolysis, with a cell voltage as low as 1.29 V to achieve a stable current (60 h) of 10 mA cm⁻². The mechanism was investigated by DFT calculations, which suggested that the self-driven charge separation across the heterojunction interface would form local electrophilic/nucleophilic regions. As illustrated in **Figure 21D**, those regions would then attract electron-donating/accepting groups in urea and activate the chemical bonds, leading to the urea decomposition. The performance of recent reported electrocatalysts for urea electrolysis is summarized in **Figure 22** and Table S14 (Supporting Information), among which the hybrid catalysts have shown high performance. On the anode side, many electrocatalysts reported have shown lower overpotential than RuO₂ catalysts, but still higher than IrO₂. On the cathode side, Pt/C is still the benchmark catalyst, but a carefully engineered NF-NiMo-H₂ has shown similar small overpotential as well as current density.

Since both urea oxidation and HER are gas–liquid–solid triphase processes, electrodes with enough effective space are indispensable for gas escape and reactant diffusion onto their surface. In this regard, constructing fast mass-transporting structure becomes one of the key factors, as demonstrated with in situ grown Ni₁₂P₅/Ni–Pi/NF core–shell structures,^[300] Ni–NiO–MoNi hybrid,^[294] 3D Ni(OH)₂/NF networks^[304] as well as Ti-mesh supported porous CoS₂ nanosheets.^[298] By modulating the Ni₂P/Ni_{0.96}S heterostructure, He et al. could combine the advantages of phosphides, which exhibit P-terminated structure for negative charge accumulation and present a hydrogenase-like catalytic behavior that is suitable for HER, with the highly stable sulphide to achieve a synergistic effect toward high catalytic activity and durability. The unique heterostructure could also provide lattice defects for more active sites and expedite gas releasing and electrolyte diffusion.^[293]

In summary, biomass electrolysis has lower thermodynamic requirements compared to water electrolysis, leading to low ΔE_{eq} and high H₂ production efficiency, however the kinetics are also sluggish due to the multiple electron transfer process. Electrocatalyst design need to take into consideration of the chemical structure of different biomass substrates. The coproduction of value-added chemicals and H₂ requires catalysts with high Faradaic efficiency toward desired products, while the reforming dictates high current density and low overpotential for improved H₂ production rate and reduced electricity consumption. In the next section, state-of-art research advances on

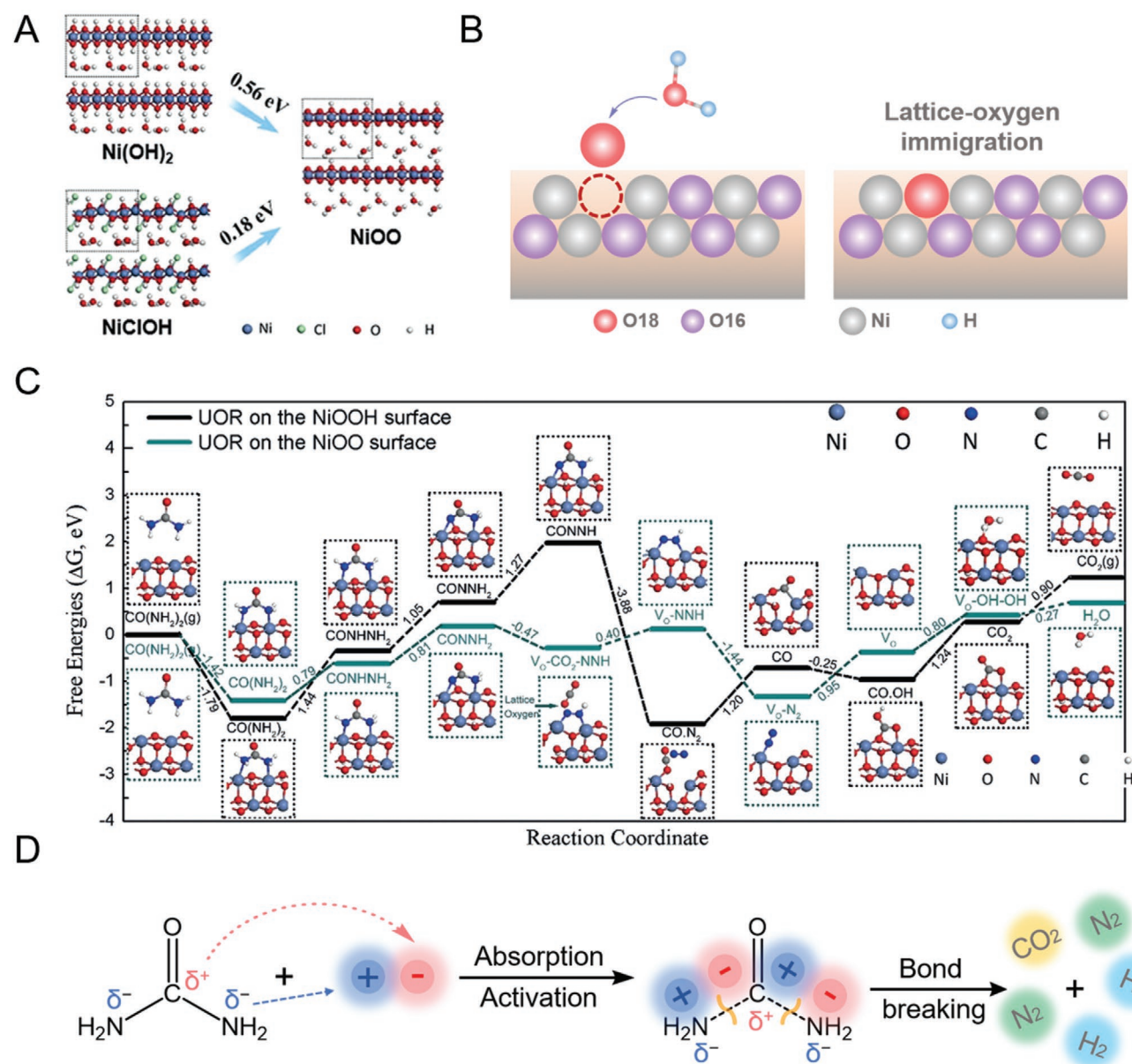


Figure 21. A) The formation energy from Ni(OH)₂ and NiClOH to NiOO models. NiClOH has a lower energy barrier to formation reactive NiOO sites than Ni(OH)₂. B) Illustration of lattice-oxygen involvement in NiClOH catalyst during urea oxidation. C) ΔG profiles calculated at the standard conditions and the simplified surface structures of the various reaction species along the reaction pathways of urea oxidation on NiOO and NiOOH surfaces. Reproduced with permission.^[284] Copyright 2019, Wiley-VCH GmbH & Co. KGaA, Weinheim. D) Catalytic mechanism diagram of urea oxidation on CoS₂-MoS₂ Schottky catalyst in alkaline solution. Reproduced with permission.^[285] Copyright 2018, Wiley-VCH GmbH & Co. KGaA, Weinheim.

photo(electro)catalytic hydrogen production from biomass feedstocks will be summarized, with the main focus on reviewing the reaction mechanism of different biomass molecules, as well as providing critical prospects on future benchmarking studies.

6. Hydrogen Production by Solar-Driven Organic Transformation

Producing hydrogen directly from water and sunlight via photocatalysis holds great promise for the scale-up of green

hydrogen. However, requirements on the semiconducting photocatalyst are numerous: not only does it have to absorb the maximum amount of the solar spectrum to generate photoexcited charge carriers via the photoelectric effect but it has also to efficiently transfer these electrons and holes to the semiconductor-electrolyte solution junction and drive the reduction and oxidation of water, respectively (Figure 23A).^[10] Since the first reports by Boddy or Fujishima and Honda utilizing a TiO₂-based photoelectrochemical cell,^[305,306] this concept was quickly extended to powder photocatalysis. Many semiconductor materials were reported with photocatalytic

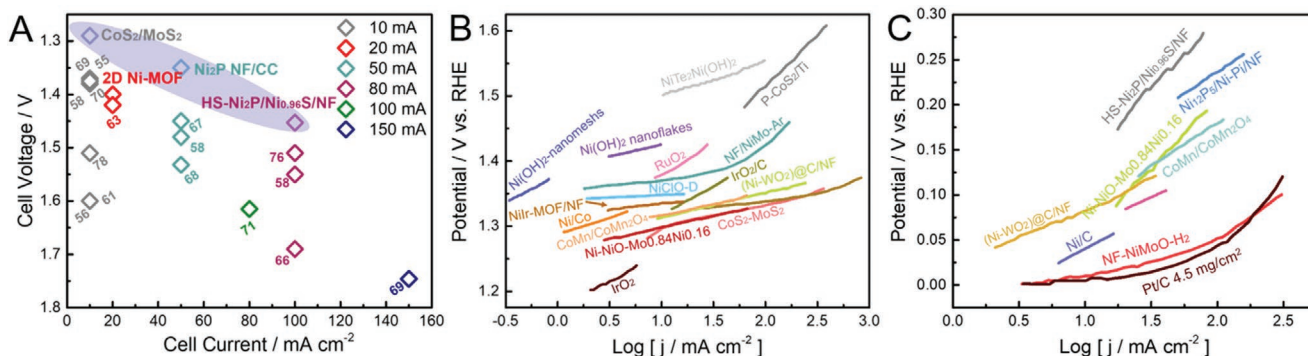


Figure 22. Summary of urea electrolysis performance reported in literature. A) Urea electrolysis cell voltage at different current density. B) Urea oxidation and C) HER polarisation curves at the Tafel region. Data sourced from: CoS₂/MoS₂,^[285] 2D Ni-MOF nanosheets,^[281] Ni₂P NF/CC,^[295] HS-Ni₂P/Ni_{0.96}S/NF,^[293] Ni(OH)₂-nanomesas,^[296] NiIr-MOF/NF,^[297] NiTe-Ni(OH)₂,^[292] P-CoS₂/Ti,^[298] Ni(OH)₂ nanoflakes,^[299] RuO₂,^[300] Ni/Co,^[301] NiClO-D,^[284] NF/NiMo-Ar,^[289] CoMn/CoMn₂O₄,^[291] (Ni-WO₂)/C/NF,^[302] Ni-NiO-Mo_{0.84}Ni_{0.16}, IrO₂,^[293] Ni₁₂P₅/Ni-Pi/NF,^[300] Ni/C,^[303] NF-NiMoO-H₂,^[289] Pt/C.^[289] Detailed information about experimental conditions are summarized in Table S14 of the Supporting Information.

activities, including metal oxides,^[307–310] chalcogenides,^[311] carbon nitrides,^[312–314] etc. Though numerous photocatalytic systems have been reported for overall water splitting, solar-

to-hydrogen (STH) efficiencies of powder photocatalytic and photoelectrochemical systems using earth abundant materials remain below ≈5%.^[315,316] To a large extent this is due to the

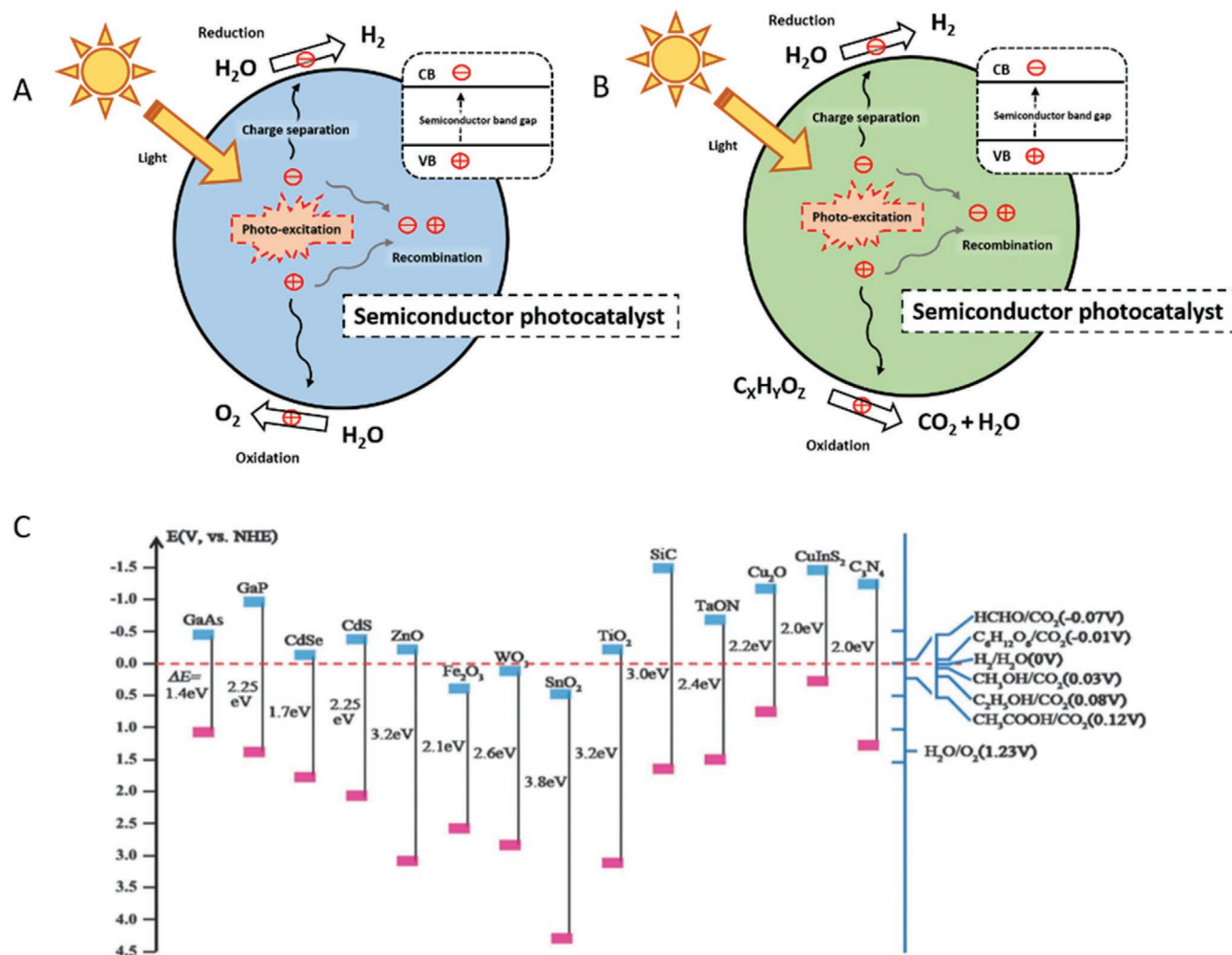


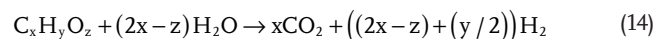
Figure 23. A) Processes in photocatalytic water splitting. B) Processes in photocatalytic hydrogen production with biomass oxidation. C) Energy band structure of different semiconductors suitable for the oxidation of organic molecules. Reproduced with permission.^[322] Copyright 2014, Royal Society of Chemistry.

energy demanding nature of OER.^[317] This energy has to be entirely sourced from the sun by the photocatalyst, which poses severe limitations to photocatalytic systems. UV-absorbers such as TiO₂, SrTiO₃, and others can provide the required photovoltage and have suitable band positions for favorable charge transfer during the catalytic steps but their STH efficiency is limited to ≈4% due to the relatively small amount of UV light in the solar spectrum.^[11] Consequently, Z-scheme photocatalyst approaches using two photocatalysts in tandem have been used. Such artificial photosynthesis systems bring more complexity and more challenges to build efficient overall water splitting devices/reactors. Similar to electrochemical processes, H₂ production derived from biomass sources has been shown to be a more favorable process thermodynamically,^[318–320] provided that the oxidation potential of standard biomass derivatives such as alcohols or sugars (Figure 23B) is considerably more negative than the water oxidation potential (Figure 23C).^[321] As such, the requirement for a deep valence band maximum is lifted (if overpotentials are low) and particulate systems with a single visible light absorber can be engineered broadening the choice of semiconductor photocatalysts.

6.1. Biomass-Derived Feedstocks as Hole Scavengers in Photocatalytic Hydrogen Production

Besides a light-harvesting semiconductor with suitable conduction band and valence band positions, a typical photocatalytic H₂ production setup typically includes other components with highly relevant roles. A cocatalyst is often added in order to accelerate the catalytic steps and simultaneously aid the spatial charge separation alleviating charge carrier recombination in the semiconductor.^[323] These cocatalysts are often nanoparticles, single atoms or molecular complexes of the platinum group metals with platinum being the most common catalyst for the HER owing to its optimal binding energy to H, leading to a remarkably low overpotential.^[324,325] Photocatalytic particulate systems often utilize hole scavengers which are easier to oxidize than water due to less demanding oxidation potentials and lower overpotentials due to simpler redox chemistry (typically fewer intermediates to stabilize). This faster oxidation chemistry removes holes from the semiconductor and hence improves the lifetime of the photogenerated electrons resulting in higher hydrogen yields. Hole scavengers are typically OH-containing small molecules such as methanol, ethanol, or glycerol, amongst others, which upon interaction with a hole or with hydroxyl radicals get oxidized to the corresponding aldehydes and which can further decompose to CO₂ if operated for prolonged times (which varies depending on reaction conditions and employed semiconductor).^[326] The main reaction pathway is their oxidation to an α-hydroxyl radical and further oxidation of the latter to the aldehyde, which often leads to the evolution of other hydrocarbons and mainly CO₂ upon complete decomposition.^[327] Nevertheless, little or no insights are often provided in the oxidation products of such molecules, and most of the published reports are focused on correlating reaction mixture composition with H₂ evolution performance, rather than on the oxidation intermediates. Kawai and Sakata reported initially in 1980 the direct photocatalytic production

of H₂ from methanol and water over TiO₂-based catalysts,^[328] which upon prolonged illumination, released H₂ and CO₂ from a H₂O/methanol 50:50 (v/v%) mixture. Matsumura et al. analyzed the effect of the solution pH in an aqueous methanol solution toward the production of H₂ on a Pt-CdS catalyst, showing H₂ and CO₂ being produced just at high pH owing to the higher stability of CdS to photocorrosion in alkaline environment. Furthermore, they observed that ethanol and 2-propanol followed the same trend but not tert-butyl alcohol, indicating that solely alcohols with a hydrogen atom in the α-position can lead to H₂ production.^[329] CdS materials were later further explored for the photocatalytic hydrogen production with isopropanol as hole scavenger owing to the more suitable bandgap compared to TiO₂ (2.4 eV for CdS vs 3.2 eV for TiO₂) which allows to perform photocatalysis under visible light irradiation (λ > 400 nm).^[330,331] Kondarides and co-workers studied hydrogen production rates with Pt-TiO₂ photocatalysts varying parameters such as type and concentration of hole scavenger (methanol and ethanol, 2-propanol, and butanol), the solution pH and temperature and found that H₂ evolution scaled linearly with the concentration of hole scavenger added and produced stoichiometric production of H₂ and CO₂ demonstrated for methanol and ethanol according to the formula^[332]



When comparing the trends with the different alcohols, the authors observed that, while methanol and ethanol lead to a higher initial performance owing to the size-dependent mobility of these compounds, their complete oxidation happens at an earlier stage than for 2-propanol and butanol due to the larger number of reaction intermediates. Glycerol was later shown to perform similarly, releasing stoichiometric amounts of H₂ and CO₂ (C₃H₈O₃ + 3H₂O → 3CO₂ + 7H₂), increasing the production with higher concentrations.^[333] We want to note here that the performance stability of the photocatalytic TiO₂-Pt system strongly varied under UV or visible light illumination typically showing a 50% drop in catalytic activity after ≈200 min under UV and ≈1000 min under visible light excitation. The enhanced stability under visible light illumination likely results from the about 3–7 times lower H₂ evolution rate (i.e., for ethanol oxidation with comparable concentrations) and shows that catalyst activity and stability are strongly coupled. Single atom catalysts of Pt might break this relation through a more stabilized catalytic center with high intrinsic activity.

Insights in the direct photocatalytic production of hydrogen from glycerol under visible light over a Pt-CdS catalyst were provided by de Oliveira Melo et al. using an aqueous solution of glycerol (30%) with pH = 11 as reaction medium.^[334] In this study, the authors compared the performance of CdS, TiO₂, and a combination of both as a photocatalyst, observing that, while CdS displays a more negative, and therefore more favorable, conduction band for hydrogen evolution (−0.75 V_{NHE} in pH 10 for CdS compared to −0.43 V_{NHE} for TiO₂), the photogenerated holes are not energetic enough to oxidize glycerol. Therefore, the production of hydrogen was suggested to occur through two different pathways: one approach entails the partial decomposition of glycerol to CO which poisons the Pt cocatalyst and is released after interaction with reactive oxygen species generated

by photogenerated holes as proposed by Bowker et al.^[335] The other was the direct oxidation of glycerol by holes through the primary carbon or secondary carbon, forming different oxidation intermediates depending on the activated carbon. After 7 h irradiation time, intermediates such as formaldehyde or acetaldehyde were further oxidized to CO₂.

Owing to the wide variety of available biomass-derived hole scavengers, and the parameters affecting the photocatalytic performance, plenty of studies have been dedicated to elucidating the ideal conditions for achieving a more efficient hydrogen production. Often, experimental studies focus on only one variable to optimize the photocatalytic system, however, more innovative approaches are needed that would allow for faster process optimization. Along this line of thought, Iliuta and co-workers designed a set of experiments coupling response surface methodology with an artificial neural network approach to predict the response of hydrogen production to several varying parameters such as Pt loading (0.02–5 wt% on TiO₂), catalyst loading (0.05–5 g L⁻¹), glycerol concentration (0.5–50% v/v) and pH (pH 2–12).^[336] They obtained an optimum for a 50 vol% glycerol mix, a Pt loading of 3.1%, and a catalyst loading of 3.9 g L⁻¹ in pH 4.5 in good agreement with previous works by Kondarides and co-workers.^[333] Considerations in their optimization were the light harvesting ability, particle aggregation, interparticle electron–hole recombination, and density of catalytic sites. The pH of the solution determines the adsorption of glycerol on the catalyst surface,^[337] while highly acidic pH causes the agglomeration of TiO₂ particles. Highly alkaline conditions result in the excessive modification of the catalyst ligand with –OH groups (TiOH) and consequently at a pH of net zero charge (6.25 for TiO₂) glycerol will be adsorbed more readily through hydrogen bonding with hydroxyl groups. Their data confirmed that glycerol concentration is the less relevant parameter (9%), barely influencing the reaction rate, while catalyst concentration was the dominant one (36%).^[338] Differences in the hole scavenging properties between methanol, ethanol, and glycerol were studied by Waterhouse and co-workers using different alcohol–water mixtures with varying concentrations in the presence of Ni/TiO₂ or Au/TiO₂ photocatalysts under UV irradiation. While at low concentrations (10–15% v/v), glycerol yielded a higher H₂ production rate (up to 42.9% quantum efficiency for Au/TiO₂), at higher concentrations (to 40% and 80% v/v) methanol and ethanol afforded the highest rates (respectively).^[327] The results were attributed to the viscosity of the alcohol water solutions; a neat glycerol solution displays a viscosity of 612 cP, while those of methanol and ethanol stand at 0.659 and 1.280 cP, respectively. This fact strongly determines the transport of reactants and the mobility of the particle semiconductors in the reaction media. The reason for the higher concentration of ethanol versus methanol required was found to be the formation of reaction intermediates such as acetaldehyde rather than its total conversion to CO₂ and H₂. The oxidation potential of the used alcohol was proven to be relevant at low concentrations (10%), where glycerol resulted in a higher yield owing to the slightly lower oxidation potential versus methanol and ethanol (0.004, 0.016, and 0.084 V_{NHE}, respectively).^[339] By contrast, Wei et al. using TiO₂ photocatalysts with a 3% loading of a NiS_x cocatalyst in a 20% aqueous solution of scavenger observed that methanol displayed a much higher hydrogen production rate compared

to glycerol or ethanol. While this result was mainly attributed to an enhanced hole capture efficiency (assessed by the amount of photoluminescence (PL) quenched), PL decay kinetics were found to be identical in the presence of any of these scavengers studied (on nanosecond timescale).^[340] This indicates that these PL measurements do not track the kinetics of the scavenging reaction but rather an indirect process likely related to a change in the amount of hole trapping in anatase TiO₂ as suggested for this PL range.^[341]

Besides the above mentioned alcohols, more complex biomass-derived molecules, or even raw biomass, have been shown to perform as hole scavengers.^[343] Kasap et al. demonstrated the photoreforming of several models of lignocellulose (including 4-methylbenzyl alcohol, α -cellulose, xylan, lignin, and their derivatives) in a wide range of pH utilizing cyanamide-functionalized carbon nitride nanosheets with different cocatalysts. They could observe up to 39 310 $\mu\text{mol H}_2 \text{ g}^{-1} \text{ h}^{-1}$ and a 22% average quantum efficiency for the reforming of 4-methylbenzyl alcohol to 4-methylbenzaldehyde in the presence of a molecular Ni cocatalyst.^[344] While the presence of the Ni complex resulted in a higher initial conversion rate, it degraded after 24 h, therefore Pt and MoS₂ showed a higher stability. Reisner and co-workers utilized carbon dots prepared from the thermal treatment of cellulose along with a molecular nickel cocatalyst as a photocatalyst for biomass photoreforming. They reached a benchmark activity of 13 450 $\mu\text{mol H}_2 \text{ g}^{-1} \text{ h}^{-1}$ and average quantum efficiency of 11.4% under 360 nm irradiation when using ethylenediaminetetraacetic acid as an electron donor, showing as well photocatalytic activities when replacing it with a wide variety of soluble and insoluble biomass model substrates and alcohols.^[345] Furthermore, transient absorption spectroscopy confirmed the electron transfer to the Ni-complex and the hole transfer to the biomass residues.

A dispersion of CdS quantum dots in alkaline solution was employed by Wakerley et al. for the photoreforming of cellulose, hemicellulose, and lignin to H₂ (**Figure 24**). The high alkaline conditions promote the formation of Cd(OH)₂/CdO on the surface which stabilizes the catalysts against photocorrosion and additionally facilitates the solubility of lignocellulose. The photocatalytic tests with α -cellulose as substrate resulted in an average quantum efficiency of 1.2%, at $\lambda = 430 \text{ nm}$ and the oxidation of the polysaccharide groups to carboxylic acids as confirmed by ¹³C-NMR.^[342] Utilizing this system, lignocellulose, including wood or paper could be reformed under light.^[346]

Up to now, the focus in this research has been to target ideal parameters for achieving high H₂ yields, and plenty of works have been published showing the hydrogen production from biomass-derived alcohols utilized as hole scavengers with different semiconductors,^[347,348] cocatalysts,^[349,350] and biomass-derived molecules.^[351] Nevertheless, the number reports that have focused on the thorough analysis of the oxidation pathway and products are rather low. While certain correlations and general rules can be obtained from the published literature, such as the importance of an α -H to the OH group, the bandgap of the semiconductor, or the oxidation potential of the desired alcohol, there are still plenty of disagreements and open questions that remain to be solved such as the ideal reaction pH or scavenger concentration amongst others. Owing to the wide availability of photocatalysts and cocatalysts with different

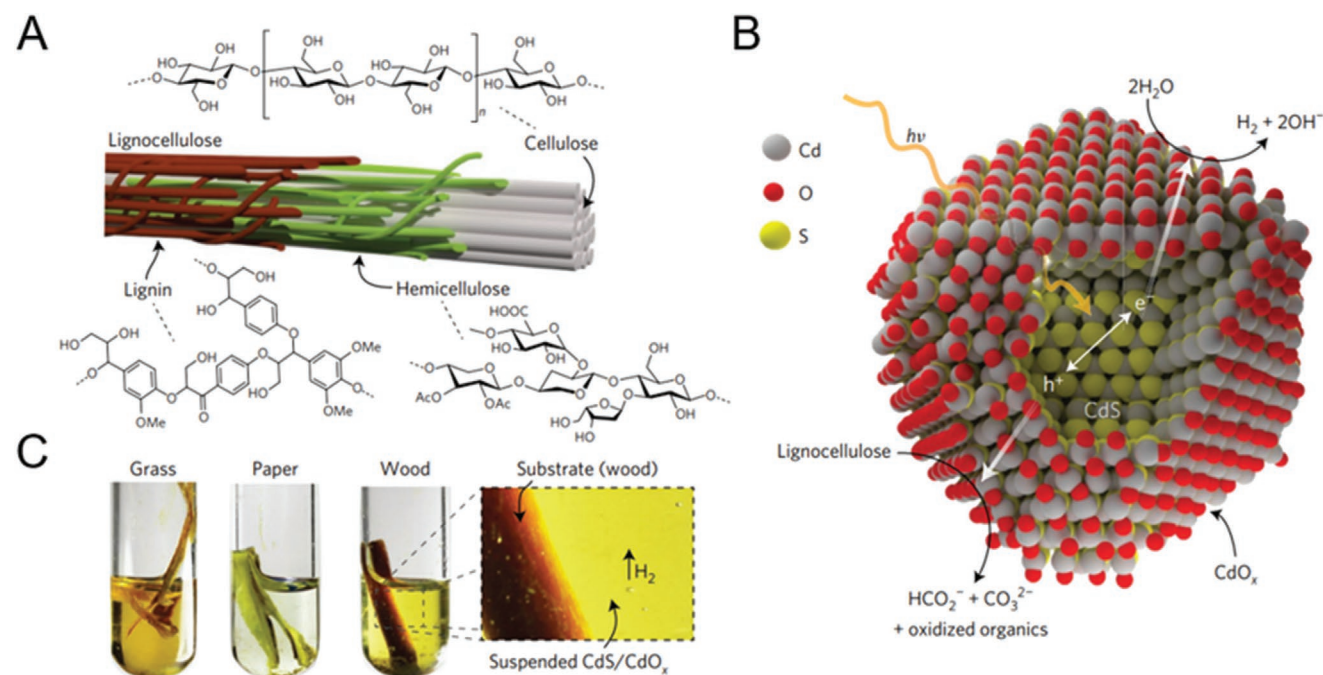


Figure 24. A) Structure of lignocellulose microfibrils within plant walls. B) Schematic representation of the photocatalytic lignocellulose reforming over CdS. C) Picture of the photochemical experiment with different biomass residues in a CdS/CdO_x solution. Reproduced with permission.^[342] Copyright 2017, Nature publishing group.

surface chemistry, defect chemistry, and colloidal properties, we encourage the reader to carefully design their experiments and thoroughly characterize their materials considering parameters such as (but not limited to) the photophysical properties, dispersibility, and colloidal stability of the particle semiconductor in the desired reaction mixture. In this regard, techniques such as zeta potential or dynamic light scattering measurements can provide meaningful insights in the particle size and distribution and colloidal stability. Additionally, photoluminescence, transient absorption, and transient photocurrent measurements can provide relevant information regarding the electron-hole separation properties of the photocatalyst and therefore about the hole scavenging properties of the biomass-derived alcohol. This kind of analysis could potentially open the gate to large scale production of sustainable chemicals with simultaneous production of clean hydrogen. In the upcoming sections we will provide a comprehensive summary of the most relevant works showing the production of biomass-derived valuable chemicals and hydrogen through photocatalysis, emphasizing the structure-activity relationships and reaction pathways on different semiconductors and cocatalysts surfaces.

6.2. Photocatalytic Biomass Oxidation Coupled to Hydrogen Production

Besides enhancing the photocatalytic performance of the semiconductor-driven hydrogen production, the utilization of a biomass-derived alcohol in those reaction media can lead to the selective production of oxidation products with high added value rather than just CO₂.^[326,352,353] The evaluation of the

production of such products is rather uncommon, partly due to the fact that often just gaseous products are analyzed (such as H₂ and CO₂), and as well owing to the difficulty of controlling the energy input and reaction rate in photocatalytic systems unlike the electrochemical approach. This issue leads often to the complete oxidation of the used hole scavengers to CO₂ rather than aldehydes, or carboxylic acids with commercial value. In this section, we will focus on the reports that have shown the rigorous transformation of biomass-derived alcohols (methanol, ethanol, glycerol, and HMF) in the corresponding liquid oxidation products through a thorough analysis of the reaction medium and provide meaningful mechanistic insights paving the way toward the large-scale production of such chemicals.

6.2.1. Methanol and Ethanol

As mentioned in the previous section, methanol and ethanol are some of the most utilized alcohols acting as hole scavengers in photocatalytic hydrogen production, and their dehydrogenation to formaldehyde or acetaldehyde, respectively, has been shown in literature with different semiconductors photocatalysts and experimental conditions. Sakata and Kawai showed in 1981 the photocatalytic production of hydrogen, methane, and acetaldehyde on Pt-TiO₂ materials at low temperature suspended in a water/ethanol mixture. The presence of acetaldehyde was attributed to the oxidation of ethanol by photogenerated holes and methane was suggested to be derived from the decomposition of acetic acid.^[354] Bamwenda et al. compared in 1995 the performance of Pt-TiO₂ and Au-TiO₂ in the same scenario, observing that when utilizing Au as cocatalyst the production rate of gases

(including H_2 , CH_4 , and CO_2) and liquids (mainly acetaldehyde) was 30% lower, owing to the better kinetics of Pt for hydrogen production.^[355] The adsorption and decomposition of ethanol on the surface of TiO_2 and in the presence of water was later shown by Nosaka et al. through NMR spectroscopy. The methyl protons ($-CH_3$) corresponding to ethanol ($-OH$ and $-CH_2$ signals overlapped with those of adsorbed water) were visible up to 385 K indicating the presence of adsorbed ethanol molecules in TiO_2 . Nevertheless, upon 1 h UV illumination the signals disappeared due to its decomposition.^[356] A similar study was carried out later by Schultz and co-workers interrogating the competitive adsorption between water and methanol on TiO_2 through the spectroscopic technique sum frequency generation. Results showed that methanol is both, physisorbed as well as chemisorbed as a methoxy group, and that those are more strongly bound than water molecules. This result would entail two feasible mechanisms for its photooxidation; its direct oxidation by photogenerated holes, and the indirect oxidation through OH radicals derived from water, depending on the methanol/water ratio.^[357] Further mechanistic insights supporting this hypothesis were provided by Chiarello et al. through a kinetic model supported by isotopic exchange experiments. Here the authors could observe that the reaction pathway in the photocatalytic production of formaldehyde and formic acid from a water/methanol mixture was determined by the chemical composition of the mixture. Namely, a higher water content entailed the indirect oxidation by hydroxyl radicals, while a high methanol concentration would result in its direct oxidation by a photogenerated hole to formaldehyde.^[358] A rate law analysis of methanol oxidation to formaldehyde on hematite and TiO_2 photoanodes under 1 sun illumination showed a reaction order of 2 and a high kinetic isotope effect of 20 (using CD_3OD). The authors suggested a first chemisorption step on the metal oxide forming a methoxy surface species which is then oxidized to a methoxyradical species and eventually to formaldehyde via a second valence band hole transfer leading to the abstraction of one of the methoxy-hydrogen atoms by a second Fe(v)-oxo site (Figure 25).^[359]

Puga elaborated a general route for their photocatalytic oxidation where the first step entails the formation of a hydroxy-alkyl radical which undergoes a dehydrogenation to form a carbonyl followed by proton-coupled oxidation to a carboxylic acid which then further oxidizes to an alkyl radical and CO_2 .^[326] The formed alkyl radicals then recombine with hydroxyl radicals back to alcohols that will be reformed in a new catalytic cycle.

Regarding semiconductor materials and cocatalysts often employed in these processes, metal oxides are some of the most widespread along with metal cocatalyst such as Pt, Ni, or Au. We would like to refer the reader to the review published by Cargnello et al. where they covered the state-of-the-art in the selective oxidation of methanol, ethanol and glycerol (amongst others) and simultaneous hydrogen production using metal oxides.^[360] Despite the numerous reports showing photocatalytic hydrogen production with metal oxides and others in water/methanol mixtures,^[361–364] the observation of oxidation products is rather difficult owing to its fast oxidation to CO_2 .^[365] Very recently, Heiz and co-workers elucidated the photochemical reaction steps for such reaction at the surface of a Pt cluster-loaded TiO_2 through Auger spectroscopy and isotopic

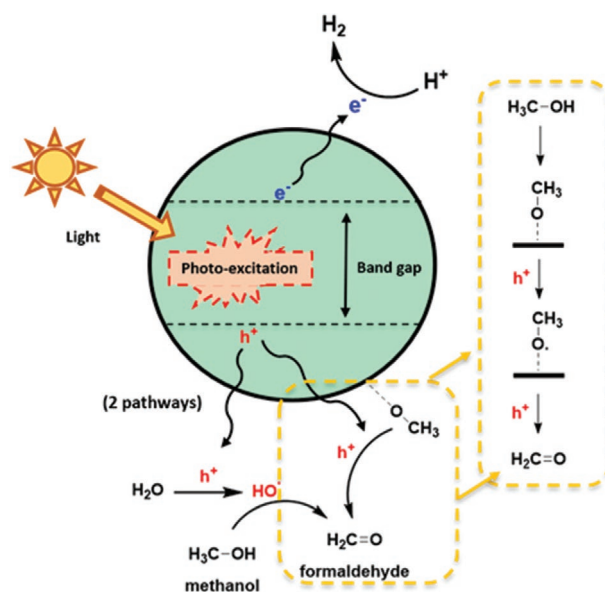


Figure 25. Reaction mechanisms for the oxidation of methanol inspired by reports from Mesa and Chiarello.^[358,359]

labeling amongst other techniques under photocatalytic conditions.^[366] In this work isotopically labeled methanol- d_3 was employed for monitoring the isothermal photoreaction, and upon illumination formaldehyde and molecular hydrogen were observed. Initially, hydrogen could be also seen owing to the dissociative adsorption of methanol or its thermal decomposition on the Pt surface leading to CO and H_2 . This fact was confirmed by a temperature programmed reaction experiment, where after methanol has been desorbed from TiO_2 , some still remained adsorbed at the Pt clusters which was dehydrogenated to CO.^[367,368] Experiments carried out under CO saturation produced formaldehyde and hydrogen. Additionally, the similarity in the formaldehyde decays in Pt- TiO_2 and bare TiO_2 samples implied that the photooxidation of methanol is not altered by electronic effects of the cocatalyst, leading the authors to propose a reaction mechanism where the photogenerated holes oxidize a methoxy species surface-bound to TiO_2 producing formaldehyde, while hydrogen is evolved at the Pt site. This mechanism was previously observed in catalytic experiments running on pure methanol, on semiconductors such as MgO or carbon nitrides and is in good agreement with the mechanism in Figure 25 and the work of Chiarello et al. in the gas phase.^[358,369,370]

In the case of ethanol, the reaction mechanism in Pt- TiO_2 proceeds in the same manner than that of methanol, with ethoxide surface bonded groups that are oxidized to acetaldehyde and the protons reduced on the surface of Pt.^[371] Several reports can be found in literature employing metal oxide materials with different cocatalysts and nanostructures showing production of acetaldehyde and other oxidation products.^[372] Fornaseiro and co-workers employed CuO_x-TiO_2 photocatalysts in a 50% ethanol aqueous solution and observed that the main product was acetaldehyde (nearly $250 \mu mol h^{-1} g^{-1}$). Owing to ethanol dehydration, ethylene trace amounts were also observed at the very beginning of the photocatalytic process as well as methane

and ethane, these species were attributed to coupling reactions between hydroxyethyl radicals formed by interaction of ethanol and photogenerated holes.^[373] The same group later observed acetaldehyde being released from a water/ethanol solution with nanostructured Fe₂O₃ polymorphs.^[374] Murdoch et al. evaluated the effect of loading Au nanoparticles on TiO₂ in the photocatalytic performance for hydrogen production and ethanol oxidation. Anatase displayed a stronger electronic interaction with Au owing to its higher Fermi level which led to a higher catalytic activity with low Au loadings of 4 wt% of 3–12 nm sized particle, while increasing the loading to 8 wt% decreased the performance. As expected, the formation of acetaldehyde was predicted to happen through the oxidation of ethoxide chemisorbed on Ti⁴⁺ sites.^[375] A similar study was shown by Vizza and co-workers where Pd nanoparticles loaded on TiO₂ nanotube arrays promoted the photocatalytic activity toward the hydrogen production from water/ethanol, observing acetaldehyde and 1,1-diethoxyethane derived from the acetalization of acetaldehyde in excess of ethanol.^[376]

This body of works employs metallic cocatalysts to promote the electron–hole spatial separation and carry the reduction of protons to molecular hydrogen. Lorca and co-workers recently suggested a metal-free CoTiO₃–TiO₂ heterojunction for the overall photocatalytic process of H₂ and acetaldehyde production from a 10% ethanol solution and indeed saw enhanced charge separation via a sixfold increase in PL lifetime.^[377] The hybrids were prepared by phase segregation of a Co-doped TiO₂ precursor and the band alignment analysis suggested the recombination between the photogenerated electron in the CoTiO₃ conduction band (as it was not negative enough to carry the reduction of H⁺) with the photogenerated holes in the TiO₂ leading to spatially separated charge carriers.

The overall photocatalytic process mechanism with colloidal quantum dots differs slightly to those widely adopted for metal oxides. CdS is one of the semiconductor chalcogenides more utilized owing to its narrow bandgap (2.4 eV vs 3.2 eV for TiO₂) which allows it to operate under visible light.^[378] The difference

in the mechanism arises from the ligands coating the quantum dots which stabilize them in solution and separate their surface from the reagents owing to a secondary coordination effect.^[379] Implying that the oxidation of a given alcohol such as ethanol does not occur by the combination of a hole and chemisorbed ethoxide but through its interaction with hydroxyl radicals. This fact was suggested by Feldmann and co-workers which demonstrated the oxidation of ethanol to acetaldehyde with a colloidal cysteine-stabilized CdS photocatalyst with Ni as cocatalyst.^[380] In this work, at higher pH (14.7), the H₂ production was substantially higher (reaching up to 53% average quantum yield) owing to the implication of ⁻OH anions in the photocatalytic process (Figure 26). Later in 2016, Chai et al. showed the production of H₂ in pure alcohol solutions (Including methanol, ethanol, and 2-propanol) employing a Ni/CdS photocatalysts.^[381] The proposed mechanism in this case entailed the formation of Ni–H hydride by abstraction from the corresponding alcohol and the formation of an alkoxide anion which is oxidized by a photogenerated hole. Finally, the cleavage of an α C–H bond, leads to the formation of the corresponding ketone and molecular hydrogen.

6.2.2. Glycerol

Glycerol is a symmetric molecule, and in the same way than with methanol and ethanol, its oxidation with simultaneous hydrogen production can happen through direct oxidation by a photogenerated hole or through hydroxyl radicals generated by oxidation of water. After the photoinduced charge transfer either of the terminal hydroxyl groups can be oxidized to an aldehyde, which leads to the production of glyceraldehyde, and if the oxidation happens in the central hydroxyl group dihydroxyacetone is obtained. Oxidation products derived from C–C carbon bond scission, such as formaldehyde and glycolaldehyde, are less common and the reaction mechanism leading to those, less studied.^[382] Additionally the reduction of protons to molecular

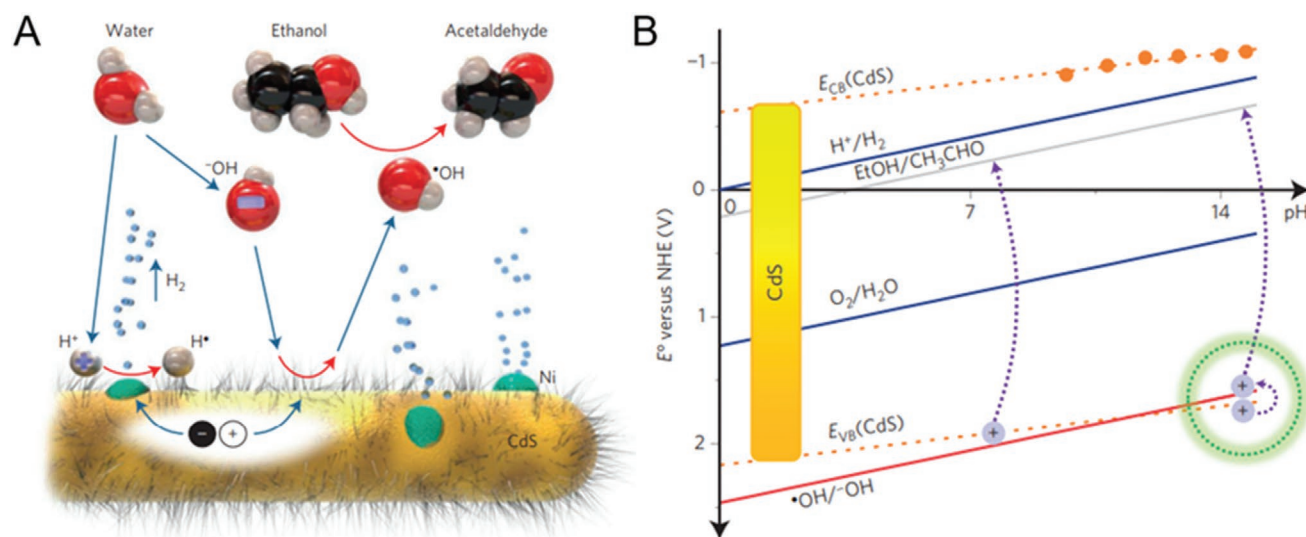


Figure 26. Schematics of the photooxidation of ethanol to acetaldehyde over Ni-decorated CdS rods mediated by A) OH radicals, and B) band structure variation with pH of such catalyst. Reproduced with permission.^[380] Copyright 2014, Nature publishing group.

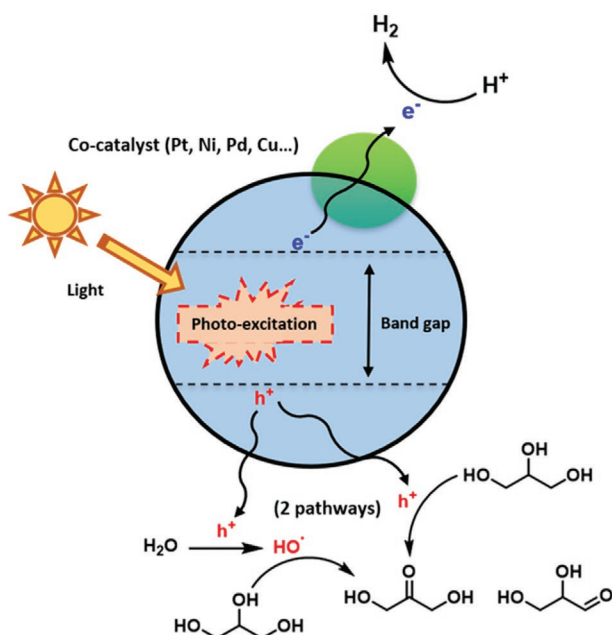


Figure 27. Schematic representation of the photocatalytic hydrogen production and glycerol oxidation to glyceraldehyde and dihydroxyacetone.

hydrogen happens in the cocatalyst loaded on the semiconductor (Figure 27), we would like to refer the reader to the review published recently by Iliuta and co-workers for a comprehensive overview of the implications of synthetic pathways and cocatalyst loading in the hydrogen evolution performance from glycerol.^[383] Despite the large body of works published showing hydrogen production from glycerol or its catalytic oxidation independently,^[384–387] the ones that do actually tackle reaction parameters to obtain and quantify both hydrogen and high added value liquid products are rather scarce.^[388]

Minero and co-workers evaluated the rate of formation of both glyceraldehyde and dihydroxyacetone on TiO₂ materials observing a pseudo first-order kinetic constant reaching 85% glycerol conversion, the trend can be assumed to correlate as well with the hydrogen production.^[389] Variation in the reaction conditions showed that at neutral pH the glycerol disappearance rate increases substantially (by a factor of 2.5). This fact was confirmed by Li et al. which showed that at pH 6.4 the hydrogen evolution and the conversion to glyceraldehyde were substantially higher, proving as well that the effect of glycerol concentration on the overall performance followed a Langmuir–Hinshelwood model. This fact implies that the hydrogen production rate increases sharply with higher glycerol concentrations.^[390] Nevertheless, the solution pH typically tends to lower down owing to the presence of dihydroxyacetone, glyceraldehyde and other acids. Jiang et al. showed that the solution pH tends to stabilize to 3.5.^[349] In 2011 Fornaseiro and co-workers employed Cu–TiO₂ materials as photocatalysts, which had been shown previously for the hydrogen production from glycerol,^[391,392] and upon analysis of the liquid phase they could detect as main products 1,3-dihydroxypropanone (dihydroxyacetone) and hydroxyacetaldehyde (glycoaldehyde), suggesting the C–C bond scission in glycerol, although no carboxylic acids were observed. Additionally, an optimal loading of 2.5% of

Cu led to the highest hydrogen production activity under UV illumination, up to 1600 μmol h⁻¹ g⁻¹.^[393] Cu nanodots-TiO₂ nanosheets were later further studied showing that Cu redox processes (Cu⁺ → Cu²⁺) could as well take part harvesting photogenerated charges. Glycerol was suggested to be adsorbed on the Ti–OH sites and oxidized to intermediates such as glyceraldehyde or glycoaldehyde through photogenerated holes or hydroxyl radicals and finally transformed to CO₂.^[394] A kinetic model for this system was later proposed by Clarizia et al. capable to simulate the hydrogen production over such catalyst (Cu–TiO₂) in water/methanol or water/glycerol mixtures as well as their adsorption constants based on a Langmuir–Hinshelwood-type model.^[395]

Kondarides and co-workers elucidated the differences between carrying the photocatalytic process with TiO₂ and Pt–TiO₂ in the presence and absence of oxygen, differentiating them as photooxidation and photoreforming respectively.^[396] The gas phase (H₂ derived from proton reduction and CO₂ from the complete oxidation of glycerol) and liquid phase products were analyzed as a function of time. In the presence of O₂ they could observe that the complete oxidation of glycerol occurred much faster, owing to its interaction with H₂O₂ generated from O₂ reduction, and therefore no hydrogen was observed. In the absence of O₂, less CO₂ was observed owing to the slower oxidation of glycerol and H₂ was produced as the photogenerated electrons had no competition with the oxygen reduction. The liquid products observed in all the scenarios were the same, acetol, acetaldehyde, ethanol, and methanol in a higher concentration and traces of glyceraldehyde and glycoaldehyde. This suggests that the absence or presence of Pt or O₂ just influences the HER and the overall rate of product formation rather than reaction mechanism. The presence of these products in the liquid-phase as well as the evolved hydrogen were attributed to glycerol deprotonation prior to cleavage of the C–C and C–O bonds. As mentioned in Section 1, we would like to note that the photocatalytic oxidation of glycerol under aerobic conditions, where photogenerated electrons reduce oxygen rather than protons, has been more widely studied, nevertheless it falls outside of the scope of this section and therefore we would like to refer the reader to recent reviews and previous literature published on this topic.^[326,383,397–399]

Arai and co-workers evaluated in depth the role of water in the photocatalytic hydrogen production from glycerol water mixtures by using D₂O in their experiments with NiO–TiO₂ materials, which had been previously shown by the same group performing in the same reaction.^[400] They could observe that after 10 h of reaction, H₂, HD, and D₂ were detected but the relative amount of HD and D₂ was 1.5% compared to H₂, suggesting that glycerol acts as the main source of hydrogen.^[401] Further insights in the photocatalytic activity of TiO₂ materials for such reaction was provided later by Beltram et al. who prepared hybrid anatase–rutile and anatase–brookite composites in order to extend the lifetime of the photogenerated charges. During the photocatalytic experiments they could detect glycoaldehyde, glyceraldehyde, hydroxyacetone, and dihydroxyacetone in the liquid phase, as well as H₂ and CO₂ in the gas phase.^[402] These results indicate that the glycerol oxidation reaction in photocatalysis follows similar pathway as described in Section 4.2.

6.2.3. HMF

As mentioned previously in Section 4.4, HMF oxidation can lead to the production of value-added products such as DFF and FDCA, which are molecules with commercial interests in fields such as pharmaceuticals, polymers or in organic synthesis.^[403] Therefore obtaining these chemicals using photocatalysis producing hydrogen as a byproduct has attracted widespread attention within the last years. In this scenario electron-hole pairs generated by photoexcitation of a semiconductor travel toward the surface where electrons reduce H^+ to H_2 (typically in the metallic cocatalyst) and the holes react with water to form OH radicals or directly with HMF, releasing the oxidation products.^[404,405]

Diaz and co-workers employed graphitic carbon nitride, which displays a more favorable energy band structure than TiO_2 , for the direct photooxidation of HMF in aqueous solution. The initial adsorption of HMF in the surface of the photocatalyst reached around 3% of the initial concentration, probably happening through hydrogen bonding between amine moieties and OH groups. Upon illumination they could observe that the degradation rate of HMF was faster than the formation rate of DFF indicating alternative oxidation pathways that remained unexplored. The most active material, whose active area was enhanced by thermal treatment showed a 69% conversion of HMF to DFF.^[406] In order to elucidate the reaction mechanism the photocatalytic process was carried out in the presence of different scavengers; tert-butyl alcohol (OH radical scavenger) did not alter the conversion rate, but the addition of sodium formate as a hole scavenger decreased it substantially, indicating a direct oxidation by photogenerated holes rather than through radicals. Experiments employing cupric ions and benzoquinone (as electrons and O_2 radicals' scavengers, respectively) demonstrated that photogenerated electrons take part in the formation of superoxide radicals which are the main active specie. This suggests that the lack of a cocatalyst with minimum overpotential for the hydrogen evolution would not lead to simultaneous H_2 and oxidation products when using carbon nitride materials. Later, Kailasam and co-worker further used carbon nitride along with a Pt cocatalyst for the simultaneous hydrogen production and selective oxidation of HMF to DFF (Figure 28).^[407] Under reaction conditions they obtained $12 \mu\text{mol H}_2 \text{ h}^{-1} \text{ m}^{-2}$ (slightly less than when using triethanolamine, a very common hole scavenger in photocatalytic hydrogen production, owing to the weaker electron donating abilities) and $1.3 \mu\text{mol DFF h}^{-1} \text{ m}^{-2}$ with 99% selectivity. This remarkably high selectivity emerges likely from the relatively high valence band maximum of carbon nitrides which is not deep enough to generate OH radicals and therefore the photogenerated holes react directly with HMF. Furthermore, experiments with D_2O confirmed that the hydrogen produced emerges from water rather than HMF, and the utilization of sodium persulfate (an electron scavenger) instead of Pt revealed that the role of the cocatalyst is restricted to the reduction of protons to hydrogen and does not take part in the oxidation of HMF.

The photocatalytic hydrogen production with conversion of HMF and furfural alcohol was shown later in Ni-CdS materials by Han et al. which showed that by tuning reaction conditions they could alter the selectivity to either aldehyde or acids as

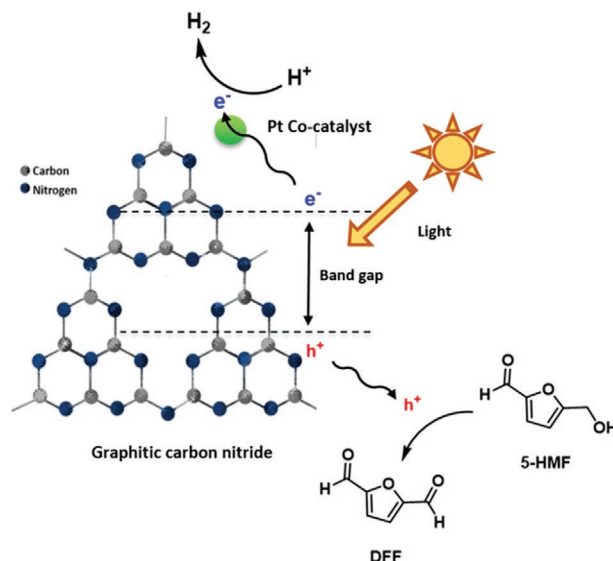


Figure 28. Schematic representation of the photocatalytic hydrogen production and HMF oxidation to DFF with carbon nitride.

oxidation products.^[408] After 22 h illumination, 20% conversion of a $10 \times 10^{-3} \text{ M}$ HMF solution to DFF was achieved with nearly 100% selectivity. Both the conversion rate and the hydrogen produced was considerably lower when transforming HMF than when employing furfural alcohol. This was attributed to the higher binding affinity of aldehyde groups to Ni-CdS in the presence of water versus that of alcohols, which makes the oxidation of the latter unfavorable. Nevertheless, under highly alkaline conditions (10 M NaOH) the conversion to FDCA was complete owing to the low stability of aldehydes and their degradation to alcohols and carboxylic acids. Chen and co-workers employed modified chalcogenides ($\text{P-Zn}_{0.5}\text{Cd}_{0.5}\text{S}$) and observed an enhancement from 419 to $786 \mu\text{mol h}^{-1} \text{ g}^{-1}$ for the HER upon addition of HMF to the reaction medium.^[409] After 8 h the conversion of HMF to DFF reached 40% with a selectivity of 65% and the hydrogen evolution rate decreased substantially owing to the consumption of HMF. $\text{Zn}_{0.5}\text{Cd}_{0.5}\text{S}$ was further employed along with MnO_2 forming a type II heterojunction with enhanced reduction and oxidation power of the photogenerated electrons and holes, respectively. Nagaraja and co-workers obtained $1322 \mu\text{mol H}_2 \text{ g}^{-1}$ and a DFF yield of 46% in 24 h with such material. Additionally replacing water by an aprotic solvent such as acetonitrile reduced the production of DFF to just a 3% and $6.8 \mu\text{mol H}_2 \text{ g}^{-1}$, suggesting a major role of water in both reduction and oxidation processes.^[410] The utilization of low-dimensional heterostructured materials is highly appealing owing to the wide range of possibilities to tailor the electronic band structure by combining different 2D materials.^[411,412] ZnIn_2S_4 was very recently shown by several research groups and in combination with other semiconductors (such as Nb_2O_5) to be able to drive the photocatalytic hydrogen evolution and simultaneous oxidation of HMF. In this scenario employing semiconductors with a deep enough valence band can result in the formation of OH radicals that assist in the oxidation of the biomass-derived residue.^[413,414]

6.3. Cross-Coupling and Hydrogen Evolution

Besides the oxidation of biomass-derived residues, creating new C–C bonds with concomitant hydrogen production can lead to the production of high added value products and sustainable fuels. In this kind of reactions, the light-absorbing semiconductor catalyst drives a cross-coupling reaction and simultaneously reduces the protons eliminated from the C–H bonds of the educt resulting in molecular H₂. Wu and co-workers explored this phenomenon for the first-time utilizing eosin Y-sensitized graphene-supported RuO₂ without sacrificial agents. In this work eosin Y took the role of a photosensitizer promoting the cross-coupling of *N*-phenyl-1,2,3,4-tetrahydroisoquinoline with indoles under visible light, while RuO₂ supported on graphene acted as a proton and electron sink for the elimination of C–H bonds.^[415]

After the initial reports, these kind of cross-coupling HERs where quickly expanded to biomass-derived substrates.^[416] Luo et al. showed the visible-light H₂ production from benzyl alcohol with controllable generation of benzoin and desoxybenzoin through tandem redox reactions utilizing a ZnIn sulphide photocatalyst, which allowed to obtain value-added chemicals on gram scale.^[417] In this case, a photogenerated hole induced the dehydrogenative coupling of benzyl alcohol, and subsequent C–C coupling. Xie et al. showed for the first time the direct photocatalytic transformation of methanol and water into ethylene glycol and hydrogen over a molybdenum disulphide nano-foam-modified cadmium sulphide nanorod. In that work they could observe a preferential activation of the C–H bond instead of O–H in methanol which was driven by the photogenerated holes in CdS through a proton–electron transfer mechanism, giving rise to a hydroxymethyl radical.^[418] The dehydrogenative coupling of methane to ethane with synergistic production of H₂ under visible light irradiation was confirmed by Meng et al. utilizing hybrid Au/ZnO porous nanosheets.^[419] Methane is a chemical often obtained after the gas-phase reduction of atmospheric CO₂^[420,421] but its direct and efficient dissociation and conversion to ethane and hydrogen remained a standing challenge due to the weak adsorptive interaction of methane with catalysts and small polarizability. In this work, the Au-plasmon-induced resonance energy triggered the stoichiometric conversion after the C–H bonds have been chemisorbed onto the polar oxide semiconductor surfaces, obtaining higher efficiencies than previously reported catalysts such as Zn⁺-modified zeolites.^[422]

6.4. Photoelectrochemical Oxidation and Hydrogen Production

The advantage of photoelectrochemical cells is the study of one half reaction at a time (at the working electrode) while the other half reaction (at the counter electrode) is not of primary concern owing to the use of a reference electrode (Figure 29A).^[423,424] Similarly to photocatalytic approaches, oxide semiconductor catalysts are commonly employed as photoanodes, and materials such as TiO₂, hematite, and BiVO₄ have been amongst the most commonly studied. Given the wide bandgap of TiO₂ (3.2–3.4 eV), approaches for enhancing its performance, such as sensitization, doping, nanostructuring,^[425–427] as well as the development of other smaller bandgap semiconductors with increased photon-to-hydrogen efficiency have been extensively sought after.^[428–431] In the same manner to powder photocatalysis, the photoelectrochemical synthesis of organic molecules and the conversion of biomass derivatives and water to H₂ and CO₂ is thermodynamically much more favorable,^[432–435] and therefore plenty of photoanodes, cell configurations, and electrolytes containing biomass-derived molecules have been reported within the last decade.^[322,436]

One of the first reports on the photoelectrochemical generation of H₂ from a water/ethanol mixture was carried out by Antoniadou et al. where a chemically-biased H-type photoelectrochemical cell based on nanocrystalline TiO₂ was utilized for the oxidation of ethanol to acetaldehyde with synergistic H₂ production under UV light illumination. In order to create enough chemical bias, a basic electrolyte (NaOH) was utilized in the anode compartment and an acidic electrolyte in the cathodic compartment (H₂SO₄), and upon addition of 20% v/v ethanol a maximum current (*J*_{sc}) of 0.89 mA cm⁻² was obtained under illumination at λ = 360 nm (intensity 0.8 mW cm⁻²).^[438] The same group later evaluated the performance of CdS-decorated TiO₂ for the photoelectrochemical oxidation of different substrates, including short chain alcohols, glycerol, ammonia, urea, and others, coproducing H₂ at the cathode.^[439–441] The utilization of TiO₂ based photoanodes for hydrogen production from biomass has been later shown by other groups; Bashiri et al. utilized Cu and Ni-modified TiO₂ electrodes prepared at different temperatures for the photoelectrochemical oxidation of glycerol under visible light. They could observe the production of 694.84 μmol H₂ after 2 h when measuring in KOH with 10% v/v glycerol and 5 mol% Cu-Ni/TiO₂ as photoanode upon 1 sun illumination (AM 1.5G, 100 mW cm⁻², λ > 360 nm).^[442]

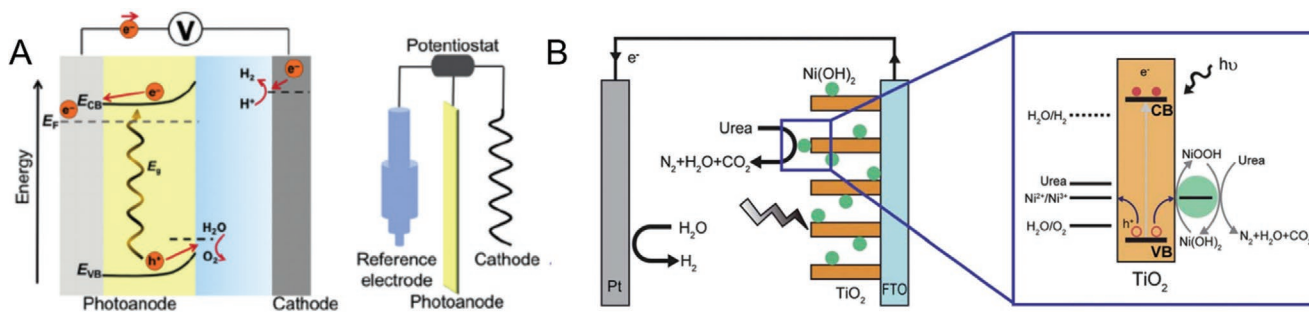


Figure 29. A) Scheme of a water splitting photoelectrochemical cell. Reproduced with permission.^[430] Copyright 2019, John Wiley & Sons. B) Photoelectrochemical cell for urea oxidation. Reproduced with permission.^[437] Copyright 2012, Royal Society of Chemistry.

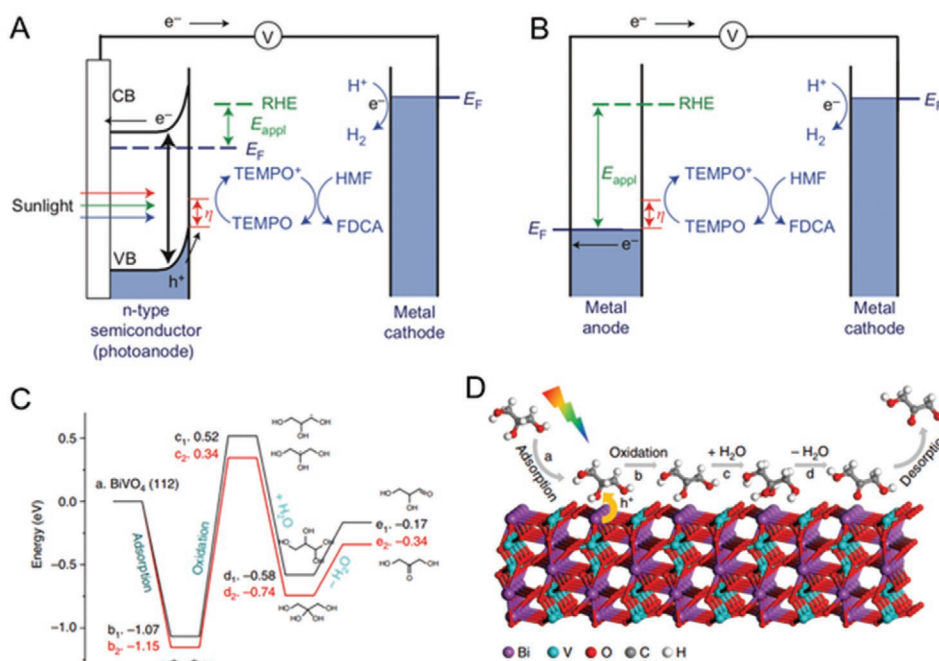


Figure 30. Scheme of A) photoelectrochemical and B) electrochemical oxidation of HMF. Reproduced with permission.^[446] Copyright 2015, Nature publishing group. C) Energy profile and D) schematic illustration of glycerol conversion to 1,3-dihydroxyacetone over BiVO₄. Reproduced with permission.^[450] Copyright 2019, Nature Research.

Hematite (Fe₂O₃) is a widely utilized semiconductor material in photoelectrochemical cells owing to its suitable bandgap of ≈2 eV with a very positive valence band edge. Zhang et al. utilized Ti-doped hematite photoanodes prepared through atmospheric pressure chemical vapor deposition of Fe(CO)₅ and TiCl₄ on fluorine-doped tin oxide (FTO) for the photoelectrochemical oxidation of glucose. The addition of 10 × 10⁻³ M glucose to the electrolyte boosted the performance due to its easier oxidation versus water, reaching incident photon-to-current efficiencies of up to 21.2% at 0.4 V versus Ag/AgCl and illumination under 400 nm wavelength.^[443] The kinetics of the photoelectrochemical oxidation of methanol to formaldehyde on hematite was studied by Durrant and co-workers, where photoinduced absorption spectroscopy was utilized in order to correlate the density of surface holes with photocurrent measurements. Here, the addition of methanol to the electrolyte (95% methanol in NaOH 0.1 M) enhanced the current from 2.6 (in 0.1 M NaOH) to 3.9 mA cm⁻² at 0.55 V versus Ag/AgCl and 1 sun illumination and formaldehyde was formed with a 96% Faradaic efficiency. Additionally, they observed that the kinetics of methanol oxidation are independent of the applied potential and are determined by the density of holes accumulated at the electrode surface.^[359] Recently, Mazzaro et al. further employed hydrothermally prepared Ti-doped nanostructured hematite electrodes for the photoelectrochemical oxidation of benzylamine to N-benzylidenebenzylamine with simultaneous H₂ production.^[444] Hematite and other metal oxides were utilized as well for the photoelectrochemical oxidation of urea. Li and co-workers observed for the first time stable hydrogen production in the Pt cathode when utilizing Ni(OH)₂-decorated TiO₂ or hematite for the solar-driven oxidation of urea. In this

scenario upon illumination the photogenerated holes oxidize Ni(OH)₂ to NiOOH which catalyses the degradation of urea to N₂ and CO₂, while the photogenerated electrons reduced water molecules on the surface of Pt (Figure 29B).^[437]

Some interesting example is the study by Berlinguette and co-workers demonstrating the photoelectrochemical oxidation of organic molecules on BiVO₄ photoanodes.^[445] Their application for hydrogen production from biomass was shown in 2015 by the photoelectrochemical oxidation of 5-HMF to FDCA. In this work a n-type, nanoporous BiVO₄ photoelectrode was utilized along with TEMPO as mediator. Upon illumination, the photogenerated holes oxidize HMF and the electrons produce H₂ molecules in the Pt cathode with only a minor potential bias due to the insufficiently high conduction band of BiVO₄ (Figure 30A,B).^[446] Chadderdon et al. employed a cobalt phosphate overlayer in BiVO₄ for alleviating recombination losses in the same system and obtained 88% conversion of HMF to FDCA at 0.64 V for 2.7 h. In these reports, TEMPO is oxidized by the photogenerated holes instead of water in the surface of the photoanode which then oxidizes the organic substrate as shown in Figure 30A,B.^[447] Later BiVO₄ was also applied for the photoelectrochemical oxidation of glycerol to dihydroxyacetone, widely utilized in different industries.^[448,449] Liu et al. showed that under AM 1.5G from illumination and pH = 2, nanoporous BiVO₄ reached 3.7 mA cm⁻² photocurrent at 1.2 V_{RHE}, corresponding to 56 mmol g⁻¹ h⁻¹ and 51% selectivity toward dihydroxyacetone. Isotopically labeled experiments along with DFT calculations confirmed that the reaction mechanism consists of adsorption of glycerol and subsequent oxidation by photogenerated holes, reaction with water and dehydration. DFT calculations were carried out on the main exposed crystal facets

of BiVO₄, (112). Results shown that the terminal and middle hydroxyl groups were absorbed spontaneously through electrostatic attractions toward Bi³⁺. Their oxidation by photogenerated holes lead to the formation of radicals, being the one in the middle carbon 0.18 eV more stable than the terminal ones, this fact supports the oxidation toward DHA (Figure 30C,D).^[450]

Unlike the electrochemical approach, the photoelectrochemical oxidation of biomass-derived molecules is highly dependent on the hole population in the valence band of the photoelectrode, rather than the applied voltage, as has been confirmed in hematite and bismuth vanadate photoanodes.^[359,450] This fact could shed light in the structure–activity relationships, and target the selective production of a given chemical by rational electronic band structure engineering. The photoelectrochemical approach addresses some of the drawbacks of the photochemical counterpart, such as the lack of understanding in the parameters determining selectivity. However, nowadays there are not enough studies showing the tendency of widely utilized semiconductors toward certain chemicals and therefore a thorough investigation joining both computational insights with rigorous experimental protocols is needed to target a large-scale production.

Despite the recent progress in the field, there is a lack of fundamental understanding of these multielectron transfer reactions in the surface of traditional semiconductors. Unlike the electrochemical biomass oxidation with synergistic hydrogen production, where modulating the voltage or the crystalline faces of an electrocatalyst can determine the selectivity of the reaction, establishing structure–activity relationships in the photon-driven counterparts is significantly challenging. Furthermore, controlling the degree of oxidation has been proven to be highly challenging, obtaining often the fully oxidized CO₂ rather than high-added value aldehydes or acids. Considering this, and with the aim to facilitate future research and the advancement of the topic we recommend several points to be addressed in upcoming works.

- 1) The reaction media shall be better controlled (i.e., thoroughly purged with an inert gas such as N₂ or Ar to removed dissolved oxygen). Oxygen can react with photogenerated electrons forming superoxide radicals and hydrogen peroxide which are highly oxidizing agents, this reaction is in direct competition with the reduction of protons to molecular hydrogen, additionally these species will accelerate the oxidation of the organic substrate.^[406]
- 2) Both produced H₂ and oxidation products must be thoroughly quantified, and their production plotted versus time and amount of employed catalyst (μmol X h⁻¹ g⁻¹), additionally, average quantum yields for hydrogen production at different wavelengths shall be also provided. Techniques such as gas chromatography, 1H and 13C-NMR, or HPLC will enable the accurate determination of the gas and liquid-phase products present in the reaction media. Reporting the turnover frequency would be even more desirable especially when studying single atom catalysts or comparing oxide versus metallic active sites. The thorough evaluation of both reduction and oxidation products will facilitate the establishment of state-of-the-art values for different materials and synthetic conditions leading to their integration in continuous flow reactors.^[451,452]
- 3) To maintain a constant production of high-added value chemicals and avoid the decrease in the H₂ production and the complete oxidation of the biomass-derived organic molecule to CO₂, aliquots of the hole scavenger shall be added periodically to the reaction media. The intervals will strongly depend in the electron–hole pair generation ability of the employed semiconductor as well as the reaction conditions. Ideally, the utilization of a flow cell would also help overcoming such issues.
- 4) The reaction mechanism shall be thoroughly explored using adequate scavengers such as Ag⁺,^[453] triethanolamine,^[350] benzoquinone,^[454] sodium persulfate,^[407] tert-butanol,^[455] and others.^[456] These can react with photogenerated electrons, holes, superoxide radicals and hydroxyl radicals therefore removing them from the reaction media and providing meaningful insights regarding the reaction mechanism and active species. Those scavengers shall be rationally selected as some may deposit irreversibly in the surface of a given catalyst blocking potential active sites.
- 5) An energy band diagram including the conduction and valence band potentials of the employed semiconductors and photovoltage generated as well as the oxidation and reduction potential (and overpotentials) of the involved species should be reported. Approximate values of the electronic band structure of semiconductors can be obtained with a combination of techniques such as Mott–Schottky electrochemical measurements (Fermi level in the flat band condition and carrier density) or (ultraviolet) photoelectron spectroscopy (Fermi level–valence band minimum offsets), UV–vis measurements and Tauc plots (direct and indirect bandgaps and sub-bandgap absorption features due to trap states).^[307,457,458] These plots will help elucidate the most feasible reaction pathway.
- 6) Despite the high number of reports dedicated to study reaction mechanisms and intermediates on the surface of TiO₂ materials, plenty of novel semiconductors have emerged as photocatalysts for different reactions such as chalcogenides, carbon nitrides, and others. Owing to the different surface chemistry of each semiconductor, the adsorption mode, namely, physisorption or chemisorption, and binding strength of biomass-derived molecules on the catalyst surface will strongly differ. Density functional theory calculations in combination with time-resolved spectroscopic studies could shed light on the different interactions between substrate and reactant helping to gain further insights in the oxidation pathway of such molecules.

7. Technology Status, Challenges, and Opportunities

7.1. Challenges and Potential Mitigations

The aforementioned research advances have shown the great potential for biomass electrolysis technology in H₂ and value-added chemical production, using both renewable electricity and/or solar energy. Our life cycle analyses presented in Section 2 have indicated that the environmental impacts associated with the reactants need to be reduced to improve its global potential, cost-benefit, and desirability of use.^[459] Apart from the common limitations similar to that of water electrolysis,

such as PGMs dependence and sluggish anode kinetics, some specific challenges from biomass electrolysis and potential mitigations have been discussed in the following sections.

7.1.1. Feedstock Availability and Reproducibility

Bioenergy with carbon capture and storage is considered central to many climate mitigation policy pathways set by the Intergovernmental Panel on Climate Change,^[460] and its large-scale deployment may compromise the availability of biomass for electrolysis. However, although carbon capture and storage is effective in the short-run to achieve net-zero emission by 2050, in the long-run beyond 2050, closing the carbon cycle is essential.^[461] Therefore, the biomass availability in a longer term will not be the major issue and the biomass valorization via electrolysis or other low-carbon technologies will still be promising.

However, significant improvements are needed to reduce the carbon intensity of biomass feedstocks in the near-term, especially for feedstocks such as glycerol. Conventional crops used for glycerol production have high impacts from land use change, with very high emissions for palm oil (231 g CO_{2,eq}/MJ), soybean oil (150 g CO_{2,eq}/MJ), rapeseed oil (65 g CO_{2,eq}/MJ), and sunflower oil (63 g CO_{2,eq}/MJ).^[462] These land use change effects primarily arise from peatland oxidation following land conversion, and deforestation. Two factors are particularly important for reducing the carbon intensity of these feedstocks—increasing the energy yield of crop per hectare and reducing deforestation for crop production. The latter has wider benefits for biodiversity and the ecosystem at large. In comparison to the above oils, ethanol feedstocks such as sugar and starch have much lower land use change emissions and may constitute a more sustainable alternative in the near-term. The variation in the feedstock market price and composition, such as the metal contents in raw biomass and the fatty acid proportion in crude glycerol will influence the actual implementation of this technology. An approach to overcome this limitation is to develop robust electrolyzer systems, with high chemical resistance, active and high poison-tolerant catalysts. This would allow the direct utilization of raw biomass feedstock or even biowaste (i.e., food waste), such as food or forestry/agricultural wastes.

Another approach is to fractionate and purify the raw materials with some existing technologies, for example, low-cost ionic liquids,^[463] to achieve higher activity and selectivity in biomass electrolysis, whilst prolonging the electrode lifetime. On the other hand, methods for separating biomass into well-established components are now well implemented, yet their environmental inputs will depend on the process used.^[464–466] A life cycle analysis carried out by National Renewable Energy Laboratory of U.S. DOE office have predicted that depending on the fractionated and separated products obtained from lignocellulosic biomass, it is possible to achieve large greenhouse gas offset targets.^[467,468]

7.1.2. Determination of Optimum Electrochemical Cell Materials, Design, Operation, and Economics

As the operating system is more complicated than water electrolysis, the reactor design, fabrication, and operation require

careful optimization. Parameters such as reaction temperature,^[261] electrode distance,^[263] analyte feed,^[264] and flow dynamics^[469] need to be investigated thoroughly to reach the optimal condition. Ramis et al. investigated the operation conditions for glucose reforming in two semipilot scale photoreactors.^[452] The authors have shown that high H₂ productivity was achieved at high temperature (60–80 °C) and moderate pressure (2–4 bar above ambient value). Colmenares and co-workers designed TiO₂-coated continuous flow microreactors for the partial oxidation of benzyl alcohol, which have showed improved irradiation, shorter reaction time, and better product yield compared to batch reactors.^[451] With commercial P25 TiO₂ catalyst, the flow microreactor exhibits a lower specific conversion of 5 μmol m⁻² min compared to the batch reactor (13 μmol m⁻² min), but higher benzaldehyde selectivity of 79% compared to 32%. This study demonstrated that increasing the catalyst availability by continuous flow can tune the product selectivity, which is crucial in obtaining high-value chemicals via partial oxidation. Similarly, Latsuzbaia et al. performed continuous electrochemical oxidation of HMF in a flow filter press tape reactor with integrated product separation unit.^[470] The set-up demonstrated 3 wt% FDCA production with a rate of 550 mL h⁻¹ and 84% Faradaic efficiency, and a separation yield of up to 95%.

7.1.3. Oxidation Product Recovery

Considering the operation complexity in biomass electrolysis, positive energy payback needs to be achieved by operating with minimum conversion steps and shorter processing times. The energy required to sustain a growth rate must also be taken into account.^[471] Kim et al. developed a process design and techno-economic assessment for glycerol electrolysis, indicating that the revenues would still match the costs with the minimum selling point of H₂ and chemicals despite greater product separation costs.^[43] In other systems, even mixed product streams can have economic value. For example, partially oxidized cellulose nanofibrils is one of the largest biopolymers and have applications in rheology modification for aqueous formulation.^[472] Still, the development of energy and cost-effective separation processes, for example, crystallization in γ-valerolactone/H₂O for recovering FDCA with >99% purity, would allow large scale HMF electrolysis with reduced operation costs.^[473] High selectivity (>90%) toward target products would also contribute to the simplification of the recovery process.

It has been shown that biomass electrolysis operated in alkaline condition typically exhibit higher activity, higher feedstock conversion as well as better selectivity by inhabiting C–C bond cleavage. However, the recovery of salt from products is rather difficult, and the carbon footprint associated with KOH usage leads to a higher environmental impact. Besides, although some salts such as potassium acetate have higher market value than acetic acid, many other organic acids such as lactic acid, FDCA are primarily used in the acidic form. Although these problems can be partially tackled by running at acidic conditions with H₂SO₄, which have a much lower global warming potential (0.17 kg CO_{2,eq} kg⁻¹), the separation of SO₄²⁻ with Ca(OH)₂ is another factor that would add on the uncertainty. Electrodialysis

constitutes a good strategy for the recovery of these acids and KOH.^[37,38,474] For example, Saxena et al. have demonstrated that 70–82% lactic acid recovery with 100% purity along with NaOH can be achieved with a single-step anion-exchange membrane electro dialysis process.^[475] However, the energy consumption associated with this process is 6.23 kWh kg⁻¹ for lactic acid production, which would add to the operational cost. A thorough process modeling coupled with techno-economic assessment and life cycle analysis is required to fully evaluate the potential of these different scenarios.

Alternatively, the implementation of anion exchange membrane electrolysis system with pure water as electrolyte feed could conceivably get around this problem, which still maintaining the low electricity consumption advantage. PEM-based systems use this kind of configuration for H₂O₂ producing electrolyzers for water treatment, which produces an effluent of H₂O₂ in pure water.^[476] However, extensive research efforts are still required to develop stable, highly conductive hydroxide exchange membranes.^[477]

7.1.4. Product Value-Chain: Partial Oxidation versus Reforming

The choice of biomass partial oxidation or reforming process can affect the product value-chain, depending on the type and yield of final products. Partial oxidation can lead to the coproduction of high-value chemicals, although it is associated with a potentially sacrificed activity, lower H₂ evolution rate, as well as the need for product recovery units that increase the CapEx. Depending on the price for the various chemicals, the minimum selling point for H₂ can be negative at low CapEx values, implying that the process reaches break-even point by purely selling chemicals alone. Reforming, on the other hand, operates in a more simplified manner, delivering high H₂ production rates, but the waste anode product CO₂ would decrease the added-value, and require integration with carbon capture and storage infrastructure. At lower levelized costs of renewable electricity, the merit of producing H₂ at low cell voltage may not compensate the input and carbon footprint from sourcing the feedstocks, as in the methanol example given in Section 2.

Considering the fact that noble metal-based catalysts show low C–C bond cleavage but high product selectivity,^[246] while Ni and other earth abundant metals show high capability of cleaving C–C bond in different alcohol oxidation process,^[123] it might be suitable to apply noble metals in partial oxidation processes toward high value chemicals, and Ni and other earth abundant metals in reforming processes for hydrogen generation. This arrangement also matches the market scale of the two different systems, in which hydrogen demand is much higher than the variety of valuable chemicals.

7.1.5. Regional Limitations

Integrating flexible biomass electrolyzers with renewable energy is an ideal approach to effectively store the energy surplus in chemical energy, which could be easily transferred back into power in fuel cells or used as value-added chemicals.^[6,478] How-

ever, the distribution of renewable energy and biomass feedstocks can vary significantly worldwide. In remote areas where feedstocks such as agricultural, bio, and plastic waste are abundant, the availability and cost of low-emission electricity may be constrained. This regional resource imbalance could increase the total cost from feedstock transportation. An effective strategy to prevent long-distance transportation would be to create a local carbon cycle. For example, if the oxidation products cannot be purified and sold, they may find uses as compost, animal feed, building materials, and/or fuel for incineration. This could still generate hydrogen more cost-effectively than water electrolysis, facilitating the local economy and waste recycling.

These remaining challenges should be addressed through research in this field, with a specific focus on the development of photo/electrocatalysts which can withstand the impurities from the feedstocks, whilst simultaneously delivering good selectivity toward value-added products. Some materials are already available,^[44,249] but long-term stability remains unresolved.

7.2. Opportunities in Future Developments

Despite the challenges, biomass electrolysis still constitutes an emerging technology which may foster the development of green H₂ production and sustainable chemical manufacture. Opportunities for future implement have been discussed below.

7.2.1. Membrane-Less Reactor

One large limitation of water electrolysis is the safe operation at low loads and high pressure, due to gas crossover. However, biomass electrolysis only generates H₂ as volatile product, especially under alkaline conditions. Thus, a membrane-less reactor can be employed to largely simplify the operation conditions, reduce the system cost associated with membrane and maintenance, and improve the system efficiency. This concept has been brought up in several alcohol oxidation reports.^[19,23,135,203] In a recent work, Vizza and co-workers designed an autoclave reactor for electrochemical reforming of ethanol with only a cellulose septum to separate the anode and cathode, which could operate at 150 °C for self-pressurized H₂ production.^[261] Later Ruiz-López et al. performed the same electrochemical ethanol reforming in a real membrane-less reactor configuration, which obtained a H₂ stream with 100% Faradaic efficiency at power consumption of 16.9 kWh kg_{H₂}⁻¹.^[263] The presence of organic molecules in the solution has negligible influence to the cathode HER reaction, as demonstrated by the similar overpotential (43 vs 40 mV) and Tafel slope (76 vs 70 mV dec⁻¹).^[203]

7.2.2. Self-Sustainable Production by Coupling with Fuel Cell

The low operation voltage of alcohol electrolysis (requires less than 0.5 V) allows it to be directly coupled with a H₂/O₂ fuel cell (operating at over 0.7 V), with H₂ being the feed for the fuel cell operation, and the electricity generated from the fuel cell in turn powering the electrolyzer process. No H₂ storage

is needed in this scenario, largely reducing the system cost.^[23] This concept is not to be confused with the direct alcohol fuel cell utilizing alcohol as direct feed for electricity. In this scenario, the current density is limited by the sluggish kinetics of alcohol oxidation, while this new concept would allow the coupled fuel cells running at its full capacity. Deng and co-workers proposed a self-powered electrolytic process for glucose to H₂ conversion, in which a glucose-based fuel cell stack provides current and voltage for electrolysis cell, and converts glucose completely into CO₂ with producing H₂ at ultrahigh purity (>99.99 vol%).^[15]

7.2.3. Diversify Biowaste for a Circular Economy

The European Environmental Agency is fostering research toward a “circular economy” with effective waste recycling strategies as a core task.^[479] The end of life commodities should be reused, recycled, and resourced for a better life cycle design.^[25] As mentioned before, urea electrolysis has applications in industries to enable H₂ production from the urea-rich wastewater and animal excrement,^[280] as well as on-demand fuel production for portable applications.^[282] This is a direct and mature example on the utilization of biowaste. Black liquor, an effluent from alkaline pulping of lignocellulosic raw materials in paper industry, has been shown to be a suitable feed solution for electrolytic H₂ production.^[480,481] Lignin oxidation and depolymerization products, such as vanillin and other benzyl alcohols, could also add to the technical and commercial values of the production stream.^[271–273] Hibino et al. demonstrated the possibility of using waste biomass raw materials, such as bread residue, cypress sawdust, rice chaff, and newspapers for H₂ evolution in an electrolysis cell achieving ~100% H₂ at the cathode with a yield of 0.1–0.2 g H₂ per 1 g raw materials used.^[482,483]

7.2.4. Coupling with CO or CO₂ Reduction Reaction Based on the Anode Oxidation Potential

The typical half-cell polarization potentials of different anode oxidation, such as OER, glycerol/glucose electro-oxidation, and cathode reduction reactions including HER, CO reduction, and CO₂ reduction allow designing full cell reaction couplings with minimized energy consumption. For instance, Kenis and co-workers investigated several cathode CO₂ reduction products and anode oxidation reactions (OER, glycerol oxidation, glucose oxidation). The potential of coupling different scenarios have been evaluated in terms of Gibbs free energy and maximum CO₂ emission. Results have shown that even though electroreduction of CO₂ to methanol, C₂H₄ or ethanol on coupled to glucose electro-oxidation is exothermic, the slow kinetics of glycerol oxidation largely limits its usage as anode feed. However, CO₂ reduction to CO coupled with glycerol oxidation delivers the lowest maximum CO₂ emission process, which could indeed become carbon neutral and/or negative from the cradle to the gate.^[484] Similar concept have been also reported with hybrid alcohol oxidation–CO₂ reduction electrolyzer system using molecular electrocatalysts.^[485]

7.2.5. Coupling Two Side Electrosynthesis

To complete the electron economy, apart from electrolysis processes to produce H₂, multi-carbon via HER, CO reduction, and CO₂ reduction, recent research has also focused on coupling two side electrosynthesis processes. Berlinguette and co-workers paired 4-methoxybenzyl alcohol oxidation to 4-methoxybenzaldehyde with 1-hexyne reduction to 1-hexene in an electrochemical cell. A dense Pd membrane was employed to separate the reaction chambers and reduce protons formed at the anode to H atoms for 1-hexyne hydrogenation reaction.^[486] Moeller and co-workers reported the electro-oxidative coupling of alcohols paired with H₂ gas generation, from which H₂ was reused for hydrogenation reactions using Pd/C. Such integrated processes will foster the application of electrosynthesis to more chemical productions needed in the fine chemical industry.^[487]

8. Conclusion

This review summarized several important aspects on electro-, photo-assisted biomass electrolysis for H₂, and value-added chemical production. The major conclusions are as follows:

- Compared to oxygen evolution reaction in water electrolysis, the biomass-derived material oxidation in biomass electrolysis has lower thermodynamic requirements, leading to low ΔE_{eq} and high H₂ production efficiency, however the kinetics are also sluggish due to the multiple electron transfer process.
- Electrocatalyst development needs to fulfill the requirements of high activity, high selectivity, and excellent poison-species tolerance. Reactivity descriptor–CO and OH adsorption energy, as well as the intrinsic properties of metals for different chemical bond activation can provide guidance when choosing the electrocatalysts for tailoring the selectivity to desired products.
- In the case of solar-driven transformations, semiconductors with the right energy band positions and the capability of efficiently activate reactant molecules shall be fabricated. The rational design of semiconductor–cocatalyst systems based on earth abundant elements can lead to high efficiency and selectivity toward a given product.
- Reaction parameters should be carefully chosen in order to achieve optimal operation conditions, in which higher temperature, low feedstock concentration, moderate acidic/alkaline condition, middle potential, short electrode distance, and slow electrolyte flow rate are favored.
- Technoeconomic assessment and life cycle analysis results indicate that the biomass electrolysis processes have the potential to significantly improve the environmental footprint relative to the incumbent production mix, however the overall impact of plant construction, operating patterns, decommissioning on the global warming potential need to be addressed, along with the development of a mature market for the oxidation products.
- The commercialization potential of photochemical, photoelectrochemical, and electrochemical oxidation of biomass is dependent on: a) the creation of a market for low-carbon H₂

and sustainable chemicals which allows effective competition with existing, carbon-intensive, production technologies; b) robust process design and development to scale-up production technology at lower costs; and c) sustainable supply of feedstocks with minimal impacts on the environment. In particular, the oxidation of biomass becomes increasingly cost-competitive to conventional production routes in a carbon-neutral world as greenhouse gas emissions from all economic activities must be avoided or offset.

- The review of technology status indicates that, while many challenges remain in feedstock availability and electrocatalysts and reactor design with high activity, selectivity, stability, and scalability, much progress has also been made, providing opportunities for future optimization and priming this technology for commercial application. With continued research and development, biomass electrolysis coupled with renewable energy could have a substantial impact on the energy transition to a zero-carbon economy.

Supporting Information

Supporting Information is available from the Wiley Online Library or from the author.

Conflict of Interest

The authors declare no conflict of interest.

Keywords

biomass, energy conversion, hydrogen production, life cycle analysis, photo/electrocatalysis, technoeconomical assessments

Received: April 13, 2021

Revised: May 8, 2021

Published online: June 17, 2021

- [1] D. Bogdanov, J. Farfan, K. Sadovskaia, A. Aghahosseini, M. Child, A. Gulagi, A. S. Oyewo, L. de Souza Noel Simas Barbosa, C. Breyer, *Nat. Commun.* **2019**, *10*, 1077.
- [2] J. G. Canadell, E. D. Schulze, *Nat. Commun.* **2014**, *5*, 5282.
- [3] J. Yan, *Nat. Clim. Change* **2018**, *8*, 560.
- [4] J. Rissman, C. Bataille, E. Masanet, N. Aden, W. R. Morrow, N. Zhou, N. Elliott, R. Dell, N. Heeren, B. Huckestein, J. Cresko, S. A. Miller, J. Roy, P. Fennell, B. Cremmins, T. Koch Blank, D. Hone, E. D. Williams, S. de la Rue du Can, B. Sisson, M. Williams, J. Katzenberger, D. Burtraw, G. Sethi, H. Ping, D. Danielson, H. Lu, T. Lorber, J. Dinkel, J. Helseth, *Appl. Energy* **2020**, *266*, 114848.
- [5] P. E. Dodds, A. Velazquez Abad, W. McDowall, G. I. Fox, *Opportunities for hydrogen and fuel cell technologies to contribute to clean growth in the UK*, H₂FC SUPERGEN, London, UK **2020**.
- [6] S. J. Davis, N. S. Lewis, M. Shaner, S. Aggarwal, D. Arent, I. L. Azevedo, S. M. Benson, T. Bradley, J. Brouwer, Y. M. Chiang, C. T. M. Clack, A. Cohen, S. Doig, J. Edmonds, P. Fennell, C. B. Field, B. Hannegan, B. M. Hodge, M. I. Hoffert, E. Ingersoll, P. Jaramillo, K. S. Lackner, K. J. Mach, M. Mastrandrea, J. Ogden, P. F. Peterson, D. L. Sanchez, D. Sperling, J. Stagner, J. E. Trancik, C. J. Yang, K. Caldeira, *Science* **2018**, *360*, 9793.
- [7] I. C. Man, H. Y. Su, F. Calle-Vallejo, H. A. Hansen, J. I. Martínez, N. G. Inoglu, J. Kitchin, T. F. Jaramillo, J. K. Nørskov, J. Rossmeisl, *ChemCatChem* **2011**, *3*, 1159.
- [8] S. Corby, R. R. Rao, L. Steier, J. R. Durrant, unpublished.
- [9] International Energy Agency (IEA), *The Future of Hydrogen-Seizing Today's Opportunities*, IEA, Paris **2019**.
- [10] X. Chen, S. Shen, L. Guo, S. S. Mao, *Chem. Rev.* **2010**, *110*, 6503.
- [11] F. Opoku, K. K. Govender, C. G. C. E. van Sittert, P. P. Govender, *Adv. Sustainable Syst.* **2017**, *1*, 1700006.
- [12] S.-F. Ng, M. Y. L. Lau, W.-J. Ong, *Sol. RRL* **2020**, 2000535.
- [13] Y. Han, Y. Chen, R. Fan, Z. Li, Z. Zou, *EcoMat.* **2021**, *1*.
- [14] K. Ren, K. Wang, Y. Cheng, W. Tang, G. Zhang, *Nano Future* **2020**, *4*, 032006.
- [15] Y. Li, W. Liu, Z. Zhang, X. Du, L. Yu, Y. Deng, *Commun. Chem.* **2019**, *2*, 67.
- [16] C. B. Field, M. J. Behrenfeld, J. T. Randerson, P. Falkowski, *Science* **1998**, *281*, 237.
- [17] V. S. Sikarwar, M. Zhao, P. Clough, J. Yao, X. Zhong, M. Z. Memon, N. Shah, E. J. Anthony, P. S. Fennell, *Energy Environ. Sci.* **2016**, *9*, 2939.
- [18] C. Antonini, K. Treyer, A. Streb, M. van der Spek, C. Bauer, M. Mazzotti, *Sustainable Energy Fuels* **2020**, *4*, 2967.
- [19] K. Zakaria, R. Thimmappa, M. Mamlouk, K. Scott, *Int. J. Hydrogen Energy* **2020**, *45*, 8107.
- [20] Y. X. Chen, A. Lavacchi, H. A. Miller, M. Bevilacqua, J. Filippi, M. Innocenti, A. Marchionni, W. Oberhauser, L. Wang, F. Vizza, *Nat. Commun.* **2014**, *5*, 4036.
- [21] S. Uhm, H. Jeon, T. J. Kim, J. Lee, *J. Power Sources* **2012**, *198*, 218.
- [22] C. Lamy, T. Jaubert, S. Baranton, C. Coutanceau, *J. Power Sources* **2014**, *245*, 927.
- [23] V. Bambagioni, M. Bevilacqua, C. Bianchini, J. Filippi, A. Lavacchi, A. Marchionni, F. Vizza, P. K. Shen, *ChemSusChem* **2010**, *3*, 851.
- [24] P. De Luna, C. Hahn, D. Higgins, S. A. Jaffer, T. F. Jaramillo, E. H. Sargent, *Science* **2019**, *364*, 350.
- [25] J. B. Zimmerman, P. T. Anastas, H. C. Erythropel, W. Leitner, *Science* **2020**, *367*, 397.
- [26] Y. Kwon, K. J. P. Schouten, M. T. M. Koper, *ChemCatChem* **2011**, *3*, 1176.
- [27] J. F. Gomes, G. Tremiliosi-Filho, *Electrocatalysis* **2011**, *2*, 96.
- [28] B. Garlyyev, S. Xue, J. Fichtner, A. S. Bandarenka, C. Andronescu, *ChemSusChem* **2020**, *13*, 2513.
- [29] K. Li, Y. Sun, *Chem. - Eur. J.* **2018**, *24*, 18258.
- [30] M. Li, X. Deng, K. Xiang, Y. Liang, B. Zhao, J. Hao, J. L. Luo, X. Z. Fu, *ChemSusChem* **2020**, *13*, 914.
- [31] IRENA, *Hydrogen: A Renewable Energy Perspective—Report Prepared for the 2nd Hydrogen Energy Ministerial Meeting in Tokyo, Japan*, IRENA, Abu Dhabi **2019**.
- [32] A. T. Pham, T. Baba, T. Shudo, *Int. J. Hydrogen Energy* **2013**, *38*, 9945.
- [33] M. Bellini, M. Bevilacqua, M. Innocenti, A. Lavacchi, H. A. Miller, J. Filippi, A. Marchionni, W. Oberhauser, L. Wang, F. Vizza, *J. Electrochem. Soc.* **2014**, *161*, D3032.
- [34] H. A. Miller, M. Bellini, F. Vizza, C. Hasenöhrl, R. D. Tilley, *Catal. Sci. Technol.* **2016**, *6*, 6870.
- [35] M. A. J. Huijbregts, Z. J. N. Steinmann, P. M. F. Elshout, G. Stam, F. Veronesi, M. Vieira, M. Zipp, A. Hollander, R. van Zelm, *Int. J. Life Cycle Assess.* **2017**, *22*, 138.
- [36] R. Bhandari, C. A. Trudewind, P. Zapp, *J. Cleaner Prod.* **2014**, *85*, 151.
- [37] R. Sirisangawang, P. Samaikaw, B. Chotiviriyavanich, P. Kitchaiya, *IOP Conf. Ser.: Mater. Sci. Eng.* **2019**, *639*, 012052.
- [38] V. Hřbová, K. Melzoch, M. Rychtera, B. Sekavová, *Desalination* **2004**, *162*, 361.
- [39] M. Simões, S. Baranton, C. Coutanceau, *ChemSusChem* **2012**, *5*, 2106.

- [40] H. J. Kim, J. Lee, S. K. Green, G. W. Huber, W. B. Kim, *ChemSusChem* **2014**, 7, 1051.
- [41] M. A. Laguna-Bercero, *J. Power Sources* **2012**, 203, 4.
- [42] B. K. Boggs, R. L. King, G. G. Botte, *Chem. Commun.* **2009**, 4859.
- [43] H. J. Kim, Y. Kim, D. Lee, J. R. Kim, H. J. Chae, S. Y. Jeong, B. S. Kim, J. Lee, G. W. Huber, J. Byun, S. Kim, J. Han, *ACS Sustainable Chem. Eng.* **2017**, 5, 6626.
- [44] M. S. E. Houache, K. Hughes, E. A. Baranova, *Sustainable Energy Fuels* **2019**, 3, 1892.
- [45] C. Lamy, C. Coutanceau, S. Baranton, *Production of Clean Hydrogen by Electrochemical Reforming of Oxygenated Organic Compounds*, Academic Press, Cambridge, Massachusetts **2020**, pp. 7–20.
- [46] A. Buttler, H. Spliethoff, *Renewable Sustainable Energy Rev.* **2018**, 82, 2440.
- [47] W. Tong, M. Forster, F. Dionigi, S. Dresp, R. Sadeghi Erami, P. Strasser, A. J. Cowan, P. Farràs, *Nat. Energy* **2020**, 5, 367.
- [48] M. Carmo, D. L. Fritz, J. Mergel, D. Stolten, *Int. J. Hydrogen Energy* **2013**, 38, 4901.
- [49] D. Zhang, J. Z. Soo, H. H. Tan, C. Jagadish, K. Catchpole, S. K. Karuturi, *Adv. Energy Sustainable Res.* **2021**, 2, 2000071.
- [50] W. J. Liu, Z. Xu, D. Zhao, X. Q. Pan, H. C. Li, X. Hu, Z. Y. Fan, W. K. Wang, G. H. Zhao, S. Jin, G. W. Huber, H. Q. Yu, *Nat. Commun.* **2020**, 11, 265.
- [51] M. S. Faber, S. Jin, *Energy Environ. Sci.* **2014**, 7, 3519.
- [52] N. Elgrishi, K. J. Rountree, B. D. McCarthy, E. S. Rountree, T. T. Eisenhart, J. L. Dempsey, *J. Chem. Educ.* **2018**, 95, 197.
- [53] I. Roger, M. A. Shipman, M. D. Symes, *Nat. Rev. Chem.* **2017**, 1, 0003.
- [54] S. Anantharaj, S. R. Ede, K. Sakthikumar, K. Karthick, S. Mishra, S. Kundu, *ACS Catal.* **2016**, 6, 8069.
- [55] J. N. Tiwari, A. N. Singh, S. Sultan, K. S. Kim, *Adv. Energy Mater.* **2020**, 10, 2000280.
- [56] P. Kuang, M. Sayed, J. Fan, B. Cheng, J. Yu, *Adv. Energy Mater.* **2020**, 10, 1903802.
- [57] I. E. L. Stephens, I. Chorkendorff, *Angew. Chem., Int. Ed.* **2011**, 50, 1476.
- [58] C. Wei, R. R. Rao, J. Peng, B. Huang, I. E. L. Stephens, M. Risch, Z. J. Xu, Y. Shao-Horn, *Adv. Mater.* **2019**, 31, 1816296.
- [59] A. B. Jorge, R. Jervis, A. P. Periasamy, M. Qiao, J. Feng, L. N. Tran, M. M. Titirici, *Adv. Energy Mater.* **2020**, 10, 1902494.
- [60] Y. Kwon, M. T. M. Koper, *Anal. Chem.* **2010**, 82, 5420.
- [61] A. Falase, K. Garcia, C. Lau, P. Atanassov, *Electrochem. Commun.* **2011**, 13, 1488.
- [62] S. C. Chang, Y. Ho, M. J. Weaver, *J. Am. Chem. Soc.* **1991**, 113, 9506.
- [63] J. Schnaidt, M. Heinen, D. Denot, Z. Jusys, R. Jürgen Behm, *J. Electroanal. Chem.* **2011**, 661, 250.
- [64] L. Thia, M. Xie, Z. Liu, X. Ge, Y. Lu, W. E. Fong, X. Wang, *ChemCatChem* **2016**, 8, 3272.
- [65] M. T. M. Koper, *Chem. Sci.* **2013**, 4, 2710.
- [66] S. Gilman, *J. Phys. Chem.* **1964**, 68, 70.
- [67] A. Baz, A. Holewinski, *J. Catal.* **2020**, 384, 1.
- [68] M. T. M. Koper, N. P. Lebedeva, C. G. M. Hermse, *Faraday Discuss.* **2002**, 121, 301.
- [69] P. Liu, A. Logadottir, J. K. Nørskov, *Electrochim. Acta* **2003**, 48, 3731.
- [70] J. K. Nørskov, *Angew. Chem.* **2008**, 120, 4913.
- [71] A. S. Bandarenka, A. S. Varela, M. Karamad, F. Calle-Vallejo, L. Bech, F. J. Perez-Alonso, J. Rossmeisl, I. E. L. Stephens, I. Chorkendorff, *Angew. Chem., Int. Ed.* **2012**, 51, 11845.
- [72] T. Yajima, H. Uchida, M. Watanabe, *J. Phys. Chem. B* **2004**, 108, 2654.
- [73] Y. Kim, H. W. Kim, S. Lee, J. Han, D. Lee, J. R. Kim, T. W. Kim, C. U. Kim, S. Y. Jeong, H. J. Chae, B. S. Kim, H. Chang, W. B. Kim, S. M. Choi, H. J. Kim, *ChemCatChem* **2017**, 9, 1683.
- [74] P. Ferrin, A. U. Nilekar, J. Greeley, M. Mavrikakis, J. Rossmeisl, *Surf. Sci.* **2008**, 602, 3424.
- [75] P. Ferrin, M. Mavrikakis, *J. Am. Chem. Soc.* **2009**, 131, 14381.
- [76] G. A. Tritsarlis, J. Rossmeisl, *J. Phys. Chem. C* **2012**, 116, 11980.
- [77] D. J. Chen, Y. J. Tong, *Angew. Chem., Int. Ed.* **2015**, 54, 9394.
- [78] B. Hammer, Y. Morikawa, J. K. Nørskov, *Phys. Rev. Lett.* **1996**, 76, 2141.
- [79] F. Maroun, F. Ozanam, O. M. Magnussen, R. J. Behm, *Science* **2001**, 293, 1811.
- [80] T. H. M. Housmans, A. H. Wonders, M. T. M. Koper, *J. Phys. Chem. B* **2006**, 110, 10021.
- [81] H. A. Gasteiger, N. Marković, P. N. Ross, E. J. Cairns, *J. Phys. Chem.* **1993**, 97, 12020.
- [82] J. Kua, W. A. Goddard, *J. Am. Chem. Soc.* **1999**, 121, 10928.
- [83] S. Wasmus, A. Küver, *J. Electroanal. Chem.* **1999**, 461, 14.
- [84] J. Rossmeisl, P. Ferrin, G. A. Tritsarlis, A. U. Nilekar, S. Koh, S. E. Bae, S. R. Brankovic, P. Strasser, M. Mavrikakis, *Energy Environ. Sci.* **2012**, 5, 8335.
- [85] L. Zhang, K. Doyle-Davis, X. Sun, *Energy Environ. Sci.* **2019**, 12, 492.
- [86] C. Mondelli, G. Gözaydın, N. Yan, J. Pérez-Ramírez, *Chem. Soc. Rev.* **2020**, 49, 3764.
- [87] S. Nitopi, E. Bertheussen, S. B. Scott, X. Liu, A. K. Engstfeld, S. Horch, B. Seger, I. E. L. Stephens, K. Chan, C. Hahn, J. K. Nørskov, T. F. Jaramillo, I. Chorkendorff, *Chem. Rev.* **2019**, 119, 7610.
- [88] M. Mavrikakis, B. Hammer, J. K. Nørskov, *Phys. Rev. Lett.* **1998**, 81, 2819.
- [89] T. Bligaard, J. K. Nørskov, *Electrochim. Acta* **2007**, 52, 5512.
- [90] A. Ruban, B. Hammer, P. Stoltze, H. L. Skriver, J. K. Nørskov, *J. Mol. Catal. A: Chem.* **1997**, 115, 421.
- [91] J. R. Kitchin, J. K. Nørskov, M. A. Barteau, J. G. Chen, *Phys. Rev. Lett.* **2004**, 93, 4.
- [92] M. M. D. Baker, G. I. Jenkins, in *Fundamental Concepts in Heterogeneous Catalysis* (Ed: J. K. Nørskov) John Wiley & Sons, Ltd, New Jersey **2014**, pp. 114–137.
- [93] M. T. Tang, Z. W. Ulissi, K. Chan, *J. Phys. Chem. C* **2018**, 122, 14481.
- [94] A. Cuesta, *J. Am. Chem. Soc.* **2006**, 128, 13332.
- [95] M. Neurock, M. Janik, A. Wieckowski, *Faraday Discuss.* **2008**, 140, 363.
- [96] M. J. Janik, C. D. Taylor, M. Neurock, *Top. Catal.* **2007**, 46, 306.
- [97] M. T. M. Koper, S. C. S. Lai, E. Herrero, *Fuel Cell Catalysis: A Surface Science Approach*, Wiley **2008**, pp. 159–207.
- [98] E. Herrero, K. Franaszczuk, A. Wieckowski, *J. Phys. Chem.* **1994**, 98, 5074.
- [99] Y. Kwon, S. C. S. Lai, P. Rodriguez, M. T. M. Koper, *J. Am. Chem. Soc.* **2011**, 133, 6914.
- [100] S. Ringe, C. G. Morales-Guio, L. D. Chen, M. Fields, T. F. Jaramillo, C. Hahn, K. Chan, *Nat. Commun.* **2020**, 11, 33.
- [101] K. Chan, *Nat. Commun.* **2020**, 11, 5954.
- [102] X. Liu, P. Schlexer, J. Xiao, Y. Ji, L. Wang, R. B. Sandberg, M. Tang, K. S. Brown, H. Peng, S. Ringe, C. Hahn, T. F. Jaramillo, J. K. Nørskov, K. Chan, *Nat. Commun.* **2019**, 10, 32.
- [103] S. Vijay, J. A. Gauthier, H. H. Heenen, V. J. Bukas, H. H. Kristoffersen, K. Chan, *ACS Catal.* **2020**, 10, 7826.
- [104] R. B. Sandberg, J. H. Montoya, K. Chan, J. K. Nørskov, *Surf. Sci.* **2016**, 654, 56.
- [105] J. Resasco, L. D. Chen, E. Clark, C. Tsai, C. Hahn, T. F. Jaramillo, K. Chan, A. T. Bell, *J. Am. Chem. Soc.* **2017**, 139, 11277.
- [106] L. D. Chen, M. Urushihara, K. Chan, J. K. Nørskov, *ACS Catal.* **2016**, 6, 7133.
- [107] P. P. Lopes, D. Strmcnik, J. S. Jirkovsky, J. G. Connell, V. Stamenkovic, N. Markovic, *Catal. Today* **2016**, 262, 41.
- [108] D. Strmcnik, K. Kodama, D. Van Der Vliet, J. Greeley, V. R. Stamenkovic, N. M. Marković, *Nat. Chem.* **2009**, 1, 466.
- [109] C. A. Angelucci, H. Varela, G. Tremiliosi-Filho, J. F. Gomes, *Electrochem. Commun.* **2013**, 33, 10.
- [110] D. Hiltrop, S. Cychy, K. Elumeeva, W. Schuhmann, M. Muhler, *Beilstein J. Org. Chem.* **2018**, 14, 1428.

- [111] L. Jacobse, S. O. Vink, S. Wijngaarden, L. B. F. Juurlink, *J. Chem. Educ.* **2017**, *94*, 1285.
- [112] M. T. M. Koper, *J. Electroanal. Chem.* **2011**, *660*, 254.
- [113] M. T. M. Koper, *Top. Catal.* **2015**, *58*, 1153.
- [114] J. Joo, T. Uchida, A. Cuesta, M. T. M. Koper, M. Osawa, *J. Am. Chem. Soc.* **2013**, *135*, 9991.
- [115] P. Rodriguez, Y. Kwon, M. T. M. Koper, *Nat. Chem.* **2012**, *4*, 177.
- [116] I. T. Schwartz, A. P. Jonke, M. Josowicz, J. Janata, *Catal. Lett.* **2013**, *143*, 777.
- [117] G. A. B. Mello, C. Busó-Rogero, E. Herrero, J. M. Feliu, *J. Chem. Phys.* **2018**, *150*, 041703.
- [118] H. Hitmi, E. M. Belgsir, J.-M. Léger, C. Lamy, R. O. Lezna, *Electrochim. Acta* **1994**, *39*, 407.
- [119] L. Roquet, E. M. Belgsir, J. M. Léger, C. Lamy, *Electrochim. Acta* **1994**, *39*, 2387.
- [120] P. S. Fernández, M. E. Martins, G. A. Camara, *Electrochim. Acta* **2012**, *66*, 180.
- [121] J. F. Gomes, C. A. Martins, M. J. Giz, G. Tremiliosi-Filho, G. A. Camara, *J. Catal.* **2013**, *307*, 154.
- [122] S. H. Shi, Y. Liang, N. Jiao, *Chem. Rev.* **2021**, *121*, 485.
- [123] T. Li, D. Harrington, *ChemSusChem* **2021**, *14*, 1472.
- [124] S. Shi-Gang, L. Yan, L. Nan-Hai, M. Ji-Qian, *J. Electroanal. Chem.* **1994**, *370*, 273.
- [125] A. C. Garcia, M. J. Kolb, C. Van Nierop Y Sanchez, J. Vos, Y. Y. Birdja, Y. Kwon, G. Tremiliosi-Filho, M. T. M. Koper, *ACS Catal.* **2016**, *6*, 4491.
- [126] P. S. Fernández, C. A. Martins, M. E. Martins, G. A. Camara, *Electrochim. Acta* **2013**, *112*, 686.
- [127] P. S. Fernández, M. E. Martins, C. A. Martins, G. A. Camara, *Electrochem. Commun.* **2012**, *15*, 14.
- [128] M. T. Bender, X. Yuan, K. S. Choi, *Nat. Commun.* **2020**, *11*, 4594.
- [129] S. E. Davis, M. S. Ide, R. J. Davis, *Green Chem.* **2013**, *15*, 17.
- [130] R. Konaka, S. Terabe, K. Kuruma, *J. Org. Chem.* **1969**, *34*, 1334.
- [131] M. Fleischmann, K. Korinek, D. Pletcher, *J. Chem. Soc., Perkin Trans.* **1972**, *2*, 1396.
- [132] M. Fleischmann, K. Korinek, D. Pletcher, *J. Electroanal. Chem. Interfacial Electrochem.* **1971**, *31*, 39.
- [133] M. S. E. Houache, K. Hughes, A. Ahmed, R. Safari, H. Liu, G. A. Botton, E. A. Baranova, *ACS Sustainable Chem. Eng.* **2019**, *7*, 14425.
- [134] B. J. Taitt, D. H. Nam, K. S. Choi, *ACS Catal.* **2019**, *9*, 660.
- [135] X. Han, H. Sheng, C. Yu, T. W. Walker, G. W. Huber, J. Qiu, S. Jin, *ACS Catal.* **2020**, *10*, 6741.
- [136] Z. Zhang, L. Xin, W. Li, *Appl. Catal., B* **2012**, *119–120*, 40.
- [137] B. Liu, J. Greeley, *Phys. Chem. Chem. Phys.* **2013**, *15*, 6475.
- [138] B. Liu, J. Greeley, *J. Phys. Chem. C* **2011**, *115*, 19702.
- [139] D. Lee, Y. Kim, Y. Kwon, J. Lee, T. W. Kim, Y. Noh, W. B. Kim, M. H. Seo, K. Kim, H. J. Kim, *Appl. Catal., B* **2019**, *245*, 555.
- [140] Z. Chen, C. Liu, X. Zhao, H. Yan, J. Li, P. Lyu, Y. Du, S. Xi, K. Chi, X. Chi, H. Xu, X. Li, W. Fu, K. Leng, S. J. Pennycook, S. Wang, K. P. Loh, *Adv. Mater.* **2019**, *31*, 1804763.
- [141] V. Bambagioni, C. Bianchini, A. Marchionni, J. Filippi, F. Vizza, J. Teddy, P. Serp, M. Zhiani, *J. Power Sources* **2009**, *190*, 241.
- [142] H. Wang, L. Thia, N. Li, X. Ge, Z. Liu, X. Wang, *ACS Catal.* **2015**, *5*, 3174.
- [143] A. Nakova, M. Ilieva, T. Boijadjieva-Scherzer, V. Tsakova, *Electrochim. Acta* **2019**, *306*, 643.
- [144] A. Villa, N. Dimitratos, C. E. Chan-Thaw, C. Hammond, L. Prati, G. J. Hutchings, *Acc. Chem. Res.* **2015**, *48*, 1403.
- [145] S. Carrettin, P. McMorn, P. Johnston, K. Griffin, C. J. Kiely, G. A. Attard, G. J. Hutchings, *Top. Catal.* **2004**, *27*, 131.
- [146] S. Carrettin, P. McMorn, P. Johnston, K. Griffin, C. J. Kiely, G. J. Hutchings, *Phys. Chem. Chem. Phys.* **2003**, *5*, 1329.
- [147] W. C. Ketchie, M. Murayama, R. J. Davis, *Top. Catal.* **2007**, *44*, 307.
- [148] H. J. Kim, S. M. Choi, M. H. Seo, S. Green, G. W. Huber, W. B. Kim, *Electrochem. Commun.* **2011**, *13*, 890.
- [149] M. Zhao, Z. Lyu, M. Xie, Z. D. Hood, Z. Cao, M. Chi, Y. Xia, *Small Methods* **2020**, *1900843*, 1.
- [150] S. Dash, N. Munichandraiah, *Electrochim. Acta* **2015**, *180*, 339.
- [151] R. S. Ferreira, M. Janete Giz, G. A. Camara, *J. Electroanal. Chem.* **2013**, *697*, 15.
- [152] W. Hong, C. Shang, J. Wang, E. Wang, *Energy Environ. Sci.* **2015**, *8*, 2910.
- [153] C. Bianchini, P. K. Shen, *Chem. Rev.* **2009**, *109*, 4183.
- [154] R. Boukil, N. Tuleushova, D. Cot, B. Rebiere, V. Bonniol, J. Cambedouzou, S. Tingry, D. Cornu, Y. Holade, *J. Mater. Chem. A* **2020**, *8*, 8848.
- [155] Y. Zhou, Y. Shen, J. Xi, X. Luo, *ACS Appl. Mater. Interfaces* **2019**, *11*, 28953.
- [156] J. R. Kitchin, J. K. Nørskov, M. A. Barteau, J. G. Chen, *J. Chem. Phys.* **2004**, *120*, 10240.
- [157] X. Tian, X. Zhao, Y. Q. Su, L. Wang, H. Wang, D. Dang, B. Chi, H. Liu, E. J. M. Hensen, X. W. Lou, B. Y. Xia, *Science* **2019**, *366*, 850.
- [158] P. Song, H. Xu, J. Wang, Y. Zhang, F. Gao, J. Guo, Y. Shiraishi, Y. Du, *Nanoscale* **2018**, *10*, 16468.
- [159] H. Xu, J. Wei, M. Zhang, C. Wang, Y. Shiraishi, J. Guo, Y. Du, *J. Mater. Chem. A* **2018**, *6*, 24418.
- [160] Y. Zhang, F. Gao, P. Song, J. Wang, T. Song, C. Wang, C. Chen, L. Jin, L. Li, X. Zhu, Y. Du, *J. Power Sources* **2019**, *425*, 179.
- [161] T. Song, F. Gao, Y. Zhang, C. Chen, C. Wang, S. Li, H. Shang, Y. Du, *Nanoscale* **2020**, *12*, 9842.
- [162] A. J. Wang, X. F. Zhang, L. Y. Jiang, L. Zhang, J. J. Feng, *Chem-CatChem* **2018**, *10*, 3319.
- [163] Y. Holade, C. Morais, K. Servat, T. W. Napporn, K. B. Kokoh, *ACS Catal.* **2013**, *3*, 2403.
- [164] M. T. M. Koper, *Nanoscale* **2011**, *3*, 2054.
- [165] R. G. Da Silva, S. Aquino Neto, K. B. Kokoh, A. R. De Andrade, *J. Power Sources* **2017**, *351*, 174.
- [166] J. Baltrusaitis, M. Valter, A. Hellman, *J. Phys. Chem. C* **2016**, *120*, 1749.
- [167] X. Zhu, Q. Guo, Y. Sun, S. Chen, J. Q. Wang, M. Wu, W. Fu, Y. Tang, X. Duan, D. Chen, Y. Wan, *Nat. Commun.* **2019**, *10*, 1428.
- [168] B. T. X. Lam, M. Chiku, E. Higuchi, H. Inoue, *J. Power Sources* **2015**, *297*, 149.
- [169] I. Velázquez-Hernández, E. Zamudio, F. J. Rodríguez-Valadez, N. A. García-Gómez, L. Álvarez-Contreras, M. Guerra-Balcázar, N. Arjona, *Fuel* **2020**, *262*, 116556.
- [170] H. Xu, B. Yan, K. Zhang, J. Wang, S. Li, C. Wang, Y. Shiraishi, Y. Du, P. Yang, *Electrochim. Acta* **2017**, *245*, 227.
- [171] M. Mougnot, A. Caillard, M. Simoes, S. Baranton, C. Coutanceau, P. Brault, *Appl. Catal., B* **2011**, *107*, 372.
- [172] A. N. Gerales, D. F. Da Silva, L. G. D. A. E. Silva, E. V. Spinacé, A. O. Neto, M. C. Dos Santos, *J. Power Sources* **2015**, *293*, 823.
- [173] K. Cai, Y. Liao, H. Zhang, J. Liu, Z. Lu, Z. Huang, S. Chen, H. Han, *ACS Appl. Mater. Interfaces* **2016**, *8*, 12792.
- [174] F. A. Al-Odail, A. Anastasopoulos, B. E. Hayden, *Phys. Chem. Chem. Phys.* **2010**, *12*, 11398.
- [175] Y. Suo, I.-M. Hsing, *Electrochim. Acta* **2011**, *56*, 2174.
- [176] H. C. Ham, G. S. Hwang, J. Han, S. W. Nam, T. H. Lim, *J. Phys. Chem. C* **2010**, *114*, 14922.
- [177] S. Li, J. Lai, R. Luque, G. Xu, *Energy Environ. Sci.* **2016**, *9*, 3097.
- [178] F. Yang, J. Y. Ye, Q. Yuan, X. Yang, Z. Xie, F. Zhao, Z. Zhou, L. Gu, X. Wang, *Adv. Funct. Mater.* **2020**, *30*, 1908235.
- [179] A. Zalineeva, A. Serov, M. Padilla, U. Martinez, K. Artyushkova, S. Baranton, C. Coutanceau, P. B. Atanassov, *J. Am. Chem. Soc.* **2014**, *136*, 3937.
- [180] O. O. Fashedemi, H. A. Miller, A. Marchionni, F. Vizza, K. I. Ozoemena, *J. Mater. Chem. A* **2015**, *3*, 7145.
- [181] J. Lai, F. Lin, Y. Tang, P. Zhou, Y. Chao, Y. Zhang, S. Guo, *Adv. Energy Mater.* **2019**, *9*, 1800684.
- [182] H. Xu, B. Yan, J. Wang, K. Zhang, S. Li, Z. Xiong, C. Wang, Y. Shiraishi, Y. Du, P. Yang, *J. Mater. Chem. A* **2017**, *5*, 15932.

- [183] H. Wang, L. Thia, N. Li, X. Ge, Z. Liu, X. Wang, *Appl. Catal., B* **2015**, 166–167, 25.
- [184] A. Falase, M. Main, K. Garcia, A. Serov, C. Lau, P. Atanassov, *Electrochim. Acta* **2012**, 66, 295.
- [185] J. Tzadikov, M. Amsellem, H. Amlani, J. Barrio, A. Azoulay, M. Volokh, S. Kozuch, M. Shalom, *Angew. Chem., Int. Ed.* **2019**, 58, 14964.
- [186] Y. Zhou, Y. Shen, J. Xi, *Appl. Catal., B* **2019**, 245, 604.
- [187] N. Zhang, Y. Feng, X. Zhu, S. Guo, J. Guo, X. Huang, *Adv. Mater.* **2017**, 29, 1603374.
- [188] H. J. Kim, S. M. Choi, S. Green, G. A. Tompsett, S. H. Lee, G. W. Huber, W. B. Kim, *Appl. Catal., B* **2011**, 101, 366.
- [189] H. Kimura, K. Tsuto, T. Wakisaka, Y. Kazumi, Y. Inaya, *Appl. Catal., A* **1993**, 96, 217.
- [190] H. Kimura, *Appl. Catal., A* **1993**, 105, 147.
- [191] A. Zalineeva, S. Baranton, C. Coutanceau, *Electrochim. Acta* **2015**, 176, 705.
- [192] G. L. Caneppele, T. S. Almeida, C. R. Zanata, É. Teixeira-Neto, P. S. Fernández, G. A. Camara, C. A. Martins, *Appl. Catal., B* **2017**, 200, 114.
- [193] M. B. C. De Souza, R. A. Vicente, V. Y. Yukuhiro, C. T. G. Pires, W. Cheuquepán, J. L. Bott-Neto, J. Solla-Gullón, P. S. Fernández, *ACS Catal.* **2019**, 9, 5104.
- [194] Y. Kwon, Y. Birdja, I. Spanos, P. Rodriguez, M. T. M. Koper, *ACS Catal.* **2012**, 2, 759.
- [195] A. C. Garcia, Y. Y. Birdja, G. Tremiliosi-Filho, M. T. M. Koper, *J. Catal.* **2017**, 346, 117.
- [196] S. Feng, J. Yi, H. Miura, N. Nakatani, M. Hada, T. Shishido, *ACS Catal.* **2020**, 10, 6071.
- [197] Y. Kwon, T. J. P. Hersbach, M. T. M. Koper, *Top. Catal.* **2014**, 57, 1272.
- [198] M. B. C. De Souza, V. Y. Yukuhiro, R. A. Vicente, C. T. G. Vilela Menegaz Teixeira Pires, J. L. Bott-Neto, P. S. Fernández, *ACS Catal.* **2020**, 10, 2131.
- [199] C. A. Martins, O. A. Ibrahim, P. Pei, E. Kjeang, *Electrochim. Acta* **2019**, 305, 47.
- [200] Z. Li, G. Qiu, Z. Jiang, W. Zhuang, J. Wu, X. Du, *Int. J. Hydrogen Energy* **2018**, 43, 22538.
- [201] M. C. Figueiredo, O. Sorsa, N. Doan, E. Pohjalainen, H. Hildebrand, P. Schmuki, B. P. Wilson, T. Kallio, *J. Power Sources* **2015**, 275, 341.
- [202] J. L. Bott-Neto, T. S. Martins, S. A. S. Machado, E. A. Ticianelli, *ACS Appl. Mater. Interfaces* **2019**, 11, 30810.
- [203] Y. Li, X. Wei, L. Chen, J. Shi, M. He, *Nat. Commun.* **2019**, 10, 5335.
- [204] M. A. Abdel Rahim, H. B. Hassan, R. M. Abdel Hamid, *J. Power Sources* **2006**, 154, 59.
- [205] M. Asgari, M. G. Maragheh, R. Davarkhah, E. Lohrasbi, A. N. Golikand, *Electrochim. Acta* **2012**, 59, 284.
- [206] M. A. Abdel Rahim, R. M. Abdel Hameed, M. W. Khalil, *J. Power Sources* **2004**, 134, 160.
- [207] V. L. Oliveira, C. Morais, K. Servat, T. W. Napporn, G. Tremiliosi-Filho, K. B. Kokoh, *J. Electroanal. Chem.* **2013**, 703, 56.
- [208] M. S. E. Houache, K. Hughes, R. Safari, G. A. Botton, E. A. Baranova, *ACS Appl. Mater. Interfaces* **2020**, 12, 15095.
- [209] M. S. E. Houache, E. Cossar, S. Ntais, E. A. Baranova, *J. Power Sources* **2018**, 375, 310.
- [210] F. Dionigi, Z. Zeng, I. Sinev, T. Merzdorf, S. Deshpande, M. B. Lopez, S. Kunze, I. Zegkinoglou, H. Sarodnik, D. Fan, A. Bergmann, J. Drnc, J. F. de Araujo, M. Gliech, D. Teschner, J. Zhu, W. X. Li, J. Greeley, B. R. Cuenya, P. Strasser, *Nat. Commun.* **2020**, 11, 2522.
- [211] S. Sun, L. Sun, S. Xi, Y. Du, M. U. Anu Prathap, Z. Wang, Q. Zhang, A. Fisher, Z. J. Xu, *Electrochim. Acta* **2017**, 228, 183.
- [212] P. N. Amaniampong, Q. T. Trinh, J. J. Varghese, R. Behling, S. Valange, S. H. Mushrif, F. Jérôme, *Green Chem.* **2018**, 20, 2730.
- [213] C. Liu, M. Hirohara, T. Maekawa, R. Chang, T. Hayashi, C. Y. Chiang, *Appl. Catal., B* **2020**, 265, 118543.
- [214] C. H. Lam, A. J. Bloomfield, P. T. Anastas, *Green Chem.* **2017**, 19, 1958.
- [215] A. Brouzgou, P. Tsiakaras, *Top. Catal.* **2015**, 58, 1311.
- [216] P. Zhang, Y. J. Guo, J. Chen, Y. R. Zhao, J. Chang, H. Junge, M. Beller, Y. Li, *Nat. Catal.* **2018**, 1, 332.
- [217] G. Moggia, T. Kenis, N. Daems, T. Breugelmans, *ChemElectroChem* **2020**, 2019, 86.
- [218] D. Zheng, J. Li, S. Ci, P. Cai, Y. Ding, M. Zhang, Z. Wen, *Appl. Catal., B* **2020**, 277, 119178.
- [219] T. Rafaïdeen, S. Baranton, C. Coutanceau, *Appl. Catal., B* **2019**, 243, 641.
- [220] A. J. J. E. Eerhart, A. P. C. Faaij, M. K. Patel, *Energy Environ. Sci.* **2012**, 5, 6407.
- [221] B. You, N. Jiang, X. Liu, Y. Sun, *Angew. Chem., Int. Ed.* **2016**, 55, 9913.
- [222] S. N. Boride, S. Barwe, J. Weidner, S. Cychy, D. M. Morales, S. Dieckhöfer, D. Hiltrop, J. Masa, M. Muhler, W. Schuhmann, *Angew. Chem., Int. Ed.* **2018**, 57, 11460.
- [223] D. H. Nam, B. J. Taitt, K. S. Choi, *ACS Catal.* **2018**, 8, 1197.
- [224] W. J. Liu, L. Dang, Z. Xu, H. Q. Yu, S. Jin, G. W. Huber, *ACS Catal.* **2018**, 8, 5533.
- [225] Z. Zhou, C. Chen, M. Gao, B. Xia, J. Zhang, *Green Chem.* **2019**, 21, 6699.
- [226] B. You, X. Liu, N. Jiang, Y. Sun, *J. Am. Chem. Soc.* **2016**, 138, 13639.
- [227] N. Jiang, B. You, R. Boonstra, I. M. Terrero Rodriguez, Y. Sun, *ACS Energy Lett.* **2016**, 1, 386.
- [228] L. Gao, Z. Liu, J. Ma, L. Zhong, Z. Song, J. Xu, S. Gan, D. Han, L. Niu, *Appl. Catal., B* **2020**, 267, 118235.
- [229] M. Sajid, X. Zhao, D. Liu, *Green Chem.* **2018**, 20, 5427.
- [230] G. Grabowski, J. Lewkowski, R. Skowroński, *Electrochim. Acta* **1991**, 36, 1995.
- [231] D. J. Chadderdon, L. Xin, J. Qi, Y. Qiu, P. Krishna, K. L. More, W. Li, *Green Chem.* **2014**, 16, 3778.
- [232] H. Ait Rass, N. Essayem, M. Besson, *ChemSusChem* **2015**, 8, 1206.
- [233] S. R. Kubota, K. Choi, *ChemSusChem* **2018**, 11, 2138.
- [234] L. Gao, Y. Bao, S. Gan, Z. Sun, Z. Song, D. Han, F. Li, L. Niu, *ChemSusChem* **2018**, 11, 2547.
- [235] C. Andronescu, S. Seisel, P. Wilde, S. Barwe, J. Masa, Y.-T. Chen, E. Ventosa, W. Schuhmann, *Chem. - Eur. J.* **2018**, 24, 13773.
- [236] S. Barwe, J. Weidner, S. Cychy, D. M. Morales, S. Dieckhöfer, D. Hiltrop, J. Masa, M. Muhler, W. Schuhmann, *Angew. Chem., Int. Ed.* **2018**, 57, 11460.
- [237] G. Chen, H. Wan, W. Ma, N. Zhang, Y. Cao, X. Liu, J. Wang, R. Ma, *Adv. Energy Mater.* **2020**, 10, 1902535.
- [238] G. A. Olah, *Angew. Chem., Int. Ed.* **2005**, 44, 2636.
- [239] Z. Hu, M. Wu, Z. Wei, S. Song, P. K. Shen, *J. Power Sources* **2007**, 166, 458.
- [240] T. Take, K. Tsurutani, M. Umeda, *J. Power Sources* **2007**, 164, 9.
- [241] Z. Zhao, X. Huang, M. Li, G. Wang, C. Lee, E. Zhu, X. Duan, Y. Huang, *J. Am. Chem. Soc.* **2015**, 137, 15672.
- [242] G. fa Long, X. hua Li, K. Wan, Z. xing Liang, J. hua Piao, P. Tsiakaras, *Appl. Catal., B* **2017**, 203, 541.
- [243] A. Elangovan, J. Xu, A. Sekar, B. Liu, J. Li, *ChemCatChem* **2020**, 12, 6000.
- [244] L. Chen, Z. Hua, J. Shi, M. He, *ACS Appl. Mater. Interfaces* **2018**, 10, 39002.
- [245] K. Xiang, D. Wu, X. Deng, M. Li, S. Chen, P. Hao, X. Guo, J. L. Luo, X. Z. Fu, *Adv. Funct. Mater.* **2020**, 30, 1909610.
- [246] B. Braunschweig, D. Hibbitts, M. Neurock, A. Wieckowski, *Catal. Today* **2013**, 202, 197.
- [247] J. P. I. De Souza, S. L. Queiroz, K. Bergamaski, E. R. Gonzalez, F. C. Nart, *J. Phys. Chem. B* **2002**, 106, 9825.
- [248] F. Colmati, G. Tremiliosi-Filho, E. R. Gonzalez, A. Berná, E. Herrero, J. M. Feliu, *Phys. Chem. Chem. Phys.* **2009**, 11, 9114.

- [249] A. Kowal, M. Li, M. Shao, K. Sasaki, M. B. Vukmirovic, J. Zhang, N. S. Marinkovic, P. Liu, A. I. Frenkel, R. R. Adzic, *Nat. Mater.* **2009**, *8*, 325.
- [250] K. Liu, W. Wang, P. Guo, J. Ye, Y. Wang, P. Li, Z. Lyu, Y. Geng, M. Liu, S. Xie, *Adv. Funct. Mater.* **2019**, *29*, 1806300.
- [251] N. Erini, R. Loukrakpam, V. Petkov, E. A. Baranova, R. Yang, D. Teschner, Y. Huang, S. R. Brankovic, P. Strasser, *ACS Catal.* **2014**, *4*, 1859.
- [252] L. Bu, S. Guo, X. Zhang, X. Shen, D. Su, G. Lu, X. Zhu, J. Yao, J. Guo, X. Huang, *Nat. Commun.* **2016**, *7*, 11850.
- [253] M. Li, K. Duanmu, C. Wan, T. Cheng, L. Zhang, S. Dai, W. Chen, Z. Zhao, P. Li, H. Fei, Y. Zhu, R. Yu, J. Luo, K. Zang, Z. Lin, M. Ding, J. Huang, H. Sun, J. Guo, X. Pan, W. A. Goddard, P. Sautet, Y. Huang, X. Duan, *Nat. Catal.* **2019**, *2*, 495.
- [254] L. Wang, M. Bevilacqua, Y. X. Chen, J. Filippi, M. Innocenti, A. Lavacchi, A. Marchionni, H. Miller, F. Vizza, *J. Power Sources* **2013**, *242*, 872.
- [255] L. Wang, A. Lavacchi, M. Bellini, F. D'Acapito, F. Di Benedetto, M. Innocenti, H. A. Miller, G. Montegrossi, C. Zafferoni, F. Vizza, *Electrochim. Acta* **2015**, *177*, 100.
- [256] E. A. Monyoncho, S. N. Steinmann, C. Michel, E. A. Baranova, T. K. Woo, P. Sautet, *ACS Catal.* **2016**, *6*, 4894.
- [257] M. Farsadrooh, J. Torrero, L. Pascual, M. A. Peña, M. Retuerto, S. Rojas, *Appl. Catal., B* **2018**, *237*, 866.
- [258] J. Torrero, M. Montiel, M. A. Peña, P. Ocón, S. Rojas, *Int. J. Hydrogen Energy* **2019**, *44*, 31995.
- [259] J. Torrero, M. A. Peña, M. Retuerto, L. Pascual, S. Rojas, *Electrochim. Acta* **2019**, *319*, 312.
- [260] L. K. Tsui, C. Zafferoni, A. Lavacchi, M. Innocenti, F. Vizza, G. Zangari, *J. Power Sources* **2015**, *293*, 815.
- [261] M. V. Pagliaro, M. Bellini, A. Lavacchi, H. A. Miller, C. Bartoli, F. Vizza, *J. Catal.* **2020**, *382*, 237.
- [262] J. Liu, Z. Luo, J. Li, X. Yu, J. Llorca, D. Nasiou, J. Arbiol, M. Meyns, A. Cabot, *Appl. Catal., B* **2019**, *242*, 258.
- [263] E. Ruiz-López, E. Amores, A. Raquel de la Osa, F. Dorado, A. de Lucas-Consuegra, *Chem. Eng. J.* **2020**, *379*, 122289.
- [264] J. de Paula, D. Nascimento, J. J. Linares, *J. Appl. Electrochem.* **2015**, *45*, 689.
- [265] A. B. Calcerrada, A. R. de la Osa, J. Llanos, F. Dorado, A. de Lucas-Consuegra, *Appl. Catal., B* **2018**, *231*, 310.
- [266] C. Lamy, B. Guenot, M. Cretin, G. Pourcelly, *ECS Trans.* **2015**, *66*, 1.
- [267] X.-L. Xing, Y.-F. Zhao, H. Li, C.-T. Wang, Q.-X. Li, W.-B. Cai, *J. Electrochem. Soc.* **2018**, *165*, J3259.
- [268] C. Wang, C. Wu, L. Xing, W. Duan, X. Zhang, Y. Cao, H. Xia, *ACS Appl. Mater. Interfaces* **2020**, *12*, 39033.
- [269] G. H. El-Nowihy, A. M. Mohammad, M. A. Sadek, M. M. H. Khalil, M. S. El-Deab, *J. Electrochem. Soc.* **2019**, *166*, F364.
- [270] J. Mahmoudian, M. Bellini, M. V. Pagliaro, W. Oberhauser, M. Innocenti, F. Vizza, H. A. Miller, *ACS Sustainable Chem. Eng.* **2017**, *5*, 6090.
- [271] O. Movil-Cabrera, A. Rodriguez-Silva, C. Arroyo-Torres, J. A. Staser, *Biomass Bioenergy* **2016**, *88*, 89.
- [272] H. Oh, Y. Choi, C. Shin, T. V. T. Nguyen, Y. Han, H. Kim, Y. H. Kim, J. W. Lee, J. W. Jang, J. Ryu, *ACS Catal.* **2020**, *10*, 2060.
- [273] F. Bateni, M. Naderi-Nasrabadi, R. Ghahremani, J. A. Staser, *J. Electrochem. Soc.* **2019**, *166*, F1037.
- [274] A. Caravaca, W. E. Garcia-Lorefice, S. Gil, A. de Lucas-Consuegra, P. Vernoux, *Electrochem. Commun.* **2019**, *100*, 43.
- [275] X. Du, H. Zhang, K. P. Sullivan, P. Gogoi, Y. Deng, *ChemSusChem* **2020**, *13*, 4318.
- [276] H. Xiao, M. Wu, G. Zhao, *Catalysts* **2015**, *6*, 5.
- [277] Y. Li, M. Nagao, K. Kobayashi, Y. Jin, T. Hibino, *Catalysts* **2020**, *10*, 106.
- [278] W. Liu, Y. Cui, X. Du, Z. Zhang, Z. Chao, Y. Deng, *Energy Environ. Sci.* **2016**, *9*, 467.
- [279] Y. Zhang, H. He, Y. Liu, Y. Wang, F. Huo, M. Fan, H. Adidharma, X. Li, S. Zhang, *Green Chem.* **2019**, *21*, 9.
- [280] D. Wang, S. Liu, Q. Gan, J. Tian, T. T. Isimjan, X. Yang, *J. Electroanal. Chem.* **2018**, *829*, 81.
- [281] D. Zhu, C. Guo, J. Liu, L. Wang, Y. Du, S. Z. Qiao, *Chem. Commun.* **2017**, *53*, 10906.
- [282] R. L. King, G. G. Botte, *J. Power Sources* **2011**, *196*, 9579.
- [283] B. Liu, F. Gao, *Catalysts* **2018**, *8*, 44.
- [284] L. Zhang, L. Wang, H. Lin, Y. Liu, J. Ye, Y. Wen, A. Chen, L. Wang, F. Ni, Z. Zhou, S. Sun, Y. Li, B. Zhang, H. Peng, *Angew. Chem., Int. Ed.* **2019**, *58*, 16820.
- [285] C. Li, Y. Liu, Z. Zhuo, H. Ju, D. Li, Y. Guo, X. Wu, H. Li, T. Zhai, *Adv. Energy Mater.* **2018**, *8*, 1801775.
- [286] D. A. Daramola, D. Singh, G. G. Botte, *J. Phys. Chem. A* **2010**, *114*, 11513.
- [287] V. Vedharathinam, G. G. Botte, *Electrochim. Acta* **2012**, *81*, 292.
- [288] J. Xie, H. Qu, F. Lei, X. Peng, W. Liu, L. Gao, P. Hao, G. Cui, B. Tang, *J. Mater. Chem. A* **2018**, *6*, 16121.
- [289] Z. Y. Yu, C. C. Lang, M. R. Gao, Y. Chen, Q. Q. Fu, Y. Duan, S. H. Yu, *Energy Environ. Sci.* **2018**, *11*, 1890.
- [290] M. Zeng, J. Wu, Z. Li, H. Wu, J. Wang, H. Wang, L. He, X. Yang, *ACS Sustainable Chem. Eng.* **2019**, *7*, 4777.
- [291] C. Wang, H. Lu, Z. Mao, C. Yan, G. Shen, X. Wang, *Adv. Funct. Mater.* **2020**, *30*, 2000556.
- [292] B. Xu, X. Yang, X. Liu, W. Song, Y. Sun, Q. Liu, H. Yang, C. Li, *J. Power Sources* **2020**, *449*, 227585.
- [293] M. He, C. Feng, T. Liao, S. Hu, H. Wu, Z. Sun, *ACS Appl. Mater. Interfaces* **2020**, *12*, 2225.
- [294] Q. Xu, G. Qian, S. Yin, C. Yu, W. Chen, T. Yu, L. Luo, Y. Xia, P. Tsiakaras, *ACS Sustainable Chem. Eng.* **2020**, *8*, 7174.
- [295] D. Liu, T. Liu, L. Zhang, F. Qu, G. Du, A. M. Asiri, X. Sun, *J. Mater. Chem. A* **2017**, *5*, 3208.
- [296] Y. Ding, Y. Li, Y. Xue, B. Miao, S. Li, Y. Jiang, X. Liu, Y. Chen, *Nanoscale* **2019**, *11*, 1058.
- [297] Y. Xu, X. Chai, T. Ren, S. Yu, H. Yu, Z. Wang, X. Li, L. Wang, H. Wang, *Chem. Commun.* **2020**, *56*, 2151.
- [298] Y. Jiang, S. Gao, J. Liu, G. Xu, Q. Jia, F. Chen, X. Song, *Nanoscale* **2020**, *12*, 11573.
- [299] W. Yang, X. Yang, C. Hou, B. Li, H. Gao, J. Lin, X. Luo, *Appl. Catal., B* **2019**, *259*, 118020.
- [300] X. Xu, P. Du, T. Guo, B. Zhao, H. Wang, M. Huang, *ACS Sustainable Chem. Eng.* **2020**, *8*, 7463.
- [301] S. Wang, X. Yang, Z. Liu, D. Yang, L. Feng, *Nanoscale* **2020**, *12*, 10827.
- [302] F. Shen, W. Jiang, G. Qian, W. Chen, H. Zhang, L. Luo, S. Yin, *J. Power Sources* **2020**, *458*, 228014.
- [303] L. Wang, L. Ren, X. Wang, X. Feng, J. Zhou, B. Wang, *ACS Appl. Mater. Interfaces* **2018**, *10*, 4750.
- [304] L. Xia, Y. Liao, Y. Qing, H. Xu, Z. Gao, W. Li, Y. Wu, *ACS Appl. Energy Mater.* **2020**, *3*, 2996.
- [305] A. Fujishima, K. Honda, *Nature* **1972**, *238*, 37.
- [306] P. J. Boddy, *J. Electrochem. Soc.* **1968**, *115*, 199.
- [307] B. Moss, Q. Wang, K. T. Butler, R. Grau-Crespo, S. Selim, A. Regoutz, T. Hisatomi, R. Godin, D. J. Payne, A. Kafizas, K. Domen, L. Steier, J. R. Durrant, *Nat. Mater.* **2021**, *20*, 511.
- [308] L. Pan, J. H. Kim, M. T. Mayer, M.-K. Son, A. Ummadisingu, J. S. Lee, A. Hagfeldt, J. Luo, M. Grätzel, *Nat. Catal.* **2018**, *1*, 412.
- [309] L. Liao, Q. Zhang, Z. Su, Z. Zhao, Y. Wang, Y. Li, X. Lu, D. Wei, G. Feng, Q. Yu, X. Cai, J. Zhao, Z. Ren, H. Fang, F. Robles-Hernandez, S. Baldelli, J. Bao, *Nat. Nanotechnol.* **2014**, *9*, 69.
- [310] L. Pan, Y. Liu, L. Yao, D. Ren, K. Sivula, M. Grätzel, A. Hagfeldt, *Nat. Commun.* **2020**, *11*, 318.
- [311] Y. Xu, Y. Huang, B. Zhang, *Inorg. Chem. Front.* **2016**, *3*, 591.
- [312] J. Barrio, M. Volokh, M. Shalom, *J. Mater. Chem. A* **2020**, *8*, 11075.
- [313] X. Wang, K. Maeda, A. Thomas, K. Takane, G. Xin, J. M. Carlsson, K. Domen, M. Antonietti, *Nat. Mater.* **2009**, *8*, 76.

- [314] W. J. Ong, L. L. Tan, Y. H. Ng, S. T. Yong, S. P. Chai, *Chem. Rev.* **2016**, *116*, 7159.
- [315] Q. Wang, T. Hisatomi, Q. Jia, H. Tokudome, M. Zhong, C. Wang, Z. Pan, T. Takata, M. Nakabayashi, N. Shibata, Y. Li, I. D. Sharp, A. Kudo, T. Yamada, K. Domen, *Nat. Mater.* **2016**, *15*, 611.
- [316] S. Chen, T. Takata, K. Domen, *Nat. Rev. Mater.* **2017**, *2*, 17050.
- [317] C. C. L. McCrory, S. Jung, I. M. Ferrer, S. M. Chatman, J. C. Peters, T. F. Jaramillo, *J. Am. Chem. Soc.* **2015**, *137*, 4347.
- [318] T. Purnima, A. Ruberu, N. C. Nelson, I. I. Slowing, J. Vela, *J. Phys. Chem. Lett.* **2012**, *3*, 2798.
- [319] T. Uekert, C. M. Pichler, T. Schubert, E. Reisner, *Nat. Sustain.* **2021**, *4*, 383.
- [320] W.-J. Ong, K. P. Y. Shak, *Sol. RRL* **2020**, *4*, 2000132.
- [321] S. Kampouri, K. C. Stylianou, *ACS Catal.* **2019**, *9*, 4247.
- [322] X. Lu, S. Xie, H. Yang, Y. Tong, H. Ji, *Chem. Soc. Rev.* **2014**, *43*, 7581.
- [323] X. Chang, T. Wang, P. Yang, G. Zhang, J. Gong, *Adv. Mater.* **2019**, *31*, 1804710.
- [324] D. Wang, Z.-P. Liu, W.-M. Yang, *ACS Catal.* **2018**, *8*, 7270.
- [325] F. J. López-Tenllado, J. Hidalgo-Carrillo, V. Montes, A. Marinas, F. J. Urbano, J. M. Marinas, L. Ilieva, T. Tabakova, F. Reid, *Catal. Today* **2017**, *280*, 58.
- [326] A. V. Puga, *Coord. Chem. Rev.* **2016**, *315*, 1.
- [327] W. T. Chen, A. Chan, D. Sun-Waterhouse, J. Llorca, H. Idriss, G. I. N. Waterhouse, *J. Catal.* **2018**, *367*, 27.
- [328] T. Kawai, T. Sakata, *J. Chem. Soc., Chem. Commun.* **1980**, 694.
- [329] M. Matsumura, M. Hiramoto, T. Iehara, H. Tsubomura, *J. Phys. Chem.* **1984**, *88*, 248.
- [330] J. Choi, S. Y. Ryu, W. Balcerski, T. K. Lee, M. R. Hoffmann, *J. Mater. Chem.* **2008**, *18*, 2371.
- [331] L. A. Silva, S. Young Ryu, J. Choi, W. Choi, M. R. Hoffmann, *J. Phys. Chem. C* **2008**, *112*, 12069.
- [332] A. Patsoura, D. I. Kondarides, X. E. Verykios, *Catal. Today* **2007**, *124*, 94.
- [333] V. M. Daskalaki, D. I. Kondarides, *Catal. Today* **2009**, *144*, 75.
- [334] M. de Oliveira Melo, L. A. Silva, *J. Photochem. Photobiol., A* **2011**, *226*, 36.
- [335] M. Bowker, C. Morton, J. Kennedy, H. Bahruji, J. Greves, W. Jones, P. R. Davies, C. Brookes, P. P. Wells, N. Dimitratos, *J. Catal.* **2014**, *310*, 10.
- [336] M. R. K. Estahbanati, M. Feilzadeh, M. C. Iliuta, *Appl. Catal., B* **2017**, *209*, 483.
- [337] A. Petala, E. Ioannidou, A. Georgaka, K. Bourikas, D. I. Kondarides, *Appl. Catal., B* **2015**, *178*, 201.
- [338] M. R. Karimi Estahbanati, N. Mahinpey, M. Feilzadeh, F. Attar, M. C. Iliuta, *Int. J. Hydrogen Energy* **2019**, *44*, 32030.
- [339] M. J. Berr, P. Wagner, S. Fischbach, A. Vaneski, J. Schneider, A. S. Susha, A. L. Rogach, F. Jäckel, J. Feldmann, *Appl. Phys. Lett.* **2012**, *100*, 223903.
- [340] Y. Wei, G. Cheng, J. Xiong, J. Zhu, Y. Gan, M. Zhang, Z. Li, S. Dou, *J. Energy Chem.* **2019**, *32*, 45.
- [341] D. K. Pallotti, L. Passoni, P. Maddalena, F. Di Fonzo, S. Lettieri, *J. Phys. Chem. C* **2017**, *121*, 9011.
- [342] D. W. Wakerley, M. F. Kuehnel, K. L. Orchard, K. H. Ly, T. E. Rosser, E. Reisner, *Nat. Energy* **2017**, *2*, 17021.
- [343] M. F. Kuehnel, E. Reisner, *Angew. Chem., Int. Ed.* **2018**, *57*, 3290.
- [344] H. Kasap, D. S. Achilleos, A. Huang, E. Reisner, *J. Am. Chem. Soc.* **2018**, *140*, 11604.
- [345] D. Achilleos, W. Yang, H. Kasap, A. Savateev, Y. Markushyna, J. Durrant, E. Reisner, *Angew. Chem., Int. Ed.* **2020**, *59*, 18184.
- [346] T. Uekert, M. F. Kuehnel, D. W. Wakerley, E. Reisner, *Energy Environ. Sci.* **2018**, *11*, 2853.
- [347] J.-J. Wang, Z.-J. Li, X.-B. Li, X.-B. Fan, Q.-Y. Meng, S. Yu, C.-B. Li, J.-X. Li, C.-H. Tung, L.-Z. Wu, *ChemSusChem* **2014**, *7*, 1468.
- [348] V. Gombac, L. Sordelli, T. Montini, J. J. Delgado, A. Adamski, G. Adami, M. Cargnello, S. Bernal, P. Fornasiero, *J. Phys. Chem. A* **2009**, *114*, 3916.
- [349] X. Jiang, X. Fu, L. Zhang, S. Meng, S. Chen, *J. Mater. Chem. A* **2015**, *3*, 2271.
- [350] W. Jones, D. J. Martin, A. Caravaca, A. M. Beale, M. Bowker, T. Maschmeyer, G. Hartley, A. Masters, *Appl. Catal., B* **2019**, *240*, 373.
- [351] T. P. Lyubina, D. V. Markovskaya, E. A. Kozlova, V. N. Parmon, *Int. J. Hydrogen Energy* **2013**, *38*, 14172.
- [352] K. Shimura, H. Yoshida, *Energy Environ. Sci.* **2011**, *4*, 2467.
- [353] B. You, G. Han, Y. Sun, *Chem. Commun.* **2018**, *54*, 5943.
- [354] T. Sakata, T. Kawai, *Chem. Phys. Lett.* **1981**, *80*, 341.
- [355] G. R. Bamwenda, S. Tsubota, T. Nakamura, M. Haruta, *J. Photochem. Photobiol., A* **1995**, *89*, 177.
- [356] A. Y. Nosaka, T. Fujiwara, H. Yagi, H. Akutsu, Y. Nosaka, *Langmuir* **2003**, *19*, 1935.
- [357] C. Wang, H. Groenzin, M. Jane Shultz, *J. Am. Chem. Soc.* **2004**, *126*, 8094.
- [358] G. L. Chiarello, D. Ferri, E. Selli, *J. Catal.* **2011**, *280*, 168.
- [359] C. A. Mesa, A. Kafizas, L. Francàs, S. R. Pendlebury, E. Pastor, Y. Ma, F. Le Formal, M. T. Mayer, M. Grätzel, J. R. Durrant, *J. Am. Chem. Soc.* **2017**, *139*, 11537.
- [360] M. Cargnello, A. Gasparotto, V. Gombac, T. Montini, D. Barreca, P. Fornasiero, *Eur. J. Inorg. Chem.* **2011**, *2011*, 4309.
- [361] Y. Okamoto, S. Ida, J. Hyodo, H. Hagiwara, T. Ishihara, *J. Am. Chem. Soc.* **2011**, *133*, 18034.
- [362] E. Tálas, Z. Pászti, L. Korecz, A. Domján, P. Németh, G. P. Szijártó, J. Mihály, A. Tompos, *Catal. Today* **2018**, *306*, 71.
- [363] Q. Hao, Zhiqiang Wang, T. Wang, Z. Ren, C. Zhou, X. Yang, *ACS Catal.* **2019**, *9*, 286.
- [364] G. L. Chiarello, M. H. Aguirre, E. Selli, *J. Catal.* **2010**, *273*, 182.
- [365] J.-C. Wang, C.-X. Cui, Q.-Q. Kong, C.-Y. Ren, Z. Li, L. Qu, Y. Zhang, K. Jiang, *ACS Sustainable Chem. Eng.* **2018**, *6*, 8754.
- [366] C. A. Walenta, C. Courtois, S. L. Kollmannsberger, M. Eder, M. Tschurl, U. Heiz, *ACS Catal.* **2020**, *10*, 4080.
- [367] M. Osmić, L. Mohrhusen, K. Al-Shamery, *J. Phys. Chem. C* **2018**, *123*, 7615.
- [368] Q. Guo, C. Xu, Z. Ren, W. Yang, Z. Ma, D. Dai, H. Fan, T. K. Minton, X. Yang, *J. Am. Chem. Soc.* **2012**, *134*, 13366.
- [369] Z. Liu, Z. Yin, C. Cox, M. Bosman, X. Qian, N. Li, H. Zhao, Y. Du, J. Li, D. G. Nocera, *Sci. Adv.* **2016**, *2*, 1501425.
- [370] Y. Liu, S. Yang, S.-N. Yin, L. Feng, Y. Zang, H. Xue, *Chem. Eng. J.* **2018**, *334*, 2401.
- [371] Y. Z. Yang, C.-H. Chang, H. Idriss, *Appl. Catal., B* **2006**, *67*, 217.
- [372] M. Antoniadou, V. Vaiano, D. Sannino, P. Lianos, *Chem. Eng. J.* **2013**, *224*, 144.
- [373] C. Ampelli, R. Passalacqua, C. Genovese, S. Perathoner, G. Centi, T. Montini, V. Gombac, J. J. Delgado Jaen, P. Fornasiero, *RSC Adv.* **2013**, *3*, 21776.
- [374] G. Carraro, C. Maccato, A. Gasparotto, T. Montini, S. Turner, O. I. Lebedev, V. Gombac, G. Adami, G. Van Tendeloo, D. Barreca, P. Fornasiero, *Adv. Funct. Mater.* **2014**, *24*, 372.
- [375] M. Murdoch, G. I. N. Waterhouse, M. A. Nadeem, J. B. Metson, M. A. Keane, R. F. Howe, J. Llorca, H. Idriss, *Nat. Chem.* **2011**, *3*, 489.
- [376] Y. X. Chen, V. Gombac, T. Montini, A. Lavacchi, J. Filippi, H. A. Miller, P. Fornasiero, F. Vizza, *Green Chem.* **2018**, *20*, 2299.
- [377] C. Xing, Y. Liu, Y. Zhang, X. Wang, P. Guardia, L. Yao, X. Han, T. Zhang, J. Arbiol, L. Soler, Y. Chen, K. Sivula, N. Guijarro, A. Cabot, J. Llorca, *ACS Appl. Mater. Interfaces* **2021**, *13*, 449.
- [378] Z. Han, F. Qiu, R. Eisenberg, P. L. Holland, T. D. Krauss, *Science* **2012**, *338*, 1321.
- [379] L.-M. Zhao, Q.-Y. Meng, X.-B. Fan, C. Ye, X.-B. Li, B. Chen, V. Ramamurthy, C.-H. Tung, L.-Z. Wu, *Angew. Chem., Int. Ed.* **2017**, *56*, 3020.
- [380] T. Simon, N. Bouchonville, M. J. Berr, A. Vaneski, A. Adrović, D. Volbers, R. Wyrwich, M. Döblinger, A. S. Susha, A. L. Rogach, F. Jäckel, J. K. Stolarczyk, J. Feldmann, *Nat. Mater.* **2014**, *13*, 1013.

- [381] Z. Chai, T.-T. Zeng, Q. Li, L.-Q. Lu, W.-J. Xiao, D. Xu, *J. Am. Chem. Soc.* **2016**, *138*, 10128.
- [382] C. Minero, A. Bedini, V. Maurino, *Appl. Catal., B* **2012**, *128*, 135.
- [383] M. R. Karimi Estahbanati, M. Feilizadeh, F. Attar, M. C. Iliuta, *React. Chem. Eng.* **2021**, *6*, 197.
- [384] G. Dodekatos, H. Tüysüz, *Catal. Sci. Technol.* **2016**, *6*, 7307.
- [385] Y. Zhang, N. Zhang, Z.-R. Tang, Y.-J. Xu, *Chem. Sci.* **2013**, *4*, 1820.
- [386] S. Taylor, M. Mehta, A. Samokhvalov, *ChemPhysChem* **2014**, *15*, 942.
- [387] G. Sadanandam, D. K. Valluri, M. S. Scurrrell, *Int. J. Hydrogen Energy* **2017**, *42*, 807.
- [388] G. Dodekatos, S. Schünemann, H. Tüysüz, *ACS Catal.* **2018**, *8*, 6301.
- [389] V. Maurino, A. Bedini, M. Minella, F. Rubertelli, E. Pelizzetti, C. Minero, *J. Adv. Oxid. Technol.* **2008**, *11*, 184.
- [390] M. Li, Y. Li, S. Peng, G. Lu, S. Li, *Front. Chem. China* **2009**, *4*, 32.
- [391] V. Gombac, L. Sordelli, T. Montini, J. J. Delgado, A. Adamski, G. Adami, M. Cargnello, S. Bernal, P. Fornasiero, *J. Phys. Chem. A* **2010**, *114*, 3916.
- [392] K. Lalitha, G. Sadanandam, V. Durga Kumari, M. Subrahmanyam, B. Sreedhar, N. Y. Hebalkar, *J. Phys. Chem. C* **2010**, *114*, 22181.
- [393] T. Montini, V. Gombac, L. Sordelli, J. J. Delgado, X. Chen, G. Adami, P. Fornasiero, *ChemCatChem* **2011**, *3*, 574.
- [394] M. Zhang, R. Sun, Y. Li, Q. Shi, L. Xie, J. Chen, X. Xu, H. Shi, W. Zhao, *J. Phys. Chem. C* **2016**, *120*, 10746.
- [395] L. Clarizia, I. Di Somma, L. Onotri, R. Andreozzi, R. Marotta, *Catal. Today* **2017**, *281*, 117.
- [396] P. Panagiotopoulou, E. E. Karamerou, D. I. Kondarides, *Catal. Today* **2013**, *209*, 91.
- [397] A. Molinari, A. Maldotti, A. Bratovic, G. Magnacca, *Catal. Today* **2013**, *206*, 46.
- [398] V. Augugliaro, H. A. H. El Nazer, V. Loddo, A. Mele, G. Palmisano, L. Palmisano, S. Yurdakal, *Catal. Today* **2010**, *151*, 21.
- [399] Y. Chen, J. Zhang, M. Zhang, X. Wang, *Chem. Sci.* **2013**, *4*, 3244.
- [400] R. Liu, H. Yoshida, S. Fujita, M. Arai, *Appl. Catal., B* **2014**, *144*, 41.
- [401] S. Fujita, H. Kawamori, D. Honda, H. Yoshida, M. Arai, *Appl. Catal., B* **2016**, *181*, 818.
- [402] A. Beltram, I. Romero-Ocaña, J. José Delgado Jaen, T. Montini, P. Fornasiero, *Appl. Catal., A* **2016**, *518*, 167.
- [403] C. Li, Y. Na, *ChemPhotoChem* **2020**, *n/a*.
- [404] T. Butburee, P. Chakthranont, C. Phawa, K. Faungnawakij, *ChemCatChem* **2020**, *12*, 1873.
- [405] X. Wu, N. Luo, S. Xie, H. Zhang, Q. Zhang, F. Wang, Y. Wang, *Chem. Soc. Rev.* **2020**, *49*, 6198.
- [406] I. Krivtsov, E. I. García-López, G. Marci, L. Palmisano, Z. Amghouz, J. R. García, S. Ordóñez, E. Díaz, *Appl. Catal., B* **2017**, *204*, 430.
- [407] V. R. Battula, A. Jaryal, K. Kailasam, *J. Mater. Chem. A* **2019**, *7*, 5643.
- [408] G. Han, Y.-H. Jin, R. Alan Burgess, N. E. Dickenson, X.-M. Cao, Y. Sun, *J. Am. Chem. Soc.* **2017**, *139*, 15584.
- [409] H.-F. Ye, R. Shi, X. Yang, W.-F. Fu, Y. Chen, *Appl. Catal., B* **2018**, *233*, 70.
- [410] S. Dhingra, T. Chhabra, V. Krishnan, C. M. Nagaraja, *ACS Appl. Energy Mater.* **2020**, *3*, 7138.
- [411] J. Fu, J. Yu, C. Jiang, B. Cheng, *Adv. Energy Mater.* **2018**, *8*, 1701503.
- [412] W.-J. Ong, *Front. Mater.* **2017**, *4*, 1.
- [413] Y. Wang, X. Kong, M. Jiang, F. Zhang, X. Lei, *Inorg. Chem. Front.* **2020**, *7*, 437.
- [414] S. Meng, H. Wu, Y. Cui, X. Zheng, H. Wang, S. Chen, Y. Wang, X. Fu, *Appl. Catal., B* **2020**, *266*, 118617.
- [415] Q.-Y. Meng, J.-J. Zhong, Q. Liu, X.-W. Gao, H.-H. Zhang, T. Lei, Z.-J. Li, K. Feng, B. Chen, C.-H. Tung, L.-Z. Wu, *J. Am. Chem. Soc.* **2013**, *135*, 19052.
- [416] B. Xia, Y. Zhang, B. Shi, J. Ran, K. Davey, S.-Z. Qiao, *Small Methods* **2020**, *4*, 2000063.
- [417] N. Luo, T. Hou, S. Liu, B. Zeng, J. Lu, J. Zhang, H. Li, F. Wang, *ACS Catal.* **2020**, *10*, 762.
- [418] S. Xie, Z. Shen, J. Deng, P. Guo, Q. Zhang, H. Zhang, C. Ma, Z. Jiang, J. Cheng, D. Deng, Y. Wang, *Nat. Commun.* **2018**, *9*, 1181.
- [419] L. Meng, Z. Chen, Z. Ma, S. He, Y. Hou, H.-H. Li, R. Yuan, X.-H. Huang, X. Wang, X. Wang, J. Long, *Energy Environ. Sci.* **2018**, *11*, 294.
- [420] S. Remiro-Buenamañana, H. García, *ChemCatChem* **2019**, *11*, 342.
- [421] J. Barrio, D. Mateo, J. Albero, H. García, M. Shalom, *Adv. Energy Mater.* **2019**, *9*, 1902738.
- [422] L. Li, G.-D. Li, C. Yan, X.-Y. Mu, X.-L. Pan, X.-X. Zou, K.-X. Wang, J.-S. Chen, *Angew. Chem., Int. Ed.* **2011**, *50*, 8299.
- [423] C. Jiang, S. J. A. Moniz, A. Wang, T. Zhang, J. Tang, *Chem. Soc. Rev.* **2017**, *46*, 4645.
- [424] M. Grätzel, *Materials For Sustainable Energy: A Collection of Peer-Reviewed Research and Review Articles from Nature Publishing Group*, World Scientific, Singapore **2011**, pp. 26–32.
- [425] W. Justin Youngblood, S.-H. Anna Lee, Y. Kobayashi, E. A. Hernandez-Pagan, P. G. Hoertz, T. A. Moore, A. L. Moore, D. Gust, T. E. Mallouk, *J. Am. Chem. Soc.* **2009**, *131*, 926.
- [426] A. P. Singh, S. Kumari, R. Shrivastav, S. Dass, V. R. Satsangi, *Int. J. Hydrogen Energy* **2008**, *33*, 5363.
- [427] X. Chen, L. Liu, P. Y. Yu, S. S. Mao, *Science* **2011**, *331*, 746.
- [428] A. G. Tamirat, J. Rick, A. A. Dubale, W.-N. Su, B.-J. Hwang, *Nanoscale Horiz.* **2016**, *1*, 243.
- [429] F. F. Abdi, L. Han, A. H. M. Smets, M. Zeman, B. Dam, R. van de Krol, *Nat. Commun.* **2013**, *4*, 2195.
- [430] M. Volokh, G. Peng, J. Barrio, M. Shalom, *Angew. Chem., Int. Ed.* **2019**, *58*, 6138.
- [431] I. Poli, U. Hintermair, M. Regue, S. Kumar, E. V. Sackville, J. Baker, T. M. Watson, S. Eslava, P. J. Cameron, *Nat. Commun.* **2019**, *10*, 2097.
- [432] D. I. Kondarides, V. M. Daskalaki, A. Patsoura, X. E. Verykios, *Catal. Lett.* **2008**, *122*, 26.
- [433] J. P. Barham, B. König, *Angew. Chem., Int. Ed.* **2020**, *59*, 11732.
- [434] A. Y. Ru Ng, B. Boruah, K. F. Chin, J. M. Modak, H. Sen Soo, *ChemNanoMat* **2020**, *6*, 185.
- [435] T. Hardwick, A. Qurashi, B. Shirinfar, N. Ahmed, *ChemSusChem* **2020**, *13*, 1967.
- [436] N. Ibrahim, S. K. Kamarudin, L. J. Minggu, *J. Power Sources* **2014**, *259*, 33.
- [437] G. Wang, Y. Ling, X. Lu, H. Wang, F. Qian, Y. Tong, Y. Li, *Energy Environ. Sci.* **2012**, *5*, 8215.
- [438] M. Antoniadou, P. Bouras, N. Strataki, P. Lianos, *Int. J. Hydrogen Energy* **2008**, *33*, 5045.
- [439] M. Antoniadou, P. Lianos, *J. Photochem. Photobiol., A* **2009**, *204*, 69.
- [440] M. Antoniadou, P. Lianos, *Appl. Catal., B* **2010**, *99*, 307.
- [441] N. Strataki, M. Antoniadou, V. Dracopoulos, P. Lianos, *Catal. Today* **2010**, *151*, 53.
- [442] R. Bashiri, N. M. Mohamed, C. Fai Kait, S. Sufian, M. Khatani, *Int. J. Hydrogen Energy* **2017**, *42*, 9553.
- [443] P. Zhang, A. Kleiman-Shwarscstein, Y.-S. Hu, J. Lefton, S. Sharma, A. J. Forman, E. McFarland, *Energy Environ. Sci.* **2011**, *4*, 1020.
- [444] R. Mazza, S. Boscolo Bibi, M. Natali, G. Bergamini, V. Morandi, P. Ceroni, A. Vomiero, *Nano Energy* **2019**, *61*, 36.
- [445] T. Li, T. Kasahara, J. He, K. E. Dettelbach, G. M. Sammis, C. P. Berlinguette, *Nat. Commun.* **2017**, *8*, 390.
- [446] H. G. Cha, K.-S. Choi, *Nat. Chem.* **2015**, *7*, 328.
- [447] D. J. Chadderdon, L.-P. Wu, Z. A. McGraw, M. Panthani, W. Li, *ChemElectroChem* **2019**, *6*, 3387.
- [448] L. W. Huang, T. G. Vo, C. Y. Chiang, *Electrochim. Acta* **2019**, *322*, 134725.
- [449] T. G. Vo, C. C. Kao, J. L. Kuo, C. Chau Chiu, C. Y. Chiang, *Appl. Catal., B* **2020**, *278*, 119303.

- [450] D. Liu, J. C. Liu, W. Cai, J. Ma, H. Bin Yang, H. Xiao, J. Li, Y. Xiong, Y. Huang, B. Liu, *Nat. Commun.* **2019**, *10*, 1779.
- [451] S. R. Pradhan, V. Nair, D. A. Giannakoudakis, D. Lisovtyskiy, J. C. Colmenares, *Mol. Catal.* **2020**, *486*, 110884.
- [452] G. Ramis, E. Bahadori, I. Rossetti, *Int. J. Hydrogen Energy* **2021**, *46*, 12105.
- [453] J. Barrio, N. Karjule, J. Qin, M. Shalom, *ChemCatChem* **2019**, *11*, 6295.
- [454] R. Gulaboski, I. Bogeski, V. Mirčeski, S. Saul, B. Pasička, H. H. Haeri, M. Stefova, J. P. Stanoeva, S. Mitrev, M. Hoth, R. Kappl, *Sci. Rep.* **2013**, *3*, 1865.
- [455] E. Illés, E. Takács, A. Dombi, K. Gajda-Schrantz, G. Rác, K. Gonter, L. Wojnárovits, *Sci. Total Environ.* **2013**, *447*, 286.
- [456] J. T. Schneider, D. S. Firak, R. R. Ribeiro, P. Peralta-Zamora, *Phys. Chem. Chem. Phys.* **2020**, *22*, 15723.
- [457] K. Gelderman, L. Lee, S. W. Donne, *J. Chem. Educ.* **2007**, *84*, 685.
- [458] W.-J. Chun, A. Ishikawa, H. Fujisawa, T. Takata, J. N. Kondo, M. Hara, M. Kawai, Y. Matsumoto, K. Domen, *J. Phys. Chem. B* **2003**, *107*, 1798.
- [459] G. H. Rau, H. D. Willauer, Z. J. Ren, *Nat. Clim. Change* **2018**, *8*, 621.
- [460] O. Babacan, S. De Causmaecker, A. Gambhir, M. Fajardy, A. W. Rutherford, A. Fantuzzi, J. Nelson, *Nat. Energy* **2020**, *5*, 720.
- [461] ICC, *Role of Carbon and Long-Term Mitigation Strategies Beyond 2050 through Carbon Capture and Use (CCU) and Closing the Carbon Cycles (C³) Policy Statement Prepared by the ICC Commission on Environment and Energy*, ICC, Paris **2016**.
- [462] H. Valin, D. Peters, M. van den Berg, S. Frank, P. Havlik, N. Forsell, C. Hamelinck, J. Pirker, A. Mosnier, J. Balkovic, E. Schmid, M. Dürauer, F. di Fulvio, *The land use change impact of biofuels consumed in the EU: Quantification of area and greenhouse gas impacts*. ECOFYS Netherlands B.V, Utrecht, Netherlands **2015**.
- [463] A. Brandt, J. Gräsvik, J. P. Hallett, T. Welton, *Green Chem.* **2013**, *15*, 550.
- [464] Y. M. Questell-Santiago, M. V. Galkin, K. Barta, J. S. Luterbacher, *Nat. Rev. Chem.* **2020**, *4*, 311.
- [465] P. P. Thoresen, L. Matsakas, U. Rova, P. Christakopoulos, *Biore-sour. Technol.* **2020**, *306*, 123189.
- [466] Y. T. Tan, A. S. M. Chua, G. C. Ngoh, *Biore-sour. Technol.* **2020**, *297*, 122522.
- [467] R. Davis, L. Tao, E. C. D. Tan, M. J. Bidy, G. T. Beckham, C. Scarlata, *Process Design and Economics for the Conversion of Lignocellulosic Biomass to Hydrocarbons: Dilute-Acid and Enzymatic Deconstruction of Biomass to Sugars and Biological Conversion of Sugars to Hydrocarbons Process Design and Economics for the Conversion*.
- [468] E. M. Anderson, L. Michael, R. Katahira, G. T. Beckham, E. M. Anderson, M. L. Stone, R. Katahira, M. Reed, G. T. Beckham, Y. Roma, *Joule* **2017**, *1*, 613.
- [469] B. Jiang, L. Li, Q. Zhang, J. Ma, H. Zhang, J. Bai, Z. Bian, B. Dou, S. Kawi, D. Tang, *Energy Fuels* **2020**, *34*, 1841.
- [470] R. Latsuzbaia, R. Bisselink, A. Anastasopol, H. van der Meer, R. van Heck, M. S. Yagüe, M. Zijlstra, M. Roelands, M. Crockett, E. Goetheer, E. Giling, *J. Appl. Electrochem.* **2018**, *48*, 611.
- [471] J. A. Turner, *Science* **2004**, *305*, 972.
- [472] R. J. Crawford, K. J. Edler, S. Lindhoud, J. L. Scott, G. Unali, *Green Chem.* **2012**, *14*, 300.
- [473] A. H. Motagamwala, W. Won, C. Sener, D. M. Alonso, C. T. Maravelias, J. A. Dumesic, *Sci. Adv.* **2018**, *4*, 9722.
- [474] W. Boonkong, P. Sangvanich, A. Petsom, N. Thongchul, *Chem. Eng. Technol.* **2009**, *32*, 1542.
- [475] A. Saxena, G. S. Gohil, V. K. Shahi, *Ind. Eng. Chem. Res.* **2007**, *46*, 1270.
- [476] S. Yang, A. Verdaguer-Casadevall, L. Arnarson, L. Silvioli, V. Čolić, R. Frydendal, J. Rossmeis, I. Chorkendorff, I. E. L. Stephens, *ACS Catal.* **2018**, *8*, 4064.
- [477] H. A. Miller, K. Bouzek, J. Hnat, S. Loos, C. I. Bernäcker, T. Weißgärber, L. Röntzsch, J. Meier-Haack, *Sustainable Energy Fuels* **2020**, *4*, 2114.
- [478] IRENA, *Hydrogen From Renewable Power: Technology Outlook for the Energy Transition*, IRENA, Abu Dhabi **2018**.
- [479] S. Westhues, J. Idel, J. Klankermayer, *Sci. Adv.* **2018**, *4*, 9669.
- [480] H. Roy Ghatak, *Int. J. Hydrogen Energy* **2006**, *31*, 934.
- [481] H. R. Ghatak, S. Kumar, P. P. Kundu, *Int. J. Hydrogen Energy* **2008**, *33*, 2904.
- [482] T. Hibino, K. Kobayashi, M. Ito, Q. Ma, M. Nagao, M. Fukui, S. Teranishi, *ACS Sustainable Chem. Eng.* **2018**, *6*, 9360.
- [483] T. Hibino, K. Kobayashi, M. Ito, M. Nagao, M. Fukui, S. Teranishi, *Appl. Catal., B* **2018**, *231*, 191.
- [484] S. Verma, S. Lu, P. J. A. Kenis, *Nat. Energy* **2019**, *4*, 466.
- [485] M. Bajada, S. Roy, J. Warnan, K. Abdiaziz, A. Wagner, M. Roessler, E. Reisner, *Angew. Chem.* **2020**, *132*, 15763.
- [486] R. S. Sherbo, R. S. Delima, V. A. Chiykowski, B. P. MacLeod, C. P. Berlinguette, *Nat. Catal.* **2018**, *1*, 501.
- [487] T. Wu, B. H. Nguyen, M. C. Daugherty, K. D. Moeller, *Angew. Chem., Int. Ed.* **2019**, *58*, 3562.



Hui Luo received her Ph.D. in Materials Science from Queen Mary University of London in 2019, working on photo(electro)catalytic water splitting. She is currently a research associate at the Department of Chemical Engineering in Imperial College London, working with Prof. Maria-Magdalena Titirici. Her research focuses on biomass electrolysis, which investigates the possibility to transform abundant biomass platform molecules into H₂ and high-value bio-based compounds with low energy consumption and minimal carbon footprints.



Nilay Shah is the Head of the Department of Chemical Engineering at Imperial College. His research interests include the application of multiscale process modeling and mathematical/systems engineering techniques to analyze and optimize complex, spatially- and temporally-explicit low-carbon industrial and energy systems, including chemical process systems, urban energy systems, carbon capture and storage, hydrogen infrastructures, and bioenergy systems. He is particularly interested in the transfer of technology from academia to industry.



Ifan E. L. Stephens received his Ph.D. from Cambridge, before moving to the Technical University of Denmark (DTU), first as a postdoctoral researcher and finally as associate professor and leader of the Electrocatalysis Group there. In 2015, Massachusetts Institute of Technology (MIT) awarded Ifan the Peabody Visiting Associate Professorship. Since 2017, he has been at the Department of Materials at Imperial College London, where he currently holds the position of reader in electrochemistry. His research aims to enable the large-scale electrochemical conversion of renewable energy to fuels and valuable chemicals and vice versa, with a focus on the electrocatalyst.



Magda Titirici has a Ph.D. from University of Dortmund and a German “Habilitation” from Max-Planck Institute of Colloids and Interfaces/University of Potsdam. She is currently a Professor of Sustainable Energy Materials in the department of Chemical Engineering at Imperial College London. Magda's research interests are in the area of energy storage and conversion materials, in particular in the development of batteries beyond Li-ion, oxygen electrocatalysis free of critical metals, and alternative production of H₂ with co-producing chemicals via biomass electro-oxidation.